Summer 2012

A generalized model for hydrocarbon drops spreading on a horizontal smooth solid surface

Yan Zhang
University of Iowa

A GENERALIZED MODEL FOR HYDROCARBON DROPS SPREADING ON A HORIZONTAL SMOOTH SOLID SURFACE

by

Yan Zhang

An Abstract

Of a thesis submitted in partial fulfillment
of the requirements for the Doctor of
Philosophy degree in Mechanical Engineering in
the Graduate College of
The University of Iowa

July 2012

Thesis Supervisor: Associate Professor Albert Ratner

ABSTRACT

Hydrocarbon drops impacting on a flat solid surface were experimentally and computationally studied to identify the key issues in the dynamics of drop spreading. Three hydrocarbon liquids were tested: diesel, methanol and glycerin. The evolutions of dynamic contact angle and spreading diameter were measured at each time step after impact from the recorded images. Two distinguishable regimes were observed during the evolutions: an initial kinetic regime followed by a spreading regime. While the kinetic regime could be accurately predicted with a single static contact angle (SCA) model, in this work, a general empirical expression (in terms of the Ohnesorge number) was constructed that accurately describe the spreading regime. The transition threshold, from the kinetic regime to the spreading regime, follows with a power law, changing as a function of Reynolds number.

In addition to the experimental investigations, the drop spreading process was studied numerically with a volume-of-fluid (VOF) approach. Based on these investigations, a new combined static contact angle-dynamic contact angle (SCA-DCA) model was proposed and applied to compute the hydrocarbon drop spreading process. The predicted time-dependent drop shapes agree well, within 5% of both previously published results and the experimental data presented here, while previous models showed at least a 10% deviation from the experiments. This proposed model also avoids the requirement for experimental measurement with specific fluids and only requires the general fluid properties. An added benefit of this methodology is that the computational cost is greatly reduced compared with the existing (full DCA-based) models.

To broaden the applicable range of this new model, water drop spreading on the solid surface was also studied. It was concluded that this model could predict the liquid drop spreading on a flat smooth solid surface (clean glass) with the range of $Oh = O(0.001) - O(0.1)$, $We = O(1) - O(100)$, $\mathrm{Re} = O(10) - O(1000)$.

Abstract Approved: _____

Thesis Supervisor

_____

Title and Department

_____

Date

A GENERALIZED MODEL FOR HYDROCARBON DROPS SPREADING ON A HORIZONTAL SMOOTH SOLID SURFACE

by

Yan Zhang

A thesis submitted in partial fulfillment
of the requirements for the Doctor of
Philosophy degree in Mechanical Engineering
in the Graduate College of
The University of Iowa

July 2012

Thesis Supervisor: Associate Professor Albert Ratner

Graduate College
The University of Iowa
Iowa City, Iowa

CERTIFICATE OF APPROVAL

_____

PH.D. THESIS

_____

This is to certify that the Ph.D. thesis of

Yan Zhang

has been approved by the Examining Committee
for the thesis requirement for the Doctor of Philosophy
degree in Mechanical Engineering at the July 2012 graduation.

Thesis Committee: _____
Albert Ratner, Thesis Supervisor

_____
James H.J. Buchholz

_____
Pablo M. Carrica

_____
Jennifer Fiegel

_____
Ching-Long Lin

To My Loved Parents

ACKNOWLEDGMENTS

I would like to express my deep and sincere gratitude to my supervisor, Associate Professor Albert Ratner. His wide knowledge and his logical way of thinking have been of great value for me. His personal guidance, support, understanding, patience, and encouraging have helped me learn and grow for the past years. He is such an excellent advisor for whom I would be grateful for all my life.

I would also warmly thank my committee members Professor Ching-Long Lin, Pablo Carrica, James Buchholz, and Jennifer Fiegel for their important support and constructive comments on this work.

This research project also would not have been possible without the support of Neeraj Kumar. His experimental data have built up a solid foundation for my research.

I would also like to convey thanks to my lab mates – Yunye, Xinhui, Majid, Mohsen, Matt, Taleb, Doug, Scott and Jianan, for giving me a memorable experience in Iowa. Special thanks to my best friend Yunye for her warm accompany through the duration of my studies. Finally, I wish to express my love and gratitude to my beloved parents, for their understanding and endless love all the way.

ABSTRACT

Hydrocarbon drops impacting on a flat solid surface were experimentally and computationally studied to identify the key issues in the dynamics of drop spreading. Three hydrocarbon liquids were tested: diesel, methanol and glycerin. The evolutions of dynamic contact angle and spreading diameter were measured at each time step after impact from the recorded images. Two distinguishable regimes were observed during the evolutions: an initial kinetic regime followed by a spreading regime. While the kinetic regime could be accurately predicted with a single static contact angle (SCA) model, in this work, a general empirical expression (in terms of the Ohnesorge number) was constructed that accurately describe the spreading regime. The transition threshold, from the kinetic regime to the spreading regime, follows with a power law, changing as a function of Reynolds number.

In addition to the experimental investigations, the drop spreading process was studied numerically with a volume-of-fluid (VOF) approach. Based on these investigations, a new combined static contact angle-dynamic contact angle (SCA-DCA) model was proposed and applied to compute the hydrocarbon drop spreading process. The predicted time-dependent drop shapes agree well, within 5% of both previously published results and the experimental data presented here, while previous models showed at least a 10% deviation from the experiments. This proposed model also avoids the requirement for experimental measurement with specific fluids and only requires the general fluid properties. An added benefit of this methodology is that the computational cost is greatly reduced compared with the existing (full DCA-based) models.

To broaden the applicable range of this new model, water drop spreading on the solid surface was also studied. It was concluded that this model could predict the liquid drop spreading on a flat smooth solid surface (clean glass) with the range of $Oh = O(0.001) - O(0.1)$, $We = O(1) - O(100)$, $\mathrm{Re} = O(10) - O(1000)$.

TABLE OF CONTENTS

LIST OF TABLES

LIST OF FIGURES

NOMENCLATURE

Notation

CFD = Computational fluid dynamics

d = Drop spread diameter at a given time, m

D = Initial drop diameter, m

DCA = Dynamic contact angle, °

t = Time measured from the instant of impact, s

t^* = Dimensionless transition instance from kinetic regime to spreading regime

u = Impact speed of the drop, m/s

ν = Kinematic viscosity, m^2 / s

V = Spreading velocity, m/s

VOF = Volume of fluid

SCA = Static contact angle, °

Greek letters

α = impingement angle, °

α_k = volume fraction of the k^{th} fluid

β = Spread factor = d / D

μ = Viscosity of the liquid, $Pa \cdot s$

θ_d^* = Apparent dynamic contact angle, °

θ_a = Advancing contact angle, °

θ_d = Macroscopic dynamic contact angle, °

θ_r = Receding contact angle, °

θ_e = Static contact angle, °

σ = Surface tension, N/m

Dimensionless groups

Ca = Capillary number = $V\mu / \sigma$

Oh = Ohnesorge number = $\mu / \sqrt{\rho\sigma D}$

We = Weber number = $(\rho D u^2) / \sigma$

Re = Reynolds number = $\rho D u / \mu$

CHAPTER 1: INTRODUCTION

1.1 Motivation

Drop impacts on surfaces are important in a wide range of industrial applications. These applications include ink-jet printing, spray cooling of hot surfaces (e.g. turbine blades), spray coating and painting, internal combustion engines (the interaction of drops with hot walls of combustion engine), annealing, fire extinguishing, liquid atomization and cleaning, production of electric circuits (the precision of solder-drop dispensing), and nucleate boiling (enhanced by the entrainment of bubbles by drop falling into a superheated liquid) (Rein, 1993; Yarin, 2006). Beyond these industrial applications, drop-surface interactions also occur in agriculture (e.g. crop spraying), meteorology (e.g. the interaction of the rain with the earth), geology (e.g. the erosion of soil), and criminal forensics (the collection of stain patterns of blood drops) (Rein, 1993; Yarin, 2006).

Fire safety is of particular interest in this work. Vehicle crash-induced fires account for over half of the deaths (58%) in transportation accidents (Bunn et al., 2012). While significant progress has been made in reducing the number of accidents, crash safety equipment (like seat belts and air bags) has been a critical component in the reduction of fatalities and serious injuries. One promising direction for reducing fatalities is to eliminate or significantly reduce crash-induced fires. The simplest and most direct way to do this is to modify the fuel so that it does not ignite in an accident. One of the ways in which this can be done is through the addition of long chained polymers to the fuel to prevent the break-up of the fuel into a fine mist, as this is typically what gets ignited in crash-induced fires (Ratner, 2009). The mist-preventing process works by the long-strand polymers inducing a non-Newtonian shear-thickening behavior in the fuel (Ameri David et al., 2009). To evaluate both the shear-thickening effect and regular fuel behavior, a simple experimental and computational scenario needs to be employed. The scenario utilized in this work measures the impact of hydrocarbon drops on a solid

surface, which is a basic component of various natural and industrial processes, has been widely utilized in fluid mechanics research, and is a simple and clean model on which to investigate the variable viscosity and shear stress of liquids. The dynamics of hydrocarbon drops (Newtonian liquids) spreading on a flat smooth surface is studied in this work as a starting point for the non-Newtonian behavior to be investigated in the future.

The behavior of drops impacting on a solid surface can be characterized into three different modes: bouncing, spreading or splashing (details are introduced in Chapter 2.1.2). The mode observed is due to the interactions of initial drop speed, pressure, surface roughness, drop viscosity and surface tension. The behaviors of water, glycerin, and silicon oil drops impacting on a solid surface have been widely examined through both experimental and numerical studies. These studies produced a consensus that the process of drop spreading on a solid surface experiences four stages (Rioboo et al., 2002): a kinematic regime, a spreading regime, a relaxation regime and a wetting/equilibrium regime (as shown in Figure 1-1). After initial contact with the solid surface, the early dynamics of the drop are primarily dictated by the initial kinetic energy. The kinetic energy during the first regime (while the drop shape is that of a truncated sphere) transforms from vertical to horizontal motion, and the drop spreads out like a liquid disk, called a lamella. As the lamella spreads out along the solid surface, the kinetic energy of the drop is both dissipated by viscous processes and transferred into additional surface tension energy. When the drop achieves its maximum diameter, several different phenomena may occur.

Some drops may bounce off after the impact (if the initial kinetic energy is large enough to be fully dissipated during the second regime). Some may develop oscillations which are influenced by surface roughness (Engel, 1955) and the wettability of the system (solid-liquid-gas) (Woerhington, 1877). The undulations induced along the rim may develop further, resulting in the formation of a corona and corona splashing at

certain conditions (L. Xu et al., 2005). Figure 1-1 (Rioboo, et al., 2002) shows the four different stages of a drop impacting on a solid surface in terms of the spread factor, which is defined as the is the ratio of the spreading diameter to the initial diameter: $\beta = d / D$. For the conditions of interest here (for fuel drops at a moderate speed), the drops reach their maximum diameters on the smooth surface and the lamellas stop and the drop is stabilized (as the dot line shown in Figure 1-1).

There are several important parameters that are examined in this study. The viscosity and the surface tension of the drop are μ and σ separately. A single drop with the initial diameter D is released freely and impacts on the solid surface with the impact (vertical) speed u. The drop then spreads along the solid surface with the spreading (horizontal) speed V. As shown in Figure 1-1, the spread factor β is a critical parameter and is typically used to describe the evolution of the drop spreading. Beyond the spread factor, the contact angle is another important parameter considered in drop impact studies. As the drop is spreading, the contact line is moving outwards, towards the gas phase with the varying dynamic contact angle (DCA) θ_d. Note, θ_d is derived from the viscous region in the vicinity to the contact line. However, this viscous region is much smaller than both the pixels of the experimental drop images and the mesh sizes of the numerical domain. Thus, the dynamic contact angles are measured at a distance with the macroscopic scale away from the solid surface, and this measured quantity is called the apparent contact angle θ_d^*. When the contact line reaches the stationary state, the drop stops spreading and is stable with the equilibrium contact angle, called the static contact angle (SCA) θ_e. In addition, several non-dimensional parameters are also important: the Reynolds number, the Weber number, the Ohnesorge number, and the Capillary number (Mukherjee & Abraham, 2007). They are defined as:

$$\mathrm{Re} = \rho D u / \mu \tag{1}$$

$$We = (\rho D u^2) / \sigma \tag{2}$$

$$Oh = \mu / \sqrt{\rho \sigma D} \tag{3}$$

$$Ca = V\mu / \sigma \tag{4}$$

Notice that V is the spreading velocity while u is the initial impact velocity. Here, Re indicates the ratio of inertial to viscous effect, while We represents the ratio of inertial to surface tension. The Oh number is the combination results of these two numbers, $Oh = \sqrt{We} / \mathrm{Re}$, and plays a key role during the spreading regime. The Capillary number Ca, widely used to define the drop spreading process, is defined as the ratio of inertial and viscosity to surface tension. However, since spreading velocity V in the Capillary number needs to be updated at each time step, numerical models involving Ca have large computational cost. Thus, we are looking for another dimensionless number to express the drop spreading process instead of Ca. By examining the physical behaviors during the spreading process, it is verified that Oh could be used to describe this regime with satisfying accuracy and low computational cost. The roles of Re, We and Oh will be discussed in Chapter 3.

In recent years, computational fluid dynamics (CFD) has been used to understand and predict the complex hydrodynamics of drop impacting and spreading on the solid surface (Bussmann et al., 2000; Bussmann et al., 1999; Gunjal et al., 2005; Lunkad et al., 2007; Pasandideh-Fard et al., 1996; Šikalo et al., 2005). Both theoretical and empirical models have been developed for numerical analysis. In particular, boundary conditions at the moving contact line of the spreading drop need to be specified in terms of contact angles. According to Young's equation

$$\sigma \cos\theta_e = \sigma_{sv} - \sigma_{sl} \tag{5}$$

static contact angle is ideally a property of the concerned system related to the surface tension of the solid/vapor σ_{sv} and solid/liquid σ_{sl} interfaces (Šikalo, et al., 2005). On the contrary, dynamic contact angle θ_d is not a material property but most depends on the capillary numbers, Ca (Šikalo, et al., 2005). However, the exact expression of

dynamic contact angle θ_d in terms of Ca is still unknown. The understanding of variable θ_d has been investigated both theoretically and empirically (Bussmann, et al., 1999; Pasandideh-Fard, et al., 1996; Šikalo, et al., 2005). When these models were applied for numerical analysis, two aspects need to be concerned: 1) the precisions of these models compared with the experimental results; 2) the physical properties and behavior information required by the models for the sake of computational cost.

Since the theoretical expression of θ_d in terms of Ca is still unclear, empirical expressions have been employed in the drop spreading studies (Cox, 1986; Hoffman, 1974; Jiang et al., 1978; Kistler, 1993). Most of the simulations predict well the shape of the spreading drop during the kinetic regime where the inertia dominates. However, the prediction of the spreading regime has not been well simulated (with more than 10% error). In addition, the complexity of existing formulas leads to high computational cost while being applied to the 3-D region. Further details are discussed in Chapter 2.1.1.

In other studies (Gunjal, et al., 2005; Lunkad, et al., 2007; Pasandideh-Fard, et al., 1996), rather than using the empirical formula, the full evolution of dynamic contact angle measured from the experiments is applied to constrain the contact line and the value of θ_d is updated after each time step. This full DCA model shows good agreement to the experimental data but large amounts of experimental measurements are required.

Table 1-1 lists the summary of previous studies which conducted the numerical simulations of drop spreading on a flat solid surface. The liquids which have been studied were limited to water and glycerin. Hence, a new generalized contact angle model is needed such that to be employed as the boundary condition in the numerical simulation in order to 1) improve the accuracy of predicting the drop shape during the spreading regime as compared with existing correlations, 2) reduce the behavior information required as compared with the full DCA model, and 3) extend the materials from water and glycerin to hydrocarbon drops.

1.2 Research Objectives and Scope

The objectives of this work are: 1) study the effect of fluid properties and impact characteristics on dynamic contact angle θ_d ; 2) develop a new model of drop behavior for hydrocarbon liquids; 3) the new model should have lower computational and experimental cost, and higher accuracy than those currently available; 4) examine the applicable range of this new model. The method for achieving these objectives is through high speed imaging of the impact of diesel and methanol drops, followed by experimental analysis and CFD simulations. In addition, the data for glycerin drops impact on a glass surface measured by Sikalo et al. (Šikalo, et al., 2005) was used to broaden the basis, showing its independent check on the computational portion. The spreading processes of these three hydrocarbon liquids were simulated and the shapes of spreading drops were compared with the experimental results. Moreover, seven different cases regarding water drop spreading on various substrates (Fukai et al., 1995; Roisman et al., 2008; M. Wang et al., 2009a) were used to investigate the applicable range of our new model. The volume of fluid (VOF) method (Hirt & Nichols, 1981), which is suited for large topology changes and has a low computational cost, was implemented by using the commercial software Fluent 12.0.16.

The thesis is organized as follows. Chapter 2 presents a general review of drop impact. The different scenarios of drop impact are displayed and relative phenomena are addressed. In particular, for drop impact on a solid surface, the models of dynamic contact angle are of great importance. These dynamic contact angle models, including the hydrodynamic and molecular kinetic ones, are also specified and compared in this chapter. Furthermore, different numerical algorithms for drop simulations, involving the volume-of-fluid (VOF) method, the level-set method, and the front-tracking method are specified and compared in this chapter.

Experimental results of hydrocarbon drops impact on the flat smooth solid surface are presented in Chapter 3. The time evolutions of dynamic contact angles and spread

factors are studied, showing the two-regime behavior after the initial collision on the wall. The two-regime behavior, a kinetic regime followed by a spreading regime, indicates that two different numerical models could be applied to each regime. A dynamic contact angle correlation, benefited from the experimental results, is proposed to describe the spreading regime. The transition time instance, from the kinetic regime to the spreading regime, agrees with a power law, changing as a function of the Reynolds number.

Chapter 4 is devoted to numerical studies of hydrocarbon drops impact on a flat smooth solid surface (glass substrate). The volume-of-fluid (VOF) method, as a popular algorithm to simulate free-surface flows and easily accessed in Fluent 12.0.16, is utilized to calculate the process of drop impacts. In addition, numerical grids and boundary conditions are presented in this chapter.

Numerical results and discussions of all the hydrocarbon drops are presented in Chapter 5. Cases with different liquid materials, impact velocities, and numerical models are compared and discussed.

Chapter 6 brings in seven different cases of water drops impact on various substrates to investigate the applicable range of our new model. Conclusions are drawn in Chapter 7, and the future work is presented in Chapter 8.

Table 1-1 Summary of Previous Studies

Authors	Liquid	Re	We	Contact Angle Model
Fukai, et al., 1995	Water	3010 ~ 8800	56.8 ~ 364	Constant Angle
Bussmann, et al., 1999	Water	1992	27	1) SCA; 2) $\theta_d = \theta_d(u)$
Pasandideh-Fard, et al., 1996	Water	2112	27	Full DCA
Gunjal, et al., 2005	Water & Mercury	750 ~ 10,300	2.78 ~ 566	Full DCA
Lunkad, et al., 2007	Water & Glycerin	27	51	Full DCA
Roisman et al., 2002	Water & Glycerin	100 ~ 10,800	25 ~ 532	Kistler's eq.
Šikalo, et al., 2005	Water & Glycerin	27 ~ 4010	51 ~ 802	Kistler's eq.
Roisman, et al., 2008	Water	N/A	0.88~1.81	Kistler's eq.
Mukherjee & Abraham, 2007	Water & Glycerin	N/A	30 ~ 246	Kistler's eq.

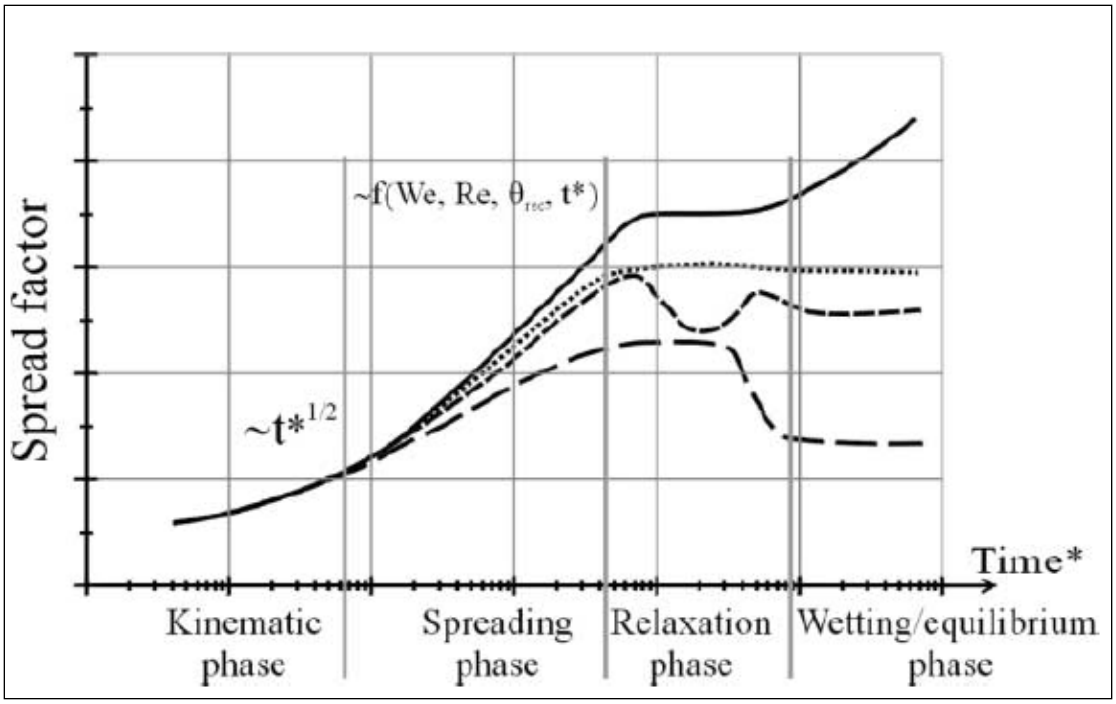

Figure 1-1 Schematic representation of the spread factor with time: the different lines correspond to an arbitrary choice of possible spreading *histories*, depending on the parameters of the impact

Source: Rioboo, R., M. Marengo, and C. Tropea, *Time evolution of liquid drop impact onto solid, dry surface.* Experiments in Fluids, 2002. **33**: p. 112-124.

CHAPTER 2: LITERATURE REVIEW

2.1 Different Scenarios of Drop Impact

Drop impacting has many different outcomes depending on the properties of drops (impact speed, geometry of the drop, surface tension, viscosity, etc.), the impacted surface (dry solid surface or liquid surface, roughness of the impacted solid surface, and wettability), and the surroundings (under normal pressure or higher pressures). An overview of different parameters that are of importance during drop impact process is listed in Figure 2-1 (Rein, 1993).

The shape of the drop varies at the moment of impact. In most experiments or simulations, the drop is considered or assumed as to be spherical. However, it also might be elliptic due to oscillation (Rodriguez & Mesler, 1988; Winnikow & Chao, 1966), or a random deformed shape (Dear & Field, 1988; Field et al., 1979), or with a shield of surfactants (Cooper-White et al., 2002; Mourougou-Candoni et al., 1997; X. Zhang & Basaran, 1997). Different drop shapes result in various impact behaviors. Typically, in this work, we are only interested in the spherical drops with a distortion within 5% (details are explained in Chapter 3).

According to the direction in which the drop impacts, scenarios of drop impact could be either normal or oblique. Numerous experimental and numerical studies were carried out to understand the normal impact (Okawa et al., 2006; Roisman et al., 2002; Šikalo, et al., 2005; A. Wang & Chen, 2000; Yarin, 2006; Yarin & Weiss, 1995), whereas studies of oblique impact of single drops are scarce (Bussmann, et al., 1999; Leneweit et al., 2005; Mundo et al., 1995; Okawa et al., 2008; Pasandideh-Fard et al., 2002; Zhbankova & Kolpakov, 1990). Even though the oblique drop impact is not a rare event in technical applications, the consequences of oblique impacts are still insufficiently studied and understood. It is generally considered that the impingement angle α (the angle between the velocity vector of the drop and the normal vector to the surface) plays

an important role in results of the oblique impact. Nonetheless, a general model implying the effect of α on the outcome of oblique drop impact is still unclear. To simplify our research scope, we only consider the normal impact in this work.

The drop may impact on a dry solid surface, on the free surface of a deep liquid pool, or on a thin liquid film. Detailed explanations to behaviors of drop impact on different surfaces are presented as follows.

2.1.1 Drop Impacts on the Liquid Surface

In the liquid-surface case, the surface of a thin liquid film is most studied to understand the mechanism of drop splashing. Most experiments were operated on the pre-existing plane liquid surfaces (Cossali et al., 1997; Cossali et al., 2004; Rioboo et al., 2003; A. Wang & Chen, 2000). However, in some experiments, droplet streams, rather than a single drop, impacted on the surfaces, and liquid films were created by impacts of previous drops. Thus, a wavy surface was present. When the surface is impacted by droplet streams, the impact frequency f plays an important role. If f is small enough, waves triggered by the previous drop could be assumed as little disturbance (Jayaratne & Mason, 1964), or it could be assumed that the liquid surface recovers between two collisions (Zhbankova & Kolpakov, 1990). In contrast, the influence of the previous drop impacting should be considered with a larger impact frequency (Siscoe & Levin, 1971; Yarin & Weiss, 1995). It is noted that the primal factors involved in a train impacting are only inertia and surface tension rather than gravity which is negligible (Yarin, 2006). Even though the characteristic times are different for the impact trains (f^{-1}) and the single drop impact (D/u), a uniform dimensionless group could be used to govern the splashing threshold (the transition from spreading to splashing) of drop impacts on liquid surface, $K = We \cdot Oh^{-2/5}$ (Yarin, 2006).

In addition to the case in which the impacted liquid is the same as the drop, the drop might impact on a different liquid film, which could be miscible or immiscible. It is also noted that the ratio of the surface tensions of the drop and the impacted liquid plays an important role in such cases (Smith, 1975).

2.1.2 Drop Impacts on the Solid Surface

In the solid-surface case, since the influences of the surface roughness and the surface wettability are involved, drop impacts are more complicated compared with the ones on the liquid surface. The drop impact on the solid surface results in three outcomes: bouncing, spreading, or splashing. Six possible scenarios of drop impact on a solid surface are exhibited in Figure 2-2 (Rioboo et al., 2001).

Right after the impact on the solid surface, the liquid drop is compressed and a shock wave is formed, attached to the contact angle. Very high impact pressures would be obtained even with small impact velocities, and the pressure rise is approximated by ρcu, where ρ is the density of the liquid, c is the sound speed in the liquid, and u is the impact speed. The drop shape is shown as a cut sphere at the initial stage, while the important properties are density, compressibility, the impact velocity and the radius of the drop. After this initial stage, the shock separates from the contact angle, no longer enclosing the compressed liquid, and the sideways jetting becomes possible. The sideways jetting either results in the motion of purely spreading or splashing.

If the drop strikes the surface with a finite velocity, the liquid starts spreading out after the formation of the contact between the liquid and the solid surface. The kinetic energy, namely inertia, of the drop plays an important role during the first regime of spreading as mentioned in Chapter 1. The drop expands rapidly aligned with the wall as a thin liquid disk, called a lamella, as shown in the first row in Figure 2-2. Then the kinetic energy is partly dissipated by viscous forces, and partly converted into surface energy as the free surface area is greatly increased. If most of the available kinetic energy is

dissipated by the viscous forces, the expanding lamella should reach its maximum diameter and remain this diameter d_a (the subscript a denotes advancing). After the maximum diameter is achieved, some liquid still flows from the center part of the lamella outward. This leads to the accumulation of liquid near the rim. The accumulation of the liquid rim is the starting point where the capillary waves run towards the center part. The capillary waves run back and forth until the kinetic energy is fully dissipated and the lamella is at rest as an equilibrium shape. For liquids with low viscosities, the contact line might start to recede from the maximum diameter, associated with the propagation of the capillary waves. If the receding velocity is sufficiently slow, then the receding lamella will stop at d_r (the subscription r denotes receding). However, at high receding velocity, the receding lamella might pass through d_r and breaks up into smaller droplets due to the capillary instability, as shown in the fourth row in Figure 2-2. It is proposed that the recoiling behavior could be scaled by the Ohnesorge number Oh since the recoiling flow is resisted by inertia and viscosity (Kim, Chun, J. -H.). The drops would recoil faster and more vigorously as the Ohnesorge number decreases.

At high impact velocity, the drop might disintegrate into some secondary drops after impacting on a solid surface, called splashing. Drop splashing includes two different morphologies: corona splashing and prompt splashing. In the case of drop spreading, if the drop spreads on the solid surface with a small surface tension, the lamella might detach from the wall and move upward, resulting in a crown shape, called corona. The corona breaks up into droplets, and then, these secondary droplets are ejected upward from the corona (Lei Xu, 2007), as shown in the third line in Figure 2-2. The other form of splashing is prompt splashing, which appears at the last stage of the spreading and results in drop being ejected radially outward, in-line with the leading edge. Xu and coworkers claimed the differences between corona and prompt splashing are the causes which induce the splashing behaviors: environmental pressure is important for corona splashing while surface roughness triggers prompt splashing (Lei Xu, 2007).

The transition from the spreading to splashing, namely, the splashing threshold, remains an important issue for studies of drop impacts on the solid surface. Compared with the splashing threshold for the drop impacts on the liquid surface, which is characterized as the dimensionless group $K = We \cdot Oh^{-2/5}$, the splashing threshold for the cases with the solid surfaces is more complicated. A splashing ratio Σ_G / Σ_L is defined and found to be constant for all liquids in the regime above their critical impact speeds (L. Xu, et al., 2005),

$$\frac{\Sigma_G}{\Sigma_L} = \frac{P_T}{\sigma}\sqrt{\gamma M_G}\sqrt{\frac{R_0 V_0}{2k_B T}}\sqrt{\nu_L} = 0.45 \tag{6}$$

Here Σ_G is defined as a dimensionless parameter related to the restraining pressure of the gas on the spreading liquid, acting to destabilize the advancing front and deflect it upward; whereas, Σ_L is defined to be the effect of the surface tension of the liquid.

$$\Sigma_G \sim (\rho_G)(C_G)(V_e) \sim \frac{P_T M_G}{k_B T}\sqrt{\frac{\gamma k_B T}{M_G}}\sqrt{\frac{R_0 V_0}{2t}} \tag{7}$$

$$\Sigma_L = \sigma / d = \sigma / \sqrt{\nu_L t} \tag{8}$$

where, σ and ν_L are the surface tension and kinematic viscosity of the liquid, respectively, R_0 and V_0 are the initial radius and impact speed of the drop, M_G is the actual mass of on molecule of the gas, γ is the ratio of its specific heats, k_B is the Boltzmann' constant, P_T is the threshold pressure at which splashing occurs, t is the time measured from the instant of impact, C_G is the speed of sound in the gas, ρ_G is the gas density, V_e is the expanding velocity of the liquid layer on the substrate, and T is the gas temperature. Thereafter, it is indicated that a drop with a splashing ratio Σ_G / Σ_L greater than 0.45 is likely to splash and the splash would not occur with the ratio less than 0.45. It is also suggested that splashing is caused by the Kelvin-Helmholtz (K-H) instability mechanism (Jepsen et al., 2006; Lei Xu, 2007), and the associated empirical splashing

threshold is proposed based on the capillary number (Liu et al., 2010). Except for the surrounding gas and the roughness of the solid surface, the effects of other factors on the splashing threshold have also been studied. It is noted that splashing on a smooth surface is caused by the air entrainment of the spreading lamella (Jepsen, et al., 2006; Rein & Deplanque, 2008). The impact speed, drop size, liquid viscosity, and surface tension also have an effect on the tendency of splashing (Engel, 1955; Levin & Hobbs, 1971; Scheller & Bousfield, 1995; Šikalo et al., 2002; L. Xu, et al., 2005; X. Zhang & Basaran, 1997). Associated with these properties, more models of splashing threshold have been proposed (Cossali, et al., 1997; Mundo, et al., 1995; Range & Feuillebois, 1998; Stow & Hadfield, 1981; Vander Wal et al., 2006).

In some cases, with sufficient high impact velocity, the kinetic energy might not be fully dissipated by the viscous effects at the end of the spreading stage and squeezes the liquid upward from the contact surface. This rising liquid volume might be fully detached from the surface, namely, fully rebound (as shown in the last row of Figure 2-2), or it might be partially detached from the surface and eject one or more secondary droplets, called partial rebound (as shown in the fifth row of Figure 2-2). Partial rebound is enhanced by decreasing the viscosity or increasing the contact angle between the liquid and the solid surface (Mao et al., 1997).

2.2 Theoretical Interpretation of Dynamic Contact Angle

When a liquid drop is deposited on a solid surface, the equilibrium shape of the liquid achieved depends on the properties of the liquid and the solid. The equilibrium shapes include two different scenarios: a sessile drop (Figure 2-3a) and a coating film (Figure 2-3b). The former form is called partial wetting while the latter one is total wetting. According to Young's relation, the equilibrium condition that relates the angle θ_e to the surface energies can be deduced as

$$\cos\theta_e = \frac{\sigma_{sv} - \sigma_{sl}}{\sigma} \tag{9}$$

If the right hand side of the above equation is larger than 1, then the equilibrium contact angle θ_e is equal to zero such that the liquid layer would expand on the surface as much as it can, called total wetting. On the other hand, when $0 < \theta_e < \pi$, partial wetting occurs.

The contact angle is the key boundary condition in drop spreading. It is defined as the angle formed between the moving liquid interface and the solid surface at the line of three-phase contact (as shown in Figure 2-4). When the contact line reaches the stationary state, the drop stops spreading while the contact angle varies in a range of values including the equilibrium contact angle, called the static contact angle (SCA) θ_e. The maximum value of the contact angle in this range is called advancing contact angle θ_a, while the minimum value of the contact angle in this range is called receding contact angle θ_r. These two angles are in the limit as $V \to 0$ with $V > 0$ and $V < 0$ respectively (as shown in Figure 2-5). Note the wettability of the substrate is related to these two values, θ_a and θ_r.

The moving wetting line and its associated dynamic contact angle were interpreted in different ways in earlier days. For example, chemists would consider them as the displaced equilibrium, while physicists preferred to use friction to describe them. Engineers are interested in two approaches: the hydrodynamic theory and the molecular kinetic theory (Blake, 2006).

2.2.1 Hydrodynamic Theory

The hydrodynamic theory emphasizes dissipation due to viscous flow within the wedge of liquid near the moving contact line (Cox, 1986; de Gennes, 1985; Dussan V., 1979; Hansen & Toong, 1971; Hocking & Rivers, 1982; Huh & Scriven, 1971; Tanner, 1979; Voinov, 1976). People who are using the hydrodynamic theory face two primary

problems related to the moving contact-line condition: 1) how to describe the behavior of macroscopic contact angle; 2) how to remove the shear-stress singularity (Shikhmurzaev, 1997). The following approaches could be found to solve Problem 1 in the literature.

(1) $\theta_d \equiv \theta_e$ (Cox, 1986; Dussan V., 1976; Hocking, 1977, 1992; Hocking & Rivers, 1982; Zhou & Sheng, 1990)

(2) $V = k(\theta_d - \theta_e)$, where k is an empirical constant (Greenspan, 1978; Haley & Miksis, 1991; Hocking, 1990).

(3) $V = k(\theta_d - \theta_e)^m$, where k and m are either empirical constant (Ehrhard & Davis, 1991), or the modified assumption (Braun et al., 1995; Goodwin & Homsy, 1991) according to Tanner's Law (Tanner, 1979).

(4) $\theta_d \equiv 180°$, implying that the fluid is inviscid and relaxing no-slip boundary condition is not considered (Baiocci & Pukhnachev, 1990; Pismen & Nir, 1982; Pukhnachev & Solonnikov, 1983).

In the above approaches, θ_d is denoted as the macroscopic contact dynamic angle, formed by the tangent plane to the free surface and the solid wall. The macroscopic contact angle is derived from the viscous region in the vicinity to the contact line. However, in experiments, this viscous region is much smaller than both the pixels of the experimental drop images and the mesh sizes of the numerical domain. Thus, the dynamic contact angles are measured at a distance with the macroscopic scale away from the solid wall, called the apparent contact angle θ_d^* (as shown in Figure 2-6, $\theta_d^* \approx \theta_{app}$).

The well-known singularity of hydrodynamic approach is raised from the conflict between the moving contact line and the conventional no-slip boundary condition. The classic fluid dynamics dictates that the tangential component of velocity at the wall should be set to zero due to the no-slip boundary condition, whereas the gas-liquid-solid contact line moves along the wall, resulting in a non-zero tangential (spreading) velocity at the wall.

To get rid of the shear stress singularity which is raised from the no-slip boundary condition, several approaches have been developed to solve this problem:

(1) The classical Navier boundary condition: $\boldsymbol{n}\cdot\boldsymbol{P}\cdot(\boldsymbol{I}-\boldsymbol{nn})=\beta(\boldsymbol{u}-V)$ (Lamb, 1932), where β is the coefficient of sliding friction. The value of β is either constant (Ehrhard & Davis, 1991; Haley & Miksis, 1991; Hocking, 1977, 1990, 1992; Hocking & Rivers, 1982; Levine et al., 1980; Zhou & Sheng, 1990) or a function in terms of the thickness of the lamella *h* (Braun, et al., 1995; Goodwin & Homsy, 1991; Greenspan, 1978; Haley & Miksis, 1991).

(2) The distribution of the spreading velocity is prescribed in terms of the slip length and the drop diameter (Dussan V., 1976; Finlow et al., 1996; Zhou & Sheng, 1990).

It is apparent that the existing problem is how to combine the two existing problems as mentioned above into one theory. Some authors have related the spreading velocity with the dynamic contact angle with semi-empirical approaches. One of these semi-empirical approaches is to cut off the singularity of the shear stress near the wall and exert a finite force on the solid (Voinov, 1976). However, such an approach would lead to the breakdown of continuum mechanics modeling. Alternatively, understanding the existing difficulty, people replace the value of apparent contact angle, which is at a certain distance from the contact line, with a prescribed function of the spreading velocity or some other parameter (Boender et al., 1991; Cox, 1986; Jiang, et al., 1978; Kistler, 1993; Voinov, 1976).

One important semi-empirical approach to solve both the problems is the analysis proposed by Cox (Cox, 1986): the evolution of dynamic contact angle θ_d is related to capillary number Ca and static contact angle θ_e, as displayed below

$$Ca=\frac{g(\theta_d)-g(\theta_w)}{\ln(\varepsilon^{-1})-\frac{Q_0^{*}}{f(\theta_d)}+\frac{Q_0^{*}}{f(\theta_w)}}+O\left(\frac{1}{\ln(\varepsilon^{-1})}\right)^3 \tag{10}$$

where θ_w is the microscopic contact angle, associated with the static contact angle θ_e. Q_0^* is the constant determined by the entire flow field in the inner region. ε is defined as the ratio of slip length s to the characteristic macroscopic length R. Since the slip between the liquid and the solid surface must occur at a very small distance from the contact line, the value of s is expected to be quite small, in the order of a molecular size. Thus, it is assumed that:

$$\varepsilon = \frac{s}{R} << 1 \tag{11}$$

Another novel and popular empirical correlation between the dynamic angle and spreading velocity was proposed by Kistler (Kistler, 1993) and it has been employed as the boundary condition by Sikalo et al. (Šikalo, et al., 2005), Roisman et al. (Roisman, et al., 2008; Roisman, et al., 2002), and Mukherjee et al. (Mukherjee & Abraham, 2007). The form is:

$$\theta_d = f_H[Ca + f_H^{-1}(\theta_e)] \tag{12}$$

where f_H^{-1} is the inverse function of the "Hoffman's function" f_H defined as

$$f_H(x) = \arccos\{1 - 2\tanh[5.16(\frac{x}{1+1.31x^{0.99}})^{0.706}]\} \tag{13}$$

It is noted that both Cox's and Kistler's correlation use capillary number Ca and static contact angle θ_e to express the evolution of dynamic contact angle θ_d. Namely, according for the definition of capillary number $Ca = V\mu/\sigma$, the dynamic contact angle varies with the instantaneous spreading velocity.

2.2.2 Molecular Kinetic Theory

Even though surface phenomena and intermolecular forces have been considered in the hydrodynamic theory, only the shape of fluid/gas or fluid/fluid interface near the wetting line is influenced. Moreover, because of the treatment of no-slip boundary

condition, the molecular details of the region in vicinity to the wetting line have been considered not only intractable, but also relatively unimportant. In contrast, the molecular kinetic theory provides a molecular view for slip at the wetting line and emphasizes the role of molecular events occurring within the three-phase zones as the controlling influence on the wetting process (Berg, 1993). The basis for this approach is the statistical mechanics treatment of transport processes developed by Eyring (Glasstone et al., 1941) and Frenkel (Frenkel, 1946). Dissipation due to viscous flow is discarded in this theory. Instead, as shown in Figure 2-7, it focuses on the process in which the fluid molecules attach or detach to or from the solid surface at the immediate vicinity of the wetting contact line (Blake, 2006). This theory is first adopted by Cherry and Holmes (Cherry & Holmes, 1969) and by Blake and Haynes (Blake & Haynes, 1969), and is supported more recently by Ruckenstein and Dunn (Ruckenstein & Dunn, 1978) and by Miller and Neogi (Miller & Neogi, 1985).

In the molecular kinetic theory, the motion of the contact line is determined by the statistical dynamics of the molecules within its immediate vicinity. Two parameters are important here: 1) κ°, the equilibrium frequency of the random molecular displacements occurring along the contact line; 2) λ, the average distance of each displacement. The resulting equation for the contact-line velocity is then

$$V = 2\kappa^{\circ}\lambda \sinh[\sigma(\cos\theta_s - \cos\theta_d)\frac{\lambda^2}{2k_B T}] \tag{14}$$

where k_B is the Boltzmann constant and T is the temperature.

This contact angle dependent velocity has proven successful with the experimental investigation in a wide range (Blake & Haynes, 1969; Hopf & Geidel, 1987; Petrov & Radoev, 1981; Schwartz & Tejada, 1970, 1972; Ström, Fredriksson, & Stenius, 1990; Ström, Fredriksson, Stenius, et al., 1990). It is noted that the microscopic contact angle is usually obtained as a result of molecular dynamics (MD) simulation (Gentner et al., 2004; He & Hadjiconstantinou, 2003). In particular, MD simulations only

consider the drops with the nanometer sizes (~10 ns) and the results of the simulations do not necessarily correspond to the characteristics of macroscopic drops (Yarin, 2006).

2.3 Numerical Algorithms for Drop Computations

Numerical methods available for the description of free-surface flows are based on the full Navier-Stokes equations. The problem is obviously difficult and a large number of methods have been dedicated to solve it. Here, a brief description of several widely-used approaches is presented as follows.

Numerical approaches for solving the free-surface problems are on the basis of moving or fixed grids. Surface fitting methods are typical examples using moving grids. They solve for the flow within the liquid region only, and the free surface is replaced at the boundary of the computational domain. The coordinate transformation helps to map the moving, body-fitted coordinate system in physical space to a fixed, uniformly spaced coordinate system in computational space (Kelecy & Plethcer, 1997). When the topology is significantly changed or highly distorted, mesh reconstruction is needed to remove the singularity.

In contrast, fixed-grid methods avoid the grid-related problems, can be easily extend to three dimensional problems, and have less expensive numerical cost compared with the moving-grid ones. Generally speaking, there are two broad categories using fixed-grid algorithms: surface capturing and surface tracking. The main difference between surface capturing and surface tracking algorithms is the method with which the interface is identified. In capturing methods, the interface is “captured” and reconstructed based on the indirectly related information propagated with the flow, such as the volume of fluid (VOF) method and the level set method. In contrast, the surface tracking method, e.g. the front tracking method, consists of the explicit tracking of the interface with Lagrangian algorithm (Rein, 2002).

The volume-of-fluid method (VOF), first developed by Hirt and Nichols (Hirt & Nichols, 1981), is based on the earlier marker and cell (MAC) method (Harlow & Welch, 1966). The general idea of the VOF method is to use an idea of so-called fraction function α_k to describe the interface. When the cell is full of fluid, $\alpha_k = 1$; when the cell is empty, $\alpha_k = 0$; and when the cell contains the interface, $0 < \alpha_k < 1$. The challenge is to reconstruct the interface accurately solely based on the value of α_k. The Piecewise Linear Interface Construction (PLIC) is introduced to solve this problem, by using straight lines (planes in three dimensions) to cut through the cell at a suitable inclination. Implementation of the volume-of fluid method is relatively simple in both two and three dimensions and it can naturally simulate the geometrically complex change (e.g. collision or merge). Further, mass conservation is always sustained in this method. Beyond these advantages, the main drawback of this method is the less accurate reconstruction of the interface on the basis of fraction function α_k. However, this drawback is no longer necessary for certain applications where a smaller scale than a grid cannot be solved, e.g. detachment of the small drop from the surface (Rein, 2002). The detail explanation about the VOF method is presented in Chapter 4.1.

The level set method, invented by Osher and Sethian (Osher & Sethian, 1988), applies the level set field $\phi(\boldsymbol{x}, t)$ representing signed distance functions. This signed distance function is initialized at $t = 0$ as zero in the interface, and $\phi < 0$ denotes that the field is inside the liquid while $\phi > 0$ means that the field is outside the liquid. The motion of the interface evolves by solving the Hamilton-Jacobi equation, which allows for the formation of shocks. In this setting, dissipation or diffusion term is missing such that the noises cannot be move out, e.g. the singularity at the tip of highly skewed curvature could not be removed, leading to instability. A native approach using the entropy-satisfying schemes is introduced to produce the correct viscosity solution. However, since numerical errors can cause the loss of mass conservation, mass conservation is a persistent problem in the level set method.

Other than the above two methods, the front-tracking method, developed by Tryggvason and co-workers (Tryggvason et al., 2001), tacks the interface explicitly on the basis of a moving grid of lower dimension. The explicit Lagrangian tracking improves the accuracy of the calculation of local geometric properties. This method also allows the existence of two interfaces in one cell without coalescence which is enforced by the above two approaches. Nevertheless, the coding of this explicit approach is more complex since the points at the interface need to be added or deleted as time evolves. Furthermore, as this method avoids automatic coalescence within one cell, topology changes involving merges or break-ups become difficult.

In spite of the three described approaches, several other methods are also used to deal with the free-surface problem. For example, the boundary-fitted coordinate methods (Ryskin & Leal, 1984), lattice-Boltzmann methods (Chen & Doolen, 1998), the phase-field model (Jacqmin, 1999), and others are of particular interests.

Compared with other approaches, mass conservation is always maintained in the VOF method, and it can be used for calculating large topology changes with a lower computational cost. Also, it can be easily accessed from Fluent 12.0.16. Therefore, the VOF method is utilized in this work to simulate the spreading process of drop impacts.

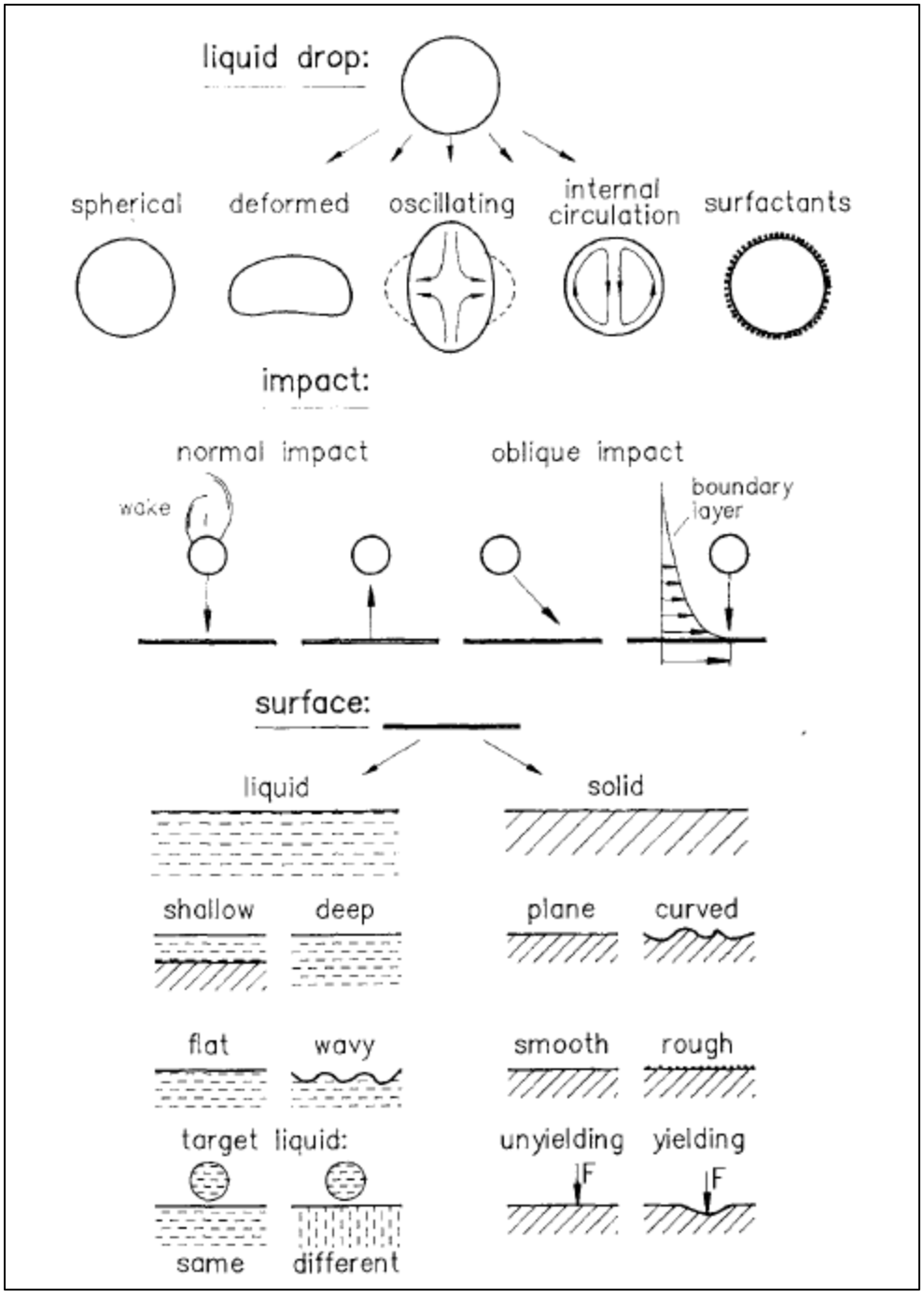

Figure 2-1 Survey of parameters governing the impact of a liquid drop

Source: Rein, M., *Phenomena of liquid drop impact on solid and liquid surfaces.* Fluid Dynamics Research, 1993. **12**: p. 61-93.

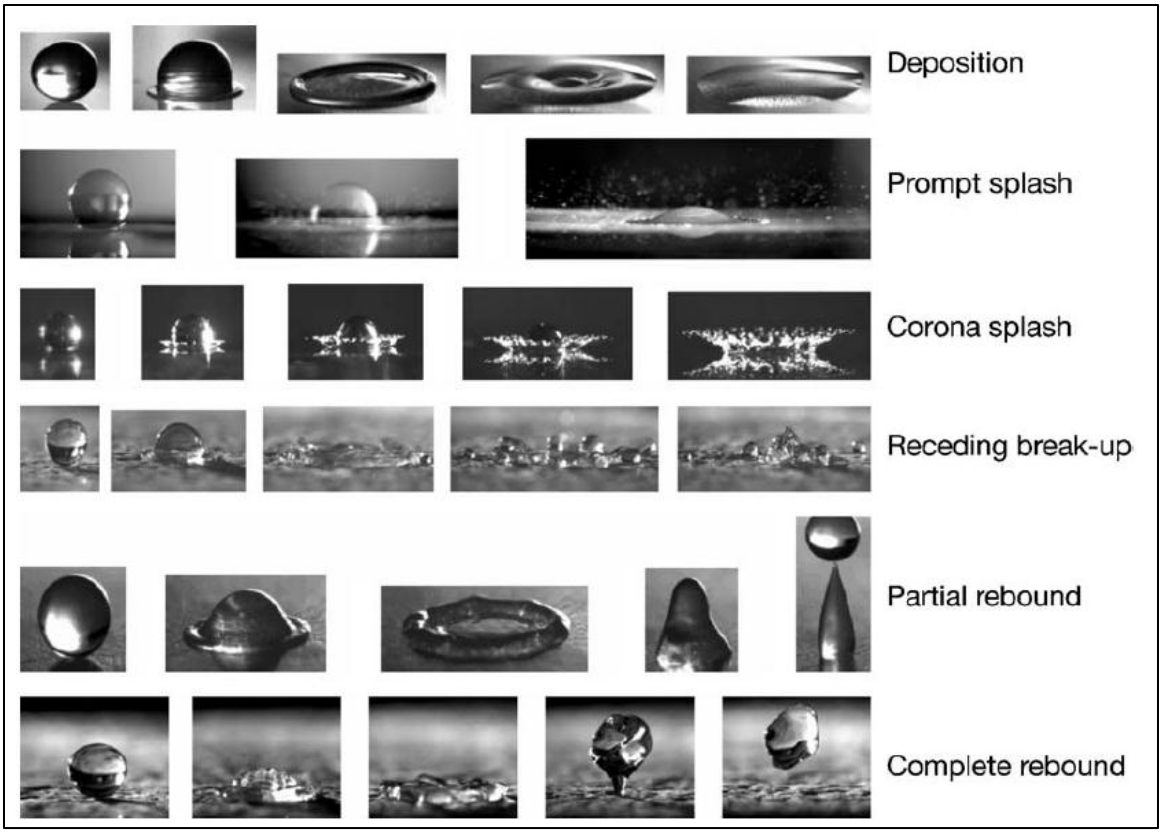

Figure 2-2 Different scenarios of drop impacts on the solid surfaces

Source: Rioboo, R., C. Tropea, and M. Marengo, *Outcomes from a drop impact on solid surfaces.* At. Sprays, 2001. **11**: p. 155-165

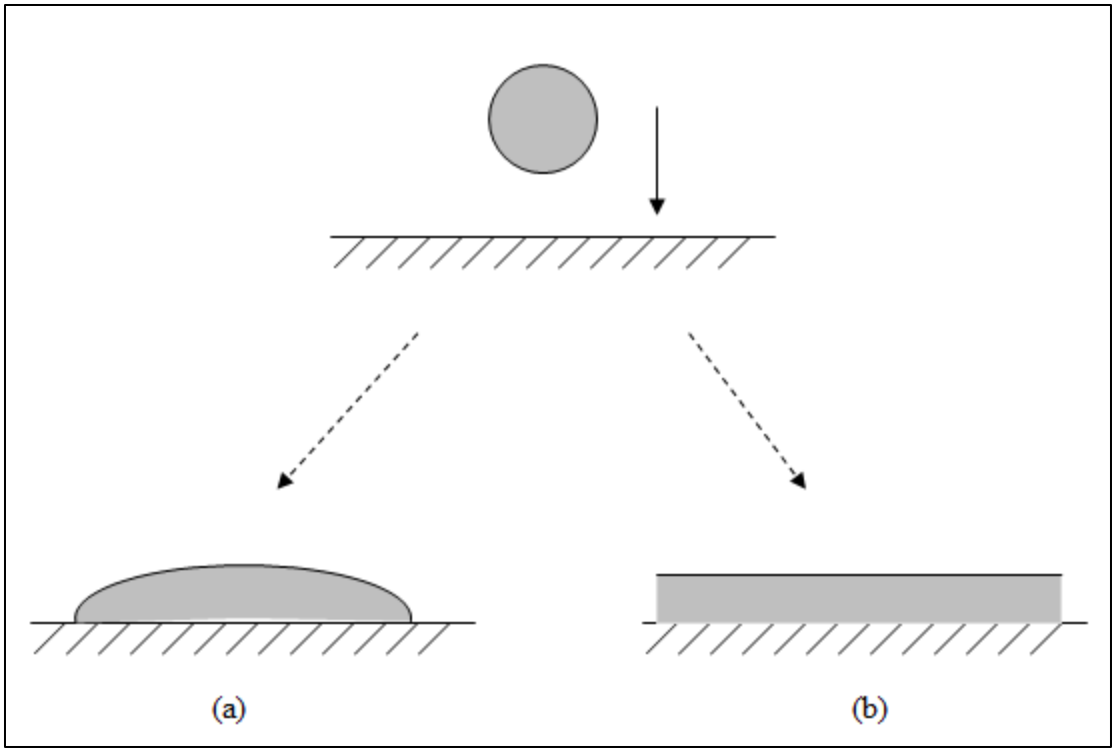

Figure 2-3 Partial wetting and total wetting

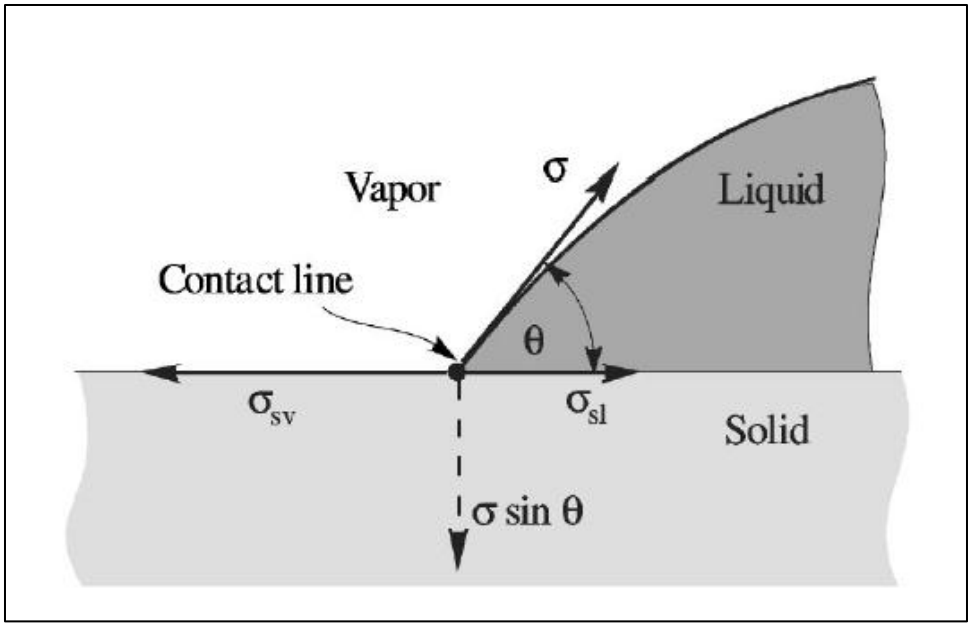

Figure 2-4 Equilibrium wetting line and contact angle

Source: Šikalo, Š., et al., *Dynamics contact angle of spreading droplets: Experiments and simulations.* Physics of Fluids 2005. **17**(062013): p. 1-13.

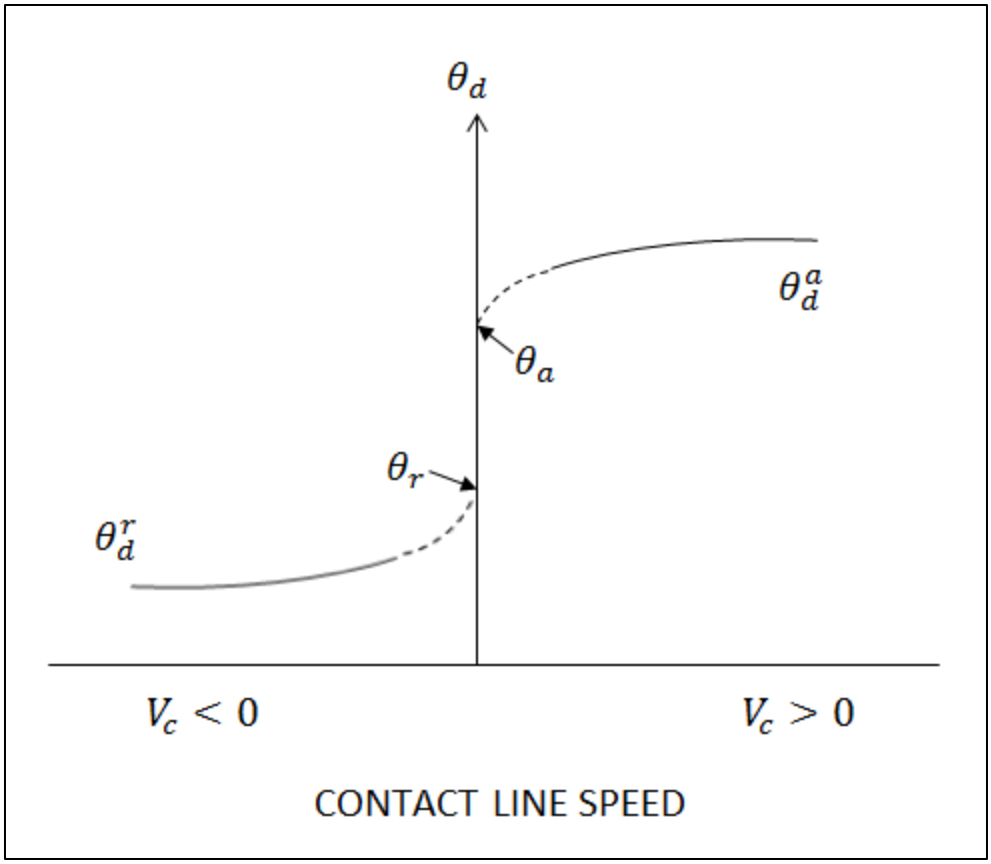

Figure 2-5 Velocity-dependence of the dynamic contact angle showing static advancing θ_a and receding θ_r limits when $V \to 0$ for a partially wetting liquid

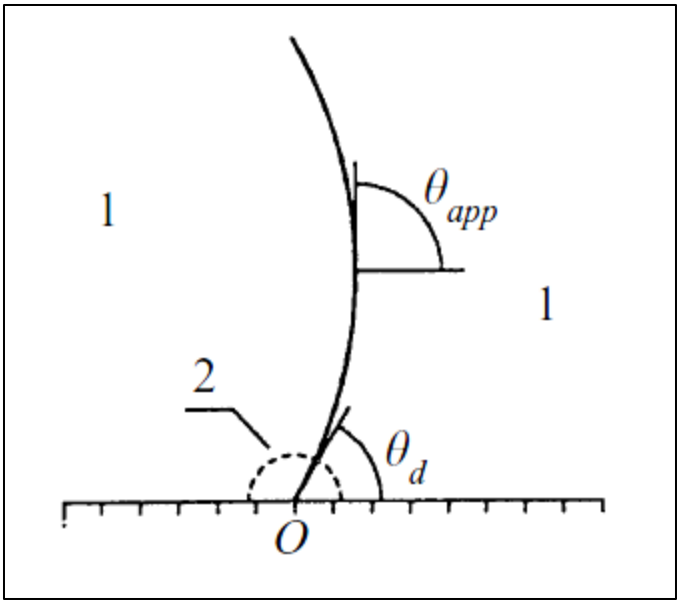

Figure 2-6 Schematic view of apparent contact angle and macroscopic contact angle

Source: Shikhmurzaev, Y.D., *Moving contact lines in liquid/liquid/solid systems.* J. Fluid Mech., 1997. **334**: p. 211-249.

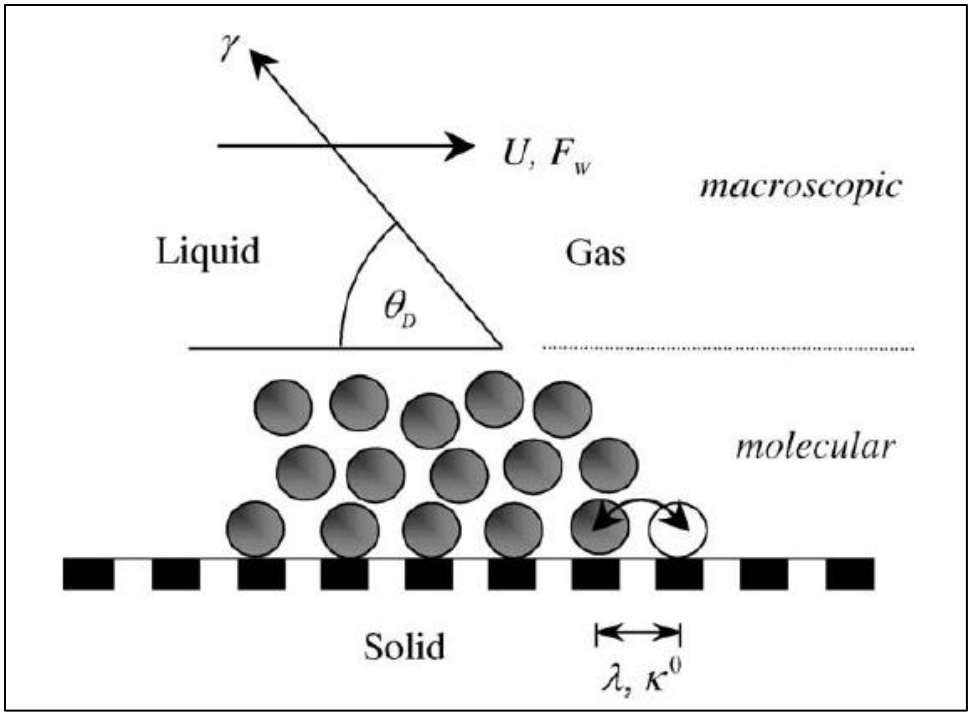

Figure 2-7 Dynamic wetting according to the molecular-kinetic theory

Source: Blake, T.D., *The physics of moving wetting lines.* Journal of Colloid and Interface Science, 2006. **299**: p. 1-13.

CHAPTER 3: EXPERIMENTS

3.1 Experimental Arrangement

The experiments were performed inside a pressure chamber with a $6" \times 6" \times 6"$ working volume, as shown in Figure 3-1 (N. K. Mishra et al., 2011). Four C-sections made of steel were welded together to form the side-walls of the chmaber. Four 44 mm thick transparent windows were affixed in the C-sections for viewing the drop impact behavior. Pressurized nitrogen could be supplied to the chamber through a pipe from an external gas cylinder to pressurize the chamber to a selected value. In this work, the chamber was open and the tests were performed under the atmospheric pressure. A quartz table smoothed to 0.2 μm across any 2 inches diameter and fixed inside the pressure chamber was used as the impact surface. Since certain materials can contaminate the surface, a new piece of glass was replaced on the top of the quartz table after each run.

Test drops were released from the blunt-end hypodermic needle at different heights, impacting on the solid surface with various impact speeds. Two different needles with the sizes of 23 ga and 17 ga were used to generate drops roughly 2.1 mm and 2.7 mm in diameter, respectively. The height of the needle could be adjusted by assembling additional pipe elements. Test liquid was controlled by a PVC pipe with a ball valve and a needle valve to be supplied from an overhead reservoir to the needle. Here, diesel was released from the needle with the size of 23 ga and methanol was from the one with the size of 17 ga. An IDT XStream-Vision XS-3 digital camera with a Nikon 105mm f/2.8D Micro-Nikkor lens was used for imaging the impacting drops, and it was placed almost normal to the direction of incidence. The camera was set to capture images at about 3000-4000 fps. Thus, the time interval between two recorded images ranges from 0.248 ms to 0.326 ms. The resolution of recorded images was well focused up to 0.014 mm/pixel. Impacts were recorded against a bright background created by a 300W projector lamp to

obtain very clear images of the deforming drop. Full experimental arrangement is available in Mishra's work (N.K. Mishra, 2009).

3.2 Experimental Observations

In this work, diesel (truck diesel, purchased from the gas station) and methanol (Methanol Acs Grade, purchased from Research Products International Corp.) drops were tested, and the cases of glycerin done by Sikalo et al. (Šikalo, et al., 2005) were used to broaden the basis. All the three hydrocarbon drops were released and impact on the glass surface. Table 3-1 shows the properties of the three materials. It is noted that diesel and methanol have fairly close surface tensions (28.0 mN/m and 22.7 mN/m), whereas that of glycerin is much higher (63.0 mN/m). Since surface tension plays an important role in the spreading process, the difference between σ leads to various spreading behaviors, which will be explained in details later.

For each material, three different impact velocities were tested as shown in Table 3-2. The fuel drops have roughly the same diameters (diesel ~ 2.16 mm; methanol ~ 2.63 mm; glycerin ~ 2.45 mm) whereas the impact velocity ranges from 0.7 to 3 m/s. Note, the drop size is not only dependent on the needle size, but also influenced by the needle valve opening and the height of the needle. Therefore, even though each diesel/methanol drop was released from the same needle, the drop initial diameters were slight different in each case. Moreover, under such impact velocities (as shown in Table 3-2), all test drops showed a spreading behavior after impact on the solid surface instead of splashing or bouncing.

10 to 15 runs were repeated for each case under the same condition to average out the minor variations of measurements. Figure 3-2 shows 5 runs (out of 15 runs) for a diesel drop impact on the surface with initial speed u = 1.6 m/s. By comparing the diesel drop diameter at the same time instance (with interpolation), the biggest variation of drop

diameter is 4.7%, which occurs at $t = 0.07$ ms. For each case (the same liquid impact with the same speed), the average drop diameter and contact angle at the same time instance were calculated by taking the arithmetic mean of all values. It is noticed that for each case the drop size varies within 5% across all the repetitions. In contrast, due to the limitation of the image pixel, the variation of contact angle during the early kinetic regime is up to 10%. Nonetheless, such a big variation could be ignored since the value of dynamic contact angle does not have an effect on the early regime (kinetic regime) of drop spreading process. Only kinetic energy dominates this regime, which would be explained in details later.

The drop diameters were read from the recorded pictures in terms of number of pixels and then converted into millimeters by using a calibration factor. This calibration factor was calculated from the image of a scale taken in the same focal plane as the drops (N. K. Mishra, et al., 2011). We selected uniform drops in shape for analysis. Since drops were not perfect spheres at the instance before impacting on the surface, an equivalent drop diameter was implemented in our analysis. This equivalent drop diameter was calculated as $D_{eq} = (D_V^2 D_H)^{1/3}$, where D_V and D_H are the diameters measured in vertical and horizontal level separately. The distortion of the drop was calculated as the ratio of difference in the horizontal and the vertical diameters to the equivalent drop diameter, $distortion = |D_V - D_H| / D_{eq}$. The valve opening was carefully adjusted to minimize the distortions, and drops with distortions beyond 5% were discarded for being out of shape.

By aligning a tangent to the image of the drop at the contact point, apparent dynamic contact angles were measured by using MB-Ruler (a triangular screen ruler).

The uncertainty in the measurement of contact angles arises due to difficulty in accurately defining the contact point where liquid/air/solid intersects. Therefore, this uncertainty is affected by the resolutions of pictures. Another primal experimental uncertainty lies in the time measurement, since the exact impact time has to be

interpolated between two exposures. All uncertainties are at 95% level of confidence by repeating measurements.

Figure 3-3 shows an example of a diesel drop impact on the glass surface with an initial speed $u = 1.6$ m/s. After the initial collision on the surface ($t < 0.78$ ms), the drop shape is like a truncated sphere, while a lamella is formed and ejected from the base of drop. Inertial effects dominate this early spreading of the drop; thus, it is called kinetic regime. With increasing time ($2.78 > t > 0.78$ ms), the truncated sphere disappears and the lamella spreads outwards. This second regime is noted as spreading regime, where viscous and surface tension forces arrest the spreading. After the lamella reaches its maximum diameter ($t > 2.78$ ms), most kinetic energy of the drop has been dissipated, leaving the capillary waves moving back and forth. Finally, the drop is brought to its equilibrium configuration by viscous and surface tension effects. This regime is named as relaxation regime. During the relaxation regime, as the spread diameter doesn't change for all three hydrocarbon liquids, this regime is of little interest in this work and experimental data (e.g. β and θ_d^*) were not measured and analyzed.

A series of pictures captured a methanol drop impact on the glass surface with an initial speed $u = 2.33$ m/s is shown in Figure 3-4. Similarly, the methanol drop experiences three regimes: the kinetic regime, the spreading regime and the relaxation regime. Since the viscosity of methanol is much less than that of diesel, the viscous effect on the spreading regime of methanol is smaller. Therefore, the methanol drop spreads much faster (ended with $d_{\max} \sim 14$ mm) and generates thinner lamella (ended with $h_{\min}$ ~0.06mm).

3.2.1 Evolution of the Apparent Dynamic Contact Angle

The trends of apparent dynamic contact angle θ_d^* are investigated for both diesel and methanol drops based on our experimental pictures.

The values of the apparent dynamic contact angle during the drop spreading have been experimentally measured and scaled in terms of the non-dimensional time *tu/D*. Two apparent regimes are visible in the trends of θ_d^* for both diesel drops and methanol drops (shown in Figure 3-5a and 3-5b) corresponding to the kinetic regime (Regime I) and spreading regime (Regime II) separately. As shown in Figures 3-3 and 3-4, the evolutions of θ_d^* are disguisable because the shapes of the drop are different during these two regimes. The value of θ_d^* roughly remains as constant during the kinetic regime and shows a significant decrease in the spreading regime.

In addition, the evolutions of the glycerin drops from Sikalo et al.'s study (Šikalo, et al., 2005) are also compared with ours. As shown in Figure 3-6, the contact angles of the glycerin drops first shows a slight decrease down to around $140\,°$ (Regime I). Then θ_d^* climbs up to about $150\,°$ (Regime II) and finally present a significant decrease with time (Regime III). Here, Regime III is the relaxation regime where the drop has stopped spreading, leaving with the capillary waves moving from the leading edge of the lamella to the center of the drop. Again, the behaviors during Regime III are not considered in this work since most kinetic energy has been dissipated before this regime. It is noted that during Regime II (spreading regime) the contact angles of glycerin drops are increasing with time (Figure 3-6) rather than decreasing as displayed by diesel and methanol drops (Figure 3-5). This is because the surface tension of glycerin is three times higher than the ones of methanol and diesel. Therefore, higher σ supports stronger stiffness for glycerin drops standing, leading to the accumulation of lamella during the spreading regime. Thus, the value of contact angle is increasing with time with the accumulated lamella. In contrast, lower σ offers less stiffness for methanol and diesel drops standing, resulting in the relaxation of lamella. In such a case, contact angles of glycerin drops show an increasing trend during Regime II, whereas the ones of diesel and methanol drops are decreasing. Figure 3-7 exhibits the images of a diesel and a glycerin drop in Regime II separately.

By cutting off Regime I in Figure 3-5 and 3-6 and rescaling the timeline, it is evident that the values of θ_d^* have the same trends during the spreading regime for the drops with different impact velocities. Note that the rescaled dimensionless time $t^{**} = tu / D - t^*$, where t^* is the dimensionless transition time instance, transferring from the kinetic regime to the spreading regime. The coincided trends are shown in Figure 3-8 and 3-9 for each hydrocarbon drop.

The dimensionless transition instance of the two-regime spreading behavior was plotted in terms of Reynolds number (Figure 3-14). As noted by the figure, the dimensionless switch time t^* grows according to a power law, $t^* = 0.05\,\mathrm{Re}^{0.45}$. This power law shows the transition instance is related to the trading between kinetic energy and viscous effect. Note, even though a power law could be derived across different liquids, for each liquid (e.g. diesel), the transition time is actually linearly increasing with increased Reynolds number. Moreover, switch time t^* is also plotted out in terms of Weber number in Figure 3-15. Apparently, there is no uniform trend could be observed across different liquids from this figure, but for each liquid t^* increases linearly with increased Weber number.

The two distinguishable regimes (Regime I & Regime II) indicate that two different numerical models could be applied for the contact angles as the boundary conditions separately, which will be discussed in Chapter 3.2.3.

3.2.2 Evolution of the Spreading Diameter

To assess the accuracy of simulation, the spreading diameter of the drop was measured and compared with the computational result. By plotting the evolutions of spread factor, $\beta = d / D$, a two-regime behavior could be also recognized for all three hydrocarbon drops: a kinetic regime followed by a spreading regime.

Rioboo et al. (Rioboo, et al., 2002) showed that the spread factors for water, silicone oil and isopropanol grow according to a power law in time during the kinetic region. This power law is approximately to $2.8(tu/D)^{0.5}$. Figure 3-10 shows that spread factors of hydrocarbon drops also increase according to this power law during the kinetic regime with the error around $\pm 14\%$. This is consistent with the conclusion that kinetic regime can be completely described by the impact velocity and initial diameter (Rioboo, et al., 2002).It is noted that the kinetic regime displayed in Figure 3-10 ends at the instance when the evolution of the contact angle shows a significant decrease or increase.

Figure 3-11 shows evolutions of spread factors for all three materials with different impact velocities in the spreading regime. It is obvious that there is no uniform expression could be presented here for all the cases, which is different from the situation in the kinetic regime. This is because other parameters, such as viscosity and surface tension, are also involved in the spreading process; therefore, the evolution of spreading diameter does not simply depend on time or initial velocity. It is observed that for each liquid, with increasing impact velocity, drop spreads faster and the maximum spread factor $\beta_{\max}$ is larger. Moreover, for different liquids, with decreased Oh number, drop spreads faster, resulting in larger $\beta_{\max}$.

Non-dimensional numbers, such as Re, We, Ca and Oh, are often used to characterize the drop behaviors as mentioned in Chapter 1. The value of maximum spread factor $\beta_{\max}$ for each case is plotted in terms of Re and We, as shown in Figure 3-12 and 3-13. It is noted that $\beta_{\max}$ shows a nonlinear and non-monotonic behavior with Weber number and Reynolds number. Since Reynolds number represents the ratio of inertial to viscous effect ($\mathrm{Re} = \rho Du/\mu$) while Weber number is the ratio of inertial to surface tension ($We = \rho Du^2/\sigma$), the nonlinear trends of $\beta_{\max}$ indicate that the behavior of the spread factor during the spreading regime is not purely based on viscosity nor surface tension. Nonetheless, as shown in Figure 3-11, $\beta_{\max}$ increases with decreased Oh (which relates the viscous and the surface tension forces, $Oh = \sqrt{We}/\mathrm{Re} = \mu/\sqrt{\rho\sigma D}$). Such a

linear relationship indicates that the behavior of the spread factor during the spreading regime is actually affected by the combination of surface tension and viscosity. Moreover, this concept could also be confirmed by the physics during this regime, where kinetic energy is transferred in to additional surface tension energy and dissipated by the viscous effect. Therefore, the Ohnesorge number is applicable to describe the spreading regime.

It is noted that Capillary number ($Ca = V\mu / \sigma$) is also a combination of viscous effect and surface tension, which has already widely used in previous studies (Cox, 1986; Jiang, et al., 1978; Kistler, 1993) to describe drop behaviors during the spreading regime. As mentioned in Chapter 1, the reason why we choose Oh number instead of Ca is based on the concern of computational cost. Since spreading velocity V in Ca needs to be updated after each time step, resulting in high computational cost, Oh number (which is purely based on liquid properties) becomes our choice.

3.2.3 Experimental Exponential Correlation

Since Regime II coincides and shows the exact same trend for diesel and methanol with various impact velocities, two similar exponential curves could be used to fit the decreasing trend.

For the diesel drop:

$$\theta_d^* = \exp(4.72 - 0.51t^{**} + 0.03t^{**2}) \tag{15}$$

For the methanol drop:

$$\theta_d^* = \exp(3.78 - 0.24t^{**} + 0.01t^{**2}) \tag{16}$$

where t^{**} is the modified non-dimensional time, $t^{**} = tu / D - t^*$.

Similarly, we derived an exponential expression to express the Regime II for glycerin drops based on Sikalo et al.'s experimental data (Šikalo, et al., 2005). The form is

$$\theta_d^* = \exp(4.96 + 0.21t^{**} - 0.14t^{**2}) \quad (17)$$

Since the values of θ_d^* are increasing in Regime II for the glycerin drops rather than decreasing for the diesel and methanol drops, the signs in Eq. (17) are opposite to the ones in Eq. (15) and (16). All the fitted exponential relations were plotted in Figures 3-8 and 3-9 as the black solid lines. To reduce the requirement of experimental data, a general expression for all different materials is preferred here. As discussed in Chapter 3.2.2, the Oh number can be used to describe the physics occurs in Regime II, a general expression is derived in terms of the Oh number in the following form,

$$\theta_d^* \approx \exp[5.70 \times Oh^{0.05} + (-1)^n \times 0.83 \times Oh^{-0.01} t^{**} + (-1)^{n+1} \times 0.31 \times Oh^{0.56} t^{**2}] \quad (18)$$

where $n = 1$ when $Oh < 0.1$, and $n = 0$ when $Oh \geq 0.1$.

With such a general equation, the drop spreading in Regime II could be described. This equation is substituted into the simulation as the boundary condition. Note that this contact angle boundary condition determines the curvature of the free surface at the contact line via Eq. (27).

Table 3-1 Properties of the Hydrocarbon Liquid

Liquid	σ (mN/m)	μ (mPa s)	$\rho(kg/m^3)$
Diesel	28.0	3.6	880
Methanol	22.7	0.6	792
Glycerin*	63.0	116	1220

*Source: Šikalo, Š., et al., *Dynamics contact angle of spreading droplets: Experiments and simulations.* Physics of Fluids 2005. **17**(062013): p. 1-13.

Table 3-2 List of Experiments for Hydrocarbon Drops

Experiment	Liquid	Impact velocity (m/s)	*D (mm)*	*Oh*	*We*	*Re*
1	Diesel	1.60	2.2063	0.0154	177	863
2	Diesel	1.21	2.1746	0.0155	100	643
3	Diesel	0.76	2.1746	0.0155	40	404
4	Methanol	2.33	2.65	0.0027	502	8150
5	Methanol	2.75	2.62	0.0027	691	9511
6	Methanol	3.05	2.62	0.0027	850	10548
7	Glycerin*	1.04	2.45	0.2673	51	27
8	Glycerin*	1.41	2.45	0.2673	94	36
9	Glycerin*	4.1	2.45	0.2673	798	106

*Source: Šikalo, Š., et al., *Dynamics contact angle of spreading droplets: Experiments and simulations.* Physics of Fluids 2005. **17**(062013): p. 1-13.

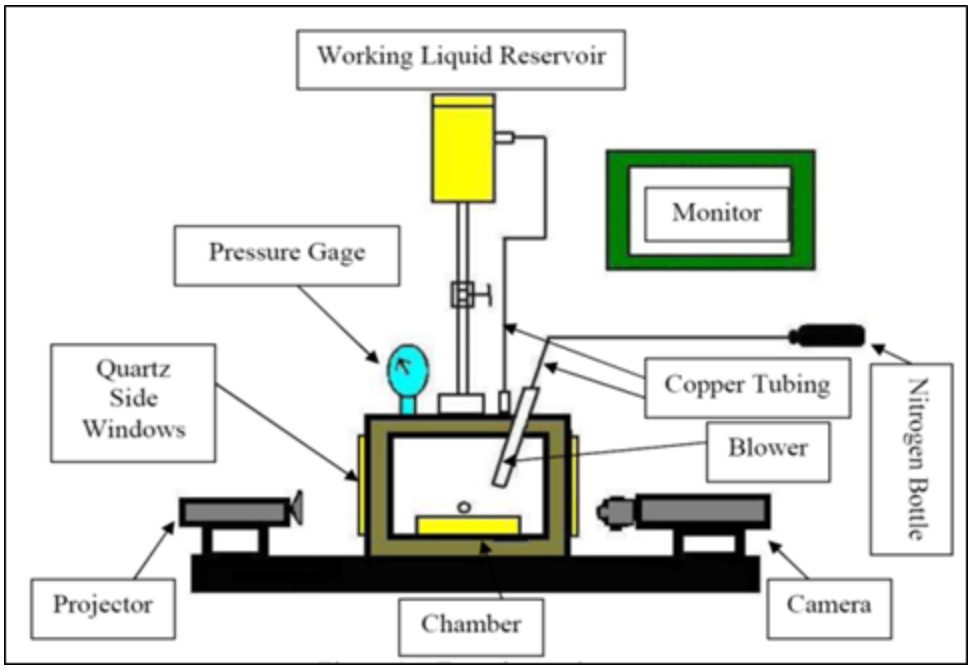

Figure 3-1 The experimental arrangement

Source: Mishra, N.K., Y. Zhang, and A. Ratner, Effect of chamber pressure on spreading and splashing of liquid drops upon impact on a dry smooth stationary surface. Experiments Fluids, 2011. **51**(2): p. 483-491.

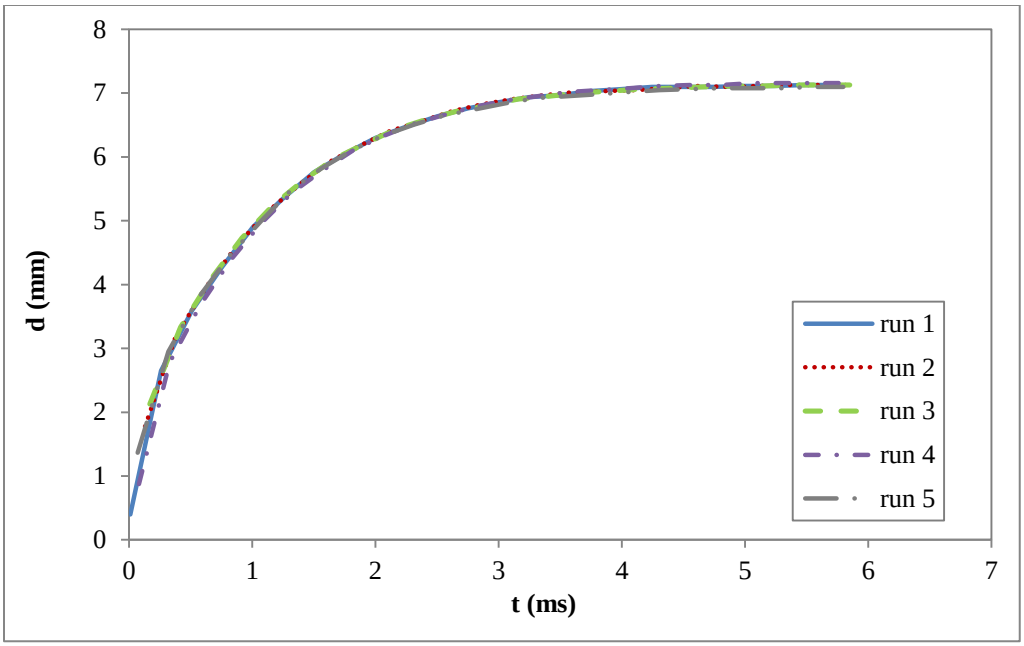

Figure 3-2 Repetitions of a diesel drop impact on the glass with initial speed u = 1.6 m/s

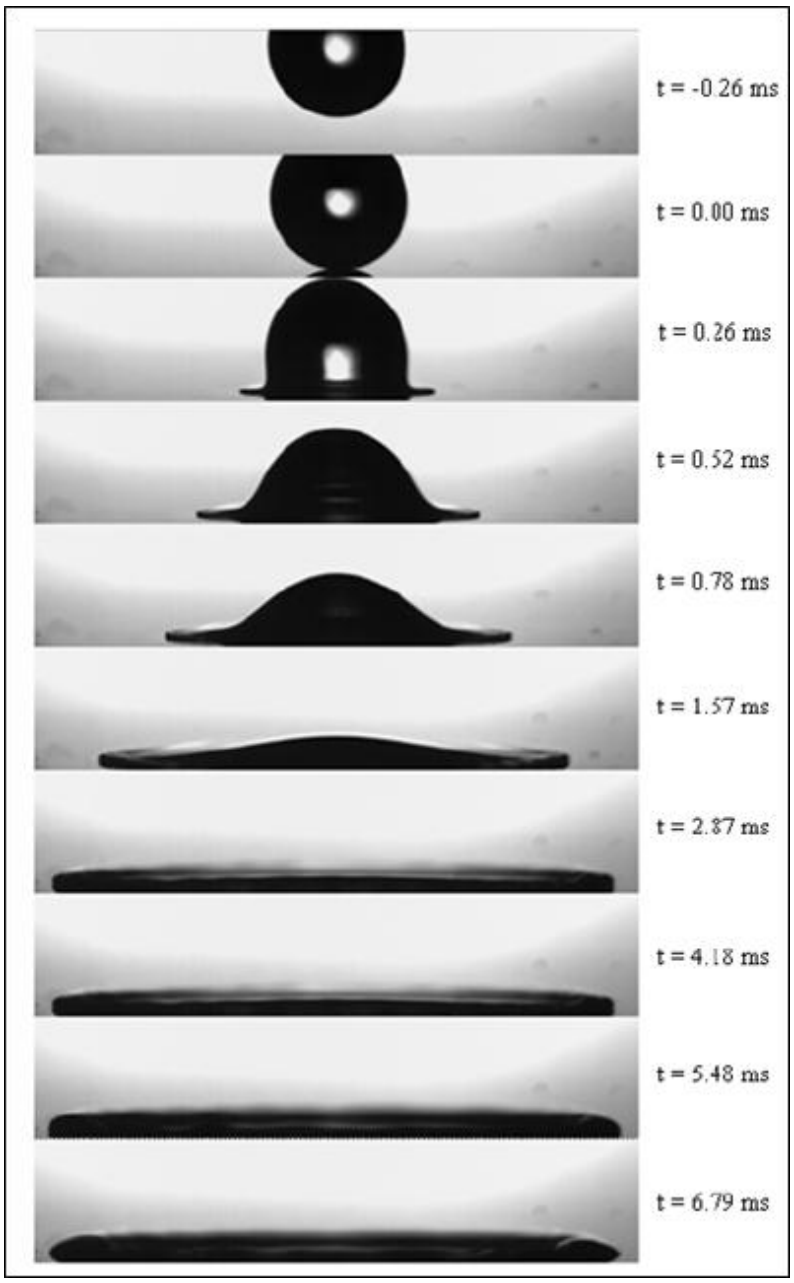

Figure 3-3 A diesel drop impacts on the glass with initial speed u = 1.6 m/s

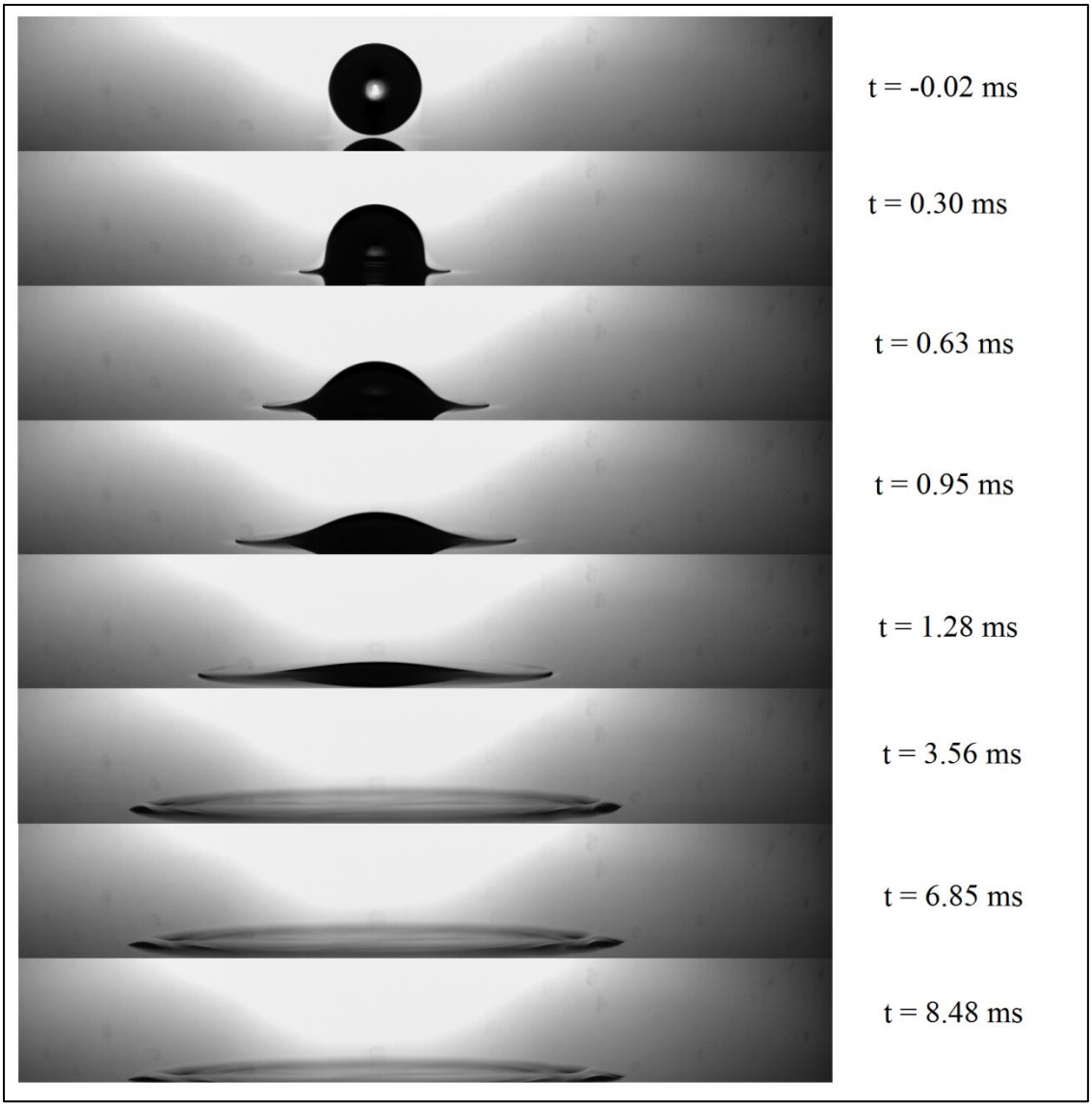

Figure 3-4 A methanol drop impacts on the glass with initial speed u = 2.33 m/s

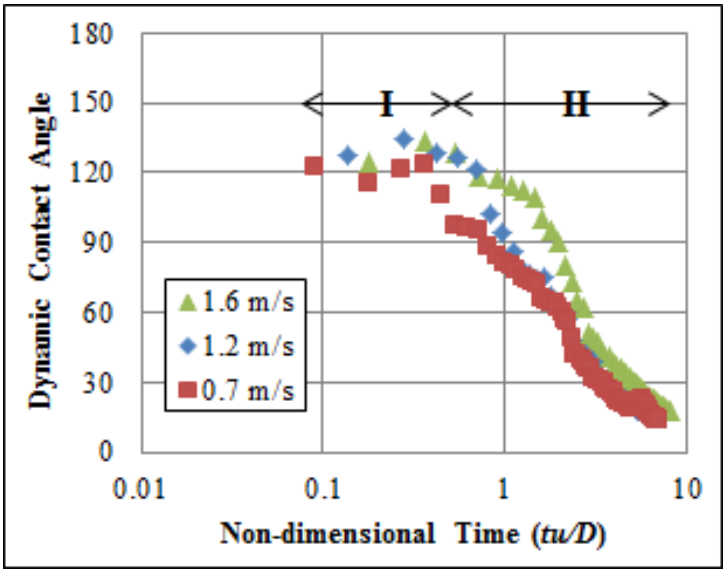

(a)

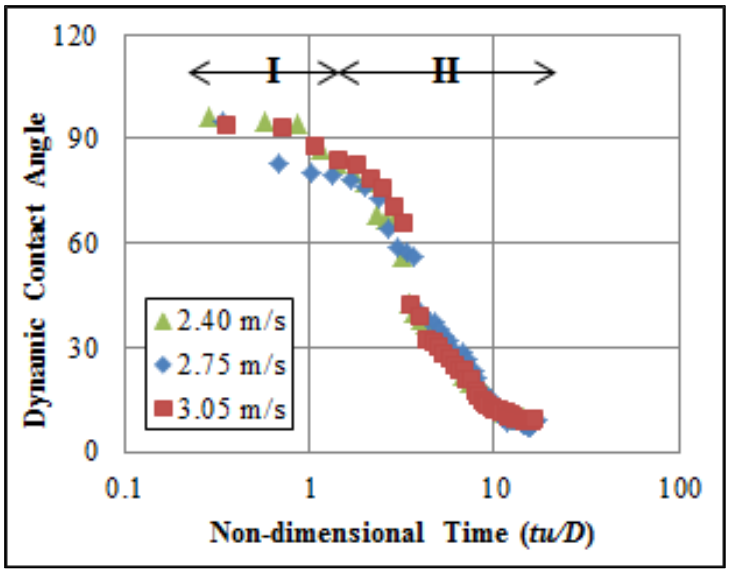

(b)

Figure 3-5 Experimental values of apparent dynamic contact angles for fuel drops impacting at three different impact speeds: (a) diesel drops; (b) methanol drops

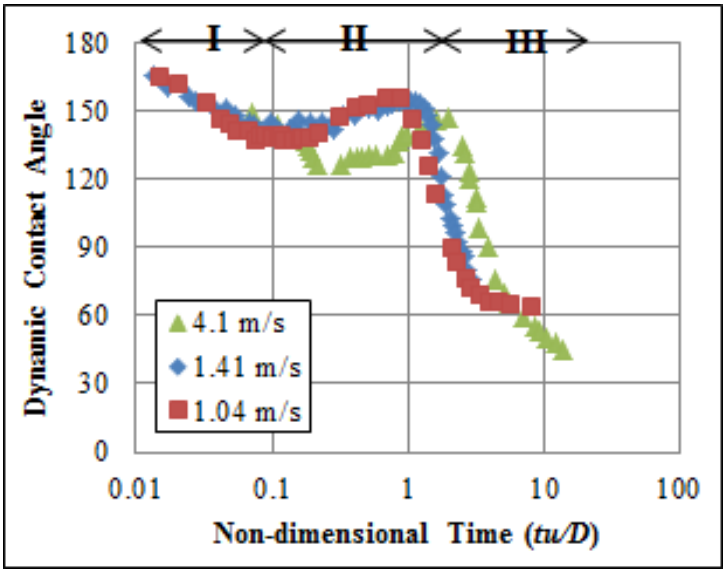

Figure 3-6 Experimental values of apparent dynamic contact angles for glycerin drops impacting at three different impact speeds

---

Source: Šikalo, Š., et al., *Dynamics contact angle of spreading droplets: Experiments and simulations.* Physics of Fluids 2005. **17**(062013): p. 1-13.

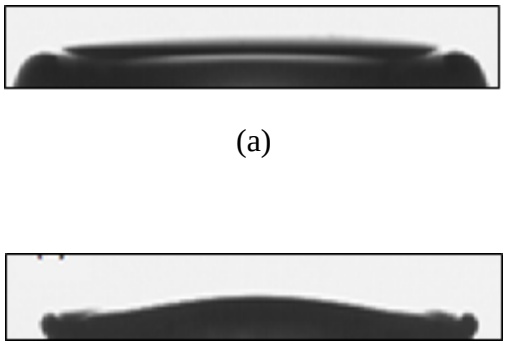

(a)

(b)

Figure 3-7 (a) a diesel drop at Regime II: lower surface tension leads to the relaxation of the lamella; (b) a glycerin drop at Regime II: higher surface tension leads to the accumulation of the lamella.

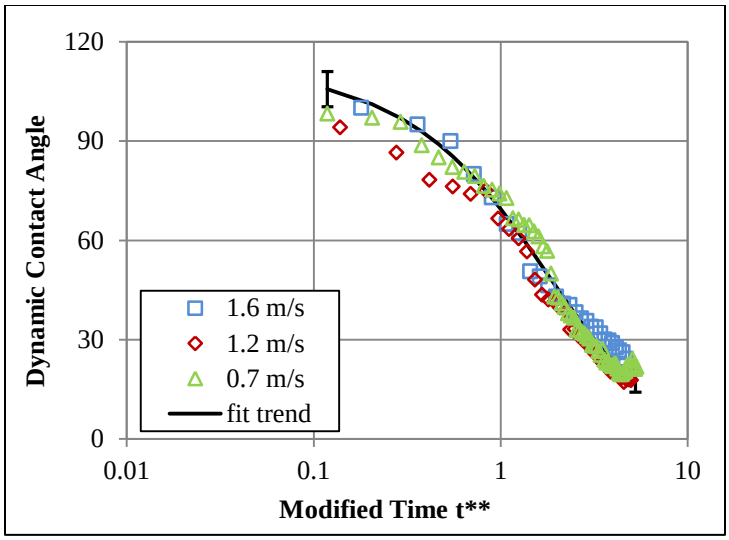

(a)

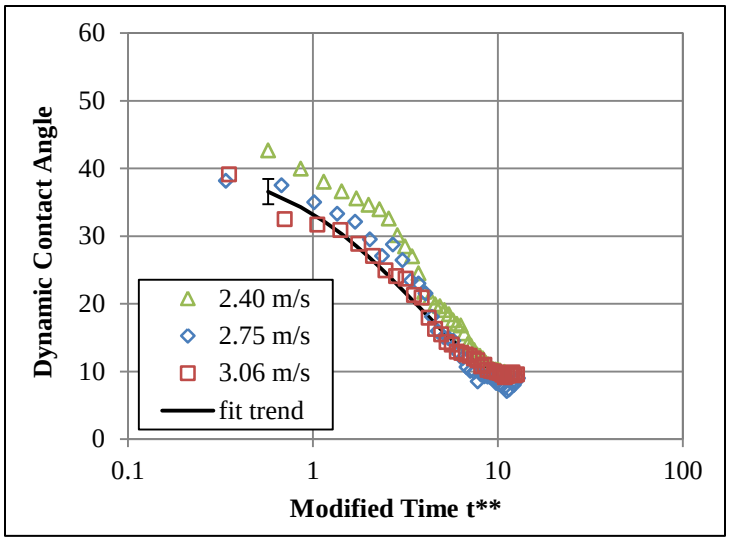

(b)

Figure 3-8 Coincided Regime II of apparent dynamic contact angles for (a) diesel drops and (b) methanol drops. The fit trends were calculated by using Eq. 18, and standard deviation error bars with 5% were plotted at the initial and final time instances separately.

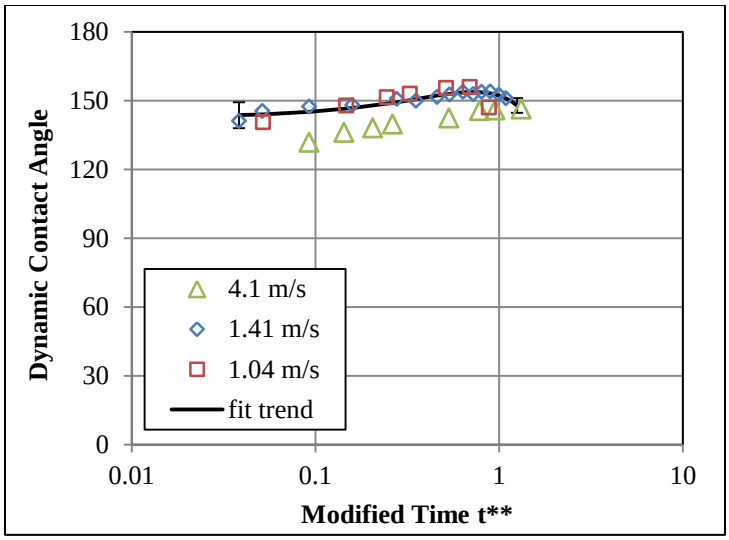

Figure 3-9 Coincided Regime II of apparent dynamic contact angles for glycerin drops. The fit trends were calculated by using Eq. 18, and standard deviation error bars with 5% were plotted at the initial and final time instances separately.

Source: Šikalo, Š., et al., *Dynamics contact angle of spreading droplets: Experiments and simulations.* Physics of Fluids 2005. **17**(062013): p. 1-13.

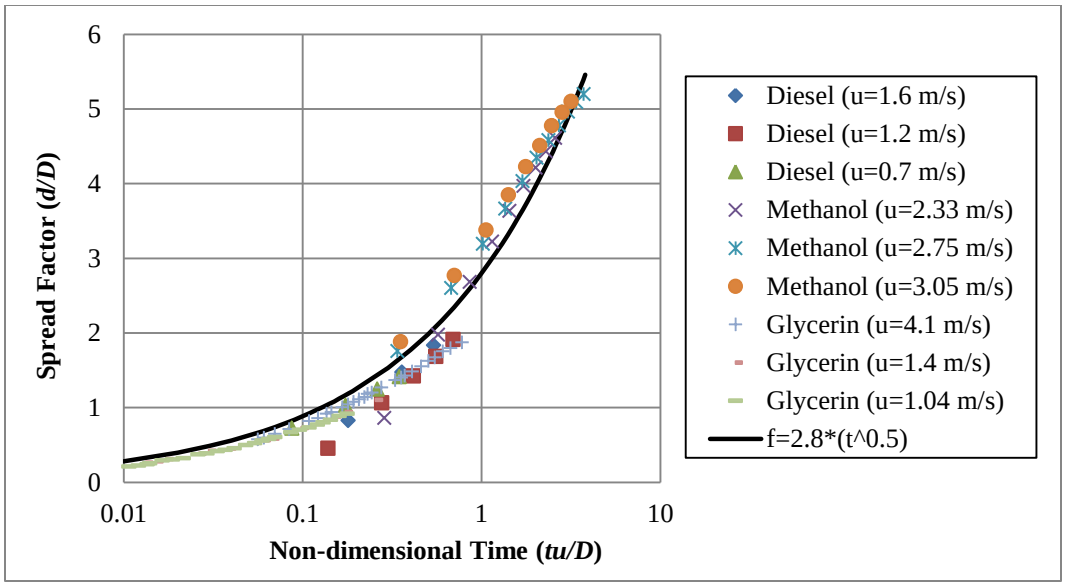

Figure 3-10 Spread factors of various cases in the kinetic regime compared with the power law

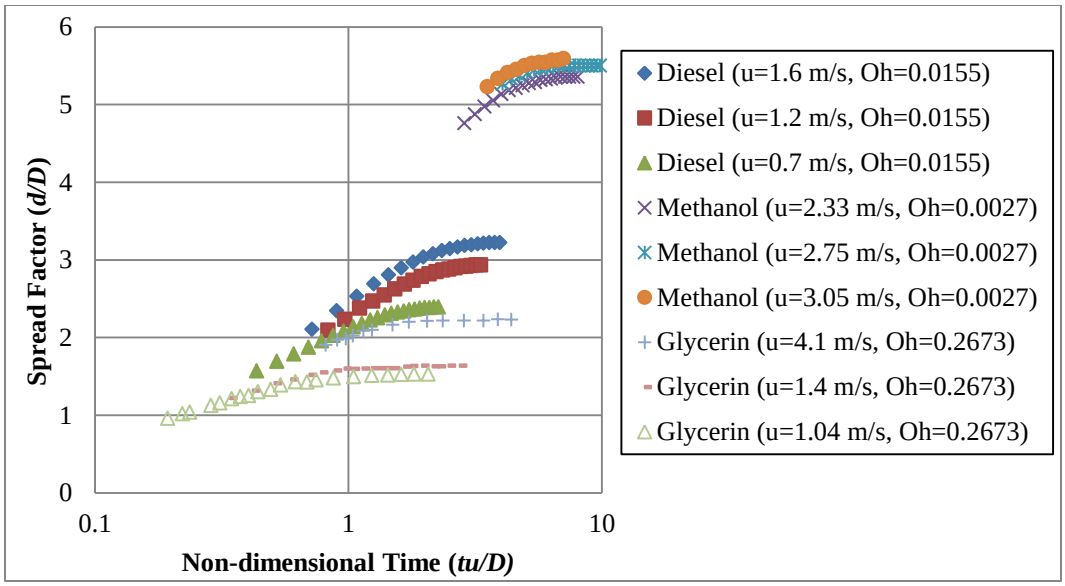

Figure 3-11 Spread factors of various cases in the spreading regime

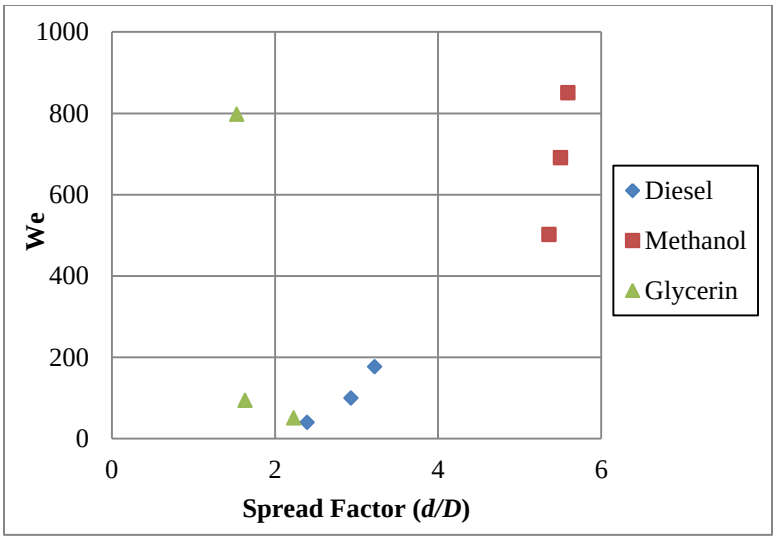

Figure 3-12 Final spread factor of each case in terms of Weber number

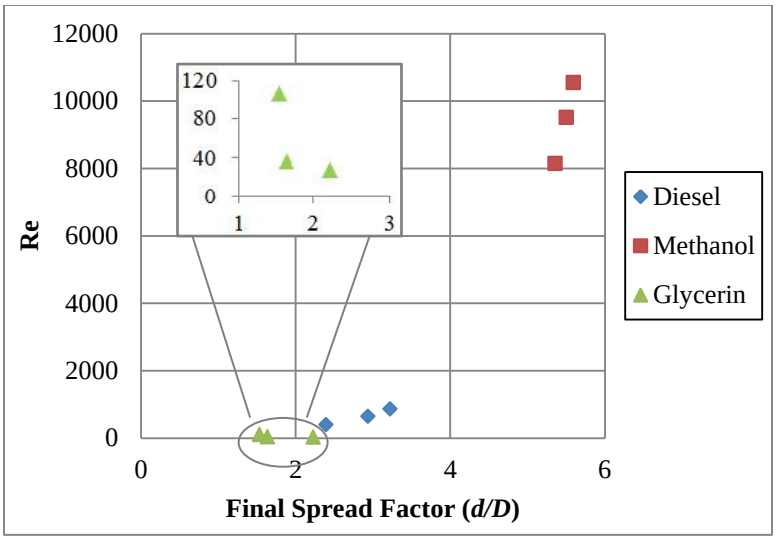

Figure 3-13 Final Spread factor of each case in terms of Reynolds number

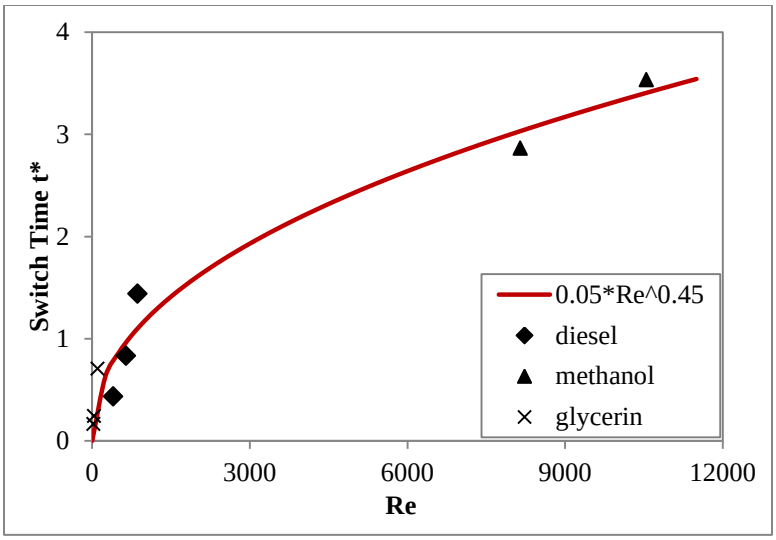

Figure 3-14 Transition time in terms of Reynolds number for each drop: The red line is a power fit to the experimental data.

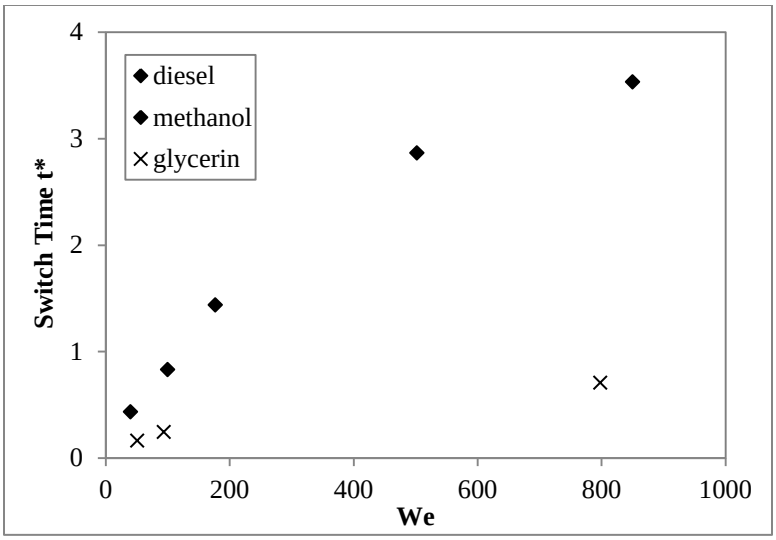

Figure 3-15 Transition time in terms of Weber number for each drop.

CHAPTER 4: COMPUTATIONAL METHOD

4.1 Computational Method

Two different phases are defined in the VOF method, where gas is normally defined as the primary phase whereas liquid is the secondary phase. Each control volume only contains one phase (or the interface between phases). The mass and momentum conservation equation for each phase:

$$\frac{\partial(\rho u_i)}{\partial x_i} = 0 \tag{19}$$

$$\frac{\partial(\rho u_i)}{\partial t} + \frac{\partial}{\partial x_j}(\rho u_i u_j) = -\frac{\partial p}{\partial x_i} + \frac{\partial}{\partial x_j}\mu(\frac{\partial u_i}{\partial x_j} + \frac{\partial u_j}{\partial x_i}) + \rho g_i + F_i \tag{20}$$

where u is the velocity, p is the pressure, and F is the surface tension force per unit volume. The density of the mixture is calculated as:

$$\rho = \sum \alpha_k \rho_k \tag{21}$$

Any other mixture property, ϕ, is calculated as

$$\phi = \frac{\sum \alpha_k \rho_k \phi_k}{\sum \alpha_k \rho_k} \tag{22}$$

where ρ_k is the density of k^{th} fluid, ϕ_k is the corresponding property of k^{th} fluid, and α_k is the volume fraction of the k^{th} fluid:

$$\alpha_k(cell) = \frac{\iiint_{cell} \alpha_k(x,y,z)dxdydz}{\iiint_{cell} dxdydz} \tag{23}$$

When in a specified control volume, three conditions are possible:

$\alpha_k = 0$: if the cell is empty (of the k^{th} fluid)

$\alpha_k = 1$: if the cell is full (of the k^{th} fluid)

$0 < \alpha_k < 1$: if the cell contains the interface between the fluids

Tracking of interface(s) between phases is accomplished by solution of a volume fraction continuity equation for each phase:

$$\frac{\partial \alpha_k}{\partial t} + u_i \frac{\partial \alpha_k}{\partial x_i} = S_{\alpha_k} \tag{24}$$

Mass transfer between phases can be modeled by using a user-defined subroutine to specify a nonzero value for S_{α_k}. In the present work, since the mass transfer between two phases is zero, S_{α_k} is set to be zero. The volume fraction for the primary phase is obtained directly from the following equation:

$$\sum_k \alpha_k = 1 \tag{25}$$

Continuum Surface Force (CSF) is the most widely used model to evaluate surface tension, proposed by Brackbill et al. (Brackbill et al., 1992). In this model, surface tension is reformulated into an equivalent volume force and results in a source term in the momentum equation.

$$\boldsymbol{F}_{ST} = \frac{\sigma \kappa \boldsymbol{n} (\alpha_1 \rho_1 + \alpha_2 \rho_2)}{\frac{1}{2}(\rho_1 + \rho_2)} \tag{26}$$

where κ is the curvature, defined in terms of the divergence of the unit normal, $\hat{\boldsymbol{n}}$:

$$\kappa = \nabla \bullet \hat{\boldsymbol{n}} \tag{27}$$

$$\hat{\boldsymbol{n}} = \frac{\boldsymbol{n}}{|\boldsymbol{n}|} \tag{28}$$

and $\boldsymbol{n}$ is the surface normal, defined as the gradient of α_2:

$$\boldsymbol{n} = \nabla \alpha_2 \tag{29}$$

4.2 Numerical Grids

Three different numerical grids are employed in this work: a three-dimensional (3D) whole domain for the diesel drops, a 3D domain quarter domain for the methanol drops, and a 2D domain for the glycerin drops. The reason why we adopted three various kinds of domains are explained as follows.

Note that a three-dimensional (3D) simulation of drop spreading on a flat surface could be considered as axisymmetric with the exception of small capillary waves. In that case, drop spreading could be simulated in a 1/4 domain with two symmetric surfaces. The main advantage of applying a 1/4 domain is that computational cost could be significantly decreased, compared with the application of a whole domain. However, it is observed that 3D quarter domain shows less accuracy than a whole domain. Figure 4-1 shows an example of simulating a diesel drop in a 1/4 domain and a whole domain separately. It is so obvious that values of spread factor β predicted in a whole domain are more accurate than the one in a 1/4 domain. This is because the symmetric boundaries in the quarter drop domain restrict the intrinsic instability of drops, inducing an over-predicted spreading velocity (Y. Zhang & Ratner, 2010). Eq. (30) shows an energy balance relation during the drop spreading process:

$$E_k = E_k^{'} + E_{dif} + E_\sigma \tag{30}$$

where E_k indicates the original kinetic energy, $E_k^{'}$ is the remaining kinetic energy, E_{dif} is the dissipated energy by viscous effect, and E_σ is the surface tension energy. As noted by Eq. (30), after drop impacts the solid surface, part of the original kinetic energy E_k is dissipated by the viscous effect while some other part is transferred into additional surface tension energy. Because of the intrinsic instability and interactions with surrounding fluid (air), oscillations occur during the drop spreading process. These oscillations could be decomposed into axisymmetric modes ($I = 1, 4, 8...$) and non-axisymmetric modes ($I = 2, 3, 5, 6, 7...$), as shown in Figure 4-2 (Shen et al., 2010).

However, only axisymmetric modes are allowed for the quarter domain. In that case, the non-axisymmetric oscillations are dismissed and therefore the surface tension energy E_σ is reduced. Thus, the remaining kinetic energy $E_k^{'}$ is increased and drop spreads faster than reality. However, these non-axisymmetric oscillations are hardly found from the drop shapes (both in photographs and predicted results). Figure 4-3 shows the top views of computer generated drop shapes in two separate domains at the same time instance (t = 3.224 ms), and two fitting circles are drawn in corresponding radius. It is noted that the deviation from the asymptotic circle in the 1/4 domain is larger than the one in the full domain, $\Delta r_{1/4} > \Delta r_{full}$. This is because the restrictions of the symmetric boundary conditions in the 1/4 domain is so powerful that "squeeze" the drop in the diagonal direction.

Due to the limitation of the quarter domain, a 3D whole domain is preferred to predict the drop impact and spreading process. A solution domain representing a $12 \times 12 \times 5$ mm large block in *x*-*y*-*z* Cartesian coordinate system is created for the diesel drops, according to the maximum spreading diameter for the diesel drops (around 8 mm). A structured grid with refinement close to the wall is used to discretize the domain. The initial radius for the diesel drop is around 1 mm and the spreading lamella is in the order of 0.2 mm. To capture the spreading of the lamella, at least 3-5 cells are needed in the vertical direction of the lamella. Thus, the minimum thickness of the cell employed is around 20 microns.

Even though the whole domain presents higher accuracy, a mesh region was created as a quarter of the whole domain for methanol drops. It is because the final diameter of the methanol drop is up to 14 mm and the thickness of lamellar ends up to only 0.06 mm. With such a larger and thinner rim, the mesh size in the methanol cases should be decreased compared with the one of the diesel drops, making sure that there are around 3 - 5 meshes in the vertical direction of the lamella. However, with decreased mesh size (required by thickness of the rim) and increased domain size (required by the

diameter of the rim), the number of meshes in the whole domain is also significantly increased, resulting in a noticeable augment of computational cost from 1-2 days (quarter domain) to 7-10 days (whole domain). Therefore, due to the limitation of computational cost, the numerical domain for methanol drops was cut into a quarter one, with the size of $10 \times 10 \times 5$ mm in x-y-z direction with two planes of symmetry (indicating the total mesh size is $20 \times 20 \times 5$ mm) as shown in Figure 4-4. Moreover, because of the application of quarter domain, the predicted methanol drop shapes are less accurate than the other two liquids, which will be shown in details in Chapter 5.

To test our model for glycerin drops and compare the predicted results with Sikalo et al.'s, the same simulation region was employed in this work. A two-dimensional (2D) domain is created with the size of 100×100 mm in r-z plane and the smallest cell is around 19.5 microns. The full details of this 2D domain are available in (Šikalo, et al., 2005). It is noted that a 2D axisymmetric domain is applicable and shows great accuracy for glycerin drops (as shown in Chapter 5). Since surface tension of glycerin is much higher than methanol and diesel, fewer oscillations occur during the drop spreading process. Therefore, in the axisymmetric domain, the loss of surface tension energy resulted from the dismissing of non-axisymmetric oscillations could be negligible for glycerin drops.

4.3 Numerical Solution and Boundary Condition

A whole drop is patched in the solution domain with exactly the same diameter and initial velocity as the experimental picture shows (Figure 4-4). The bottom of the solution domain is defined as the wall while the top surface is set as pressure-outlet and the side ones are pressure-inlets. No-slip boundary condition is specified at the wall where all the components of velocity are set to be zero. Three different models of contact angles are tested in this work: the SCA model, the combine SCA-DCA model, Kistler's

correlation (Kistler, 1993). The QUICK scheme is implemented for the mass and momentum equations and the first-order implicit method is used to discretize the time derivatives. In the momentum equation, pressure and velocity is coupled by the pressure implicit with splitting of operator (PISO) scheme. The applied time step is varying corresponding to the time interval between successive frames of experimental images taken at different camera speeds, ranging from 0.003 ms to 0.0326 ms.

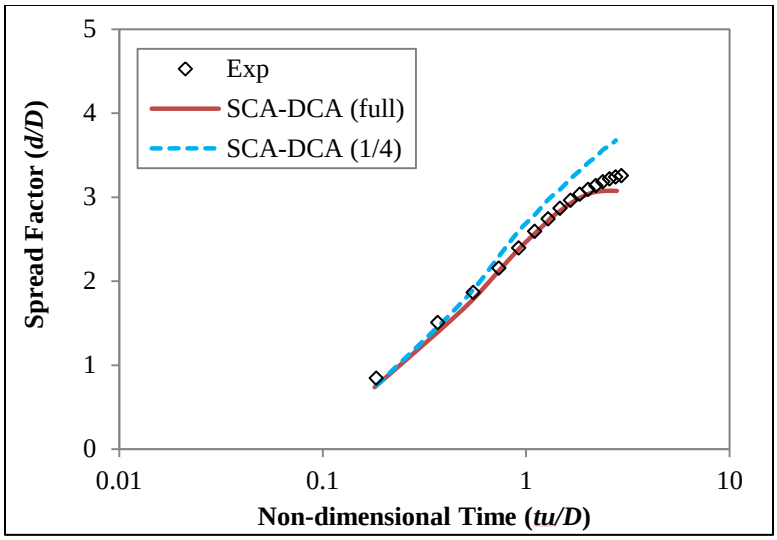

Figure 4-1 Comparison of the experimental and numerical spread factors in the whole domain and quarter domain with the SCA-DCA model for a diesel drop impacting with speed u = 1.6 m/s.

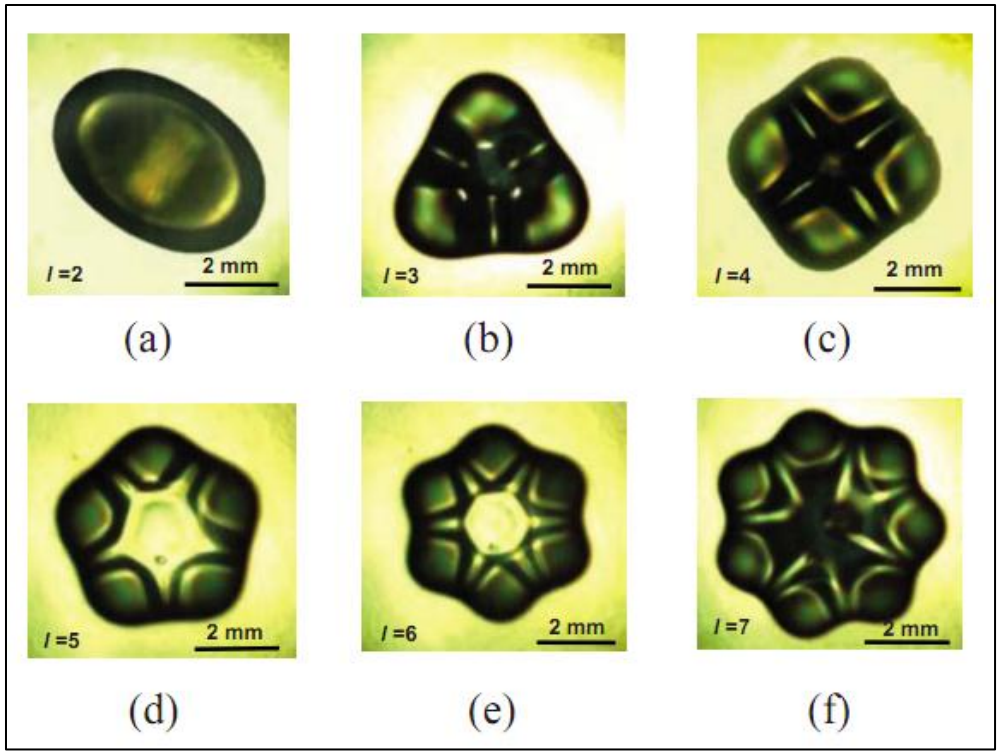

Figure 4-2 Typical patterns of water drop under different oscillation modes.

Source: Shen, C. L., Xie, W. J., & Wei, B. (2010). Parametrically excited sectorial oscillation of liquid drops floating in ultrasound. *Phys. Rev. E.*, *81*(046305), 1-6.

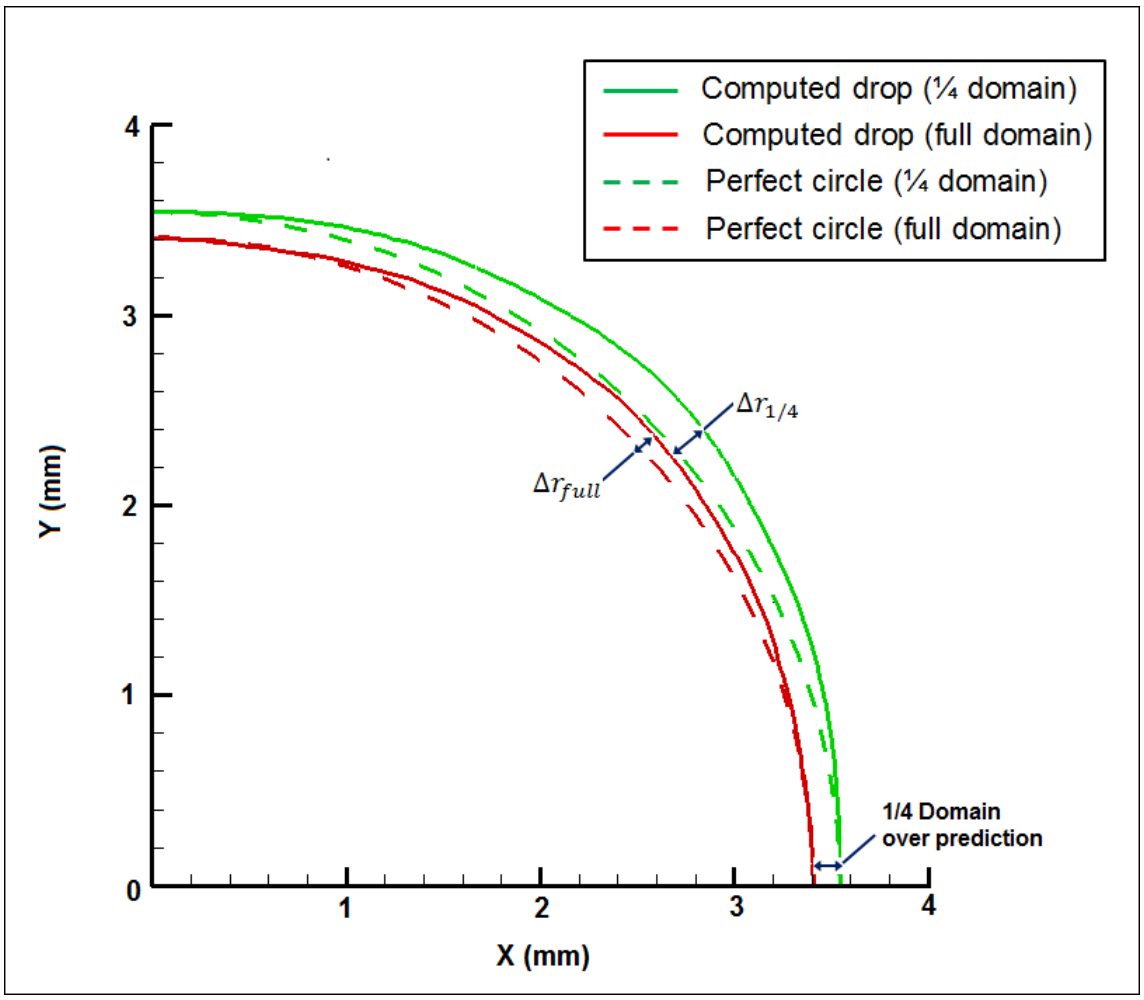

Figure 4-3 Top views of computer generated images of a diesel drop impacting on the surface with u = 1.6 m/s at time t = 3.224 ms in a quarter domain (red solid) and a full domain (green solid). The dashed lines are the fitting circles with corresponding radius.

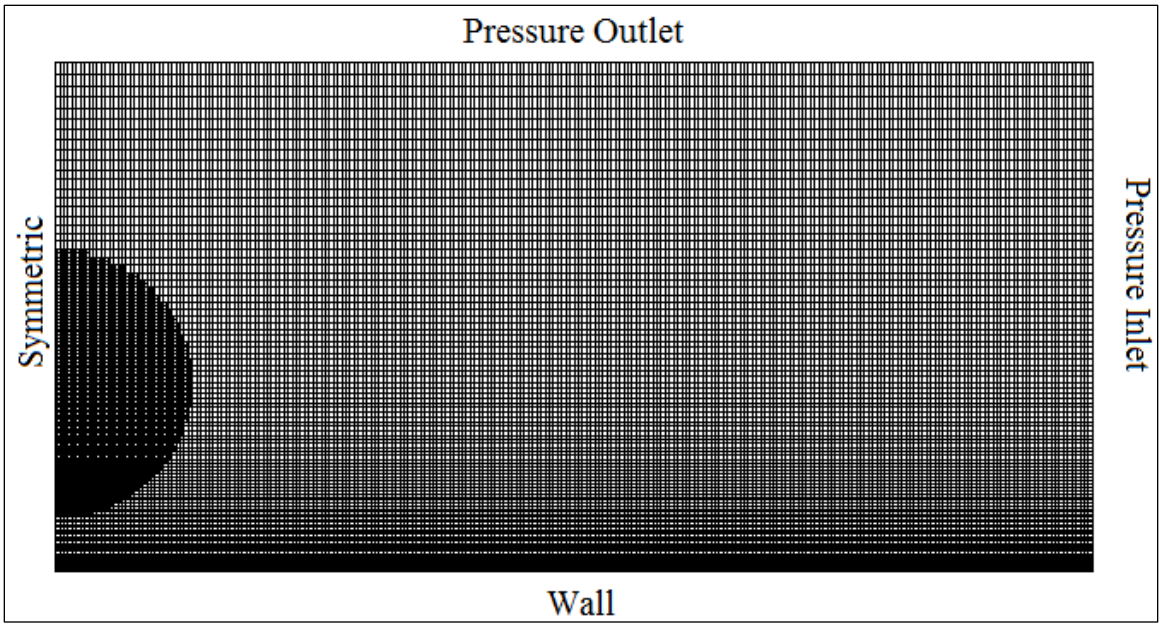

Figure 4-4 A side view of the solution domain (the x-z plane at z = 0) and boundary conditions for the methanol drops: meshes were refined towards the wall

CHAPTER 5: NUMERICAL RESULTS AND DISCUSSION

5.1 Drop Impact with the SCA Model

A criterion used in this work to compare the experimental and numerical results is a quantifiable comparison of the spread diameter at each time step after drop impacting on the surface.

The static contact angle model is tested as the baseline in this work. This model has been widely studied and been used in the previous studies (Gunjal, et al., 2005; Lunkad, et al., 2007; Pasandideh-Fard, et al., 1996; Šikalo, et al., 2005). In this model, the static contact angle is substituted into the numerical simulation as the boundary condition, assuming that the contact angle is equal to the static contact angle throughout the spreading process, $\theta_d = \theta_e$. The previous studies have shown that the SCA model lacks of accuracy. Again, in this work, by comparing the simulation results of the SCA model with our diesel data, the decrement of the SCA model is shown in Figures 5-1. In the case of the diesel drop with impact speed u = 1.6 m/s (Fig. 5-1a), when the dimensionless time tu/D < 0.7, it is evident that the drop spreading is nearly identical for both the SCA model and the experimental results. However, an appreciable change of the shape starts from tu/D = 0.7 onwards. At the end of drop spreading, the error of the SCA model is about 16%. By comparing with the evolution of contact angles, it could be observed that tu/D = 0.7 is the characteristic time when the kinetic regime ends. In other words, the SCA model shows good accuracy in the kinetic regime and fails in the spreading regime. This situation is also clear in the cases with impact speed u = 1.2 m/s (Fig. 5-1b) and u = 0.7 m/s (Fig. 5-1c). Hence, this indicates that the SCA model is sufficient to accurately predict the first regime while another model is needed to predict the second regime.

5.2 Drop Impact with the Combined SCA-DCA Model

Since a general expression of the apparent dynamic contact angle has been derived from the experimental data (Eq. 29), this expression is employed as the boundary condition in the spreading regime. Therefore, the SCA model is employed in the 1st regime while the variable contact angle model with the general expression (Eq. 29) is applied as the boundary condition in the 2nd regime. This specific model is proposed as the "combined SCA-DCA model". This model was tested for all three materials with different impact speeds. Figure 5-2 shows images of drop deformation obtained from the SCA-DCA model, along with photographs of a diesel drop impacting the surface with u = 1.6 m/s. Predicted spreading diameters were measured from each computed image and compared with the experimental data at the same time (*t*) after impact. Note, the wrinkle in the leading edge of the lamella in experimental pictures (e.g. when t=0.992 ms) is not the result of oscillation but it is the reflection of the other drop side. This is because the camera was not placed perfectly normal to the direction of incidence.

Figures 5-3 to 5-5 show the comparisons of this model with the experimental data: glycerin drops are shown in Figure 5-3, diesel drops are displayed in Figure 5-3, and methanol drops are plotted in Figure 5-5. Table 5-2 shows the errors of predicted spread factors by using SCA-DCA model compared with the experimental data for all the cases. It is clear that the numerical results in most cases have sufficient accuracy within the quality of experiment results, since the all experimental uncertainties are reported at 95% level of confidence. Note that the numerical results of the methanol drops are less accurate than the other two liquids. This is because the quarter domain applied for methanol drops restricts the intrinsic instability, offering a less accurate prediction, as discussed in Chapter 4.

In addition to the above comparisons, we also compare the simulation results of Sikalo et al. (Šikalo, et al., 2005) with ours. Here, Sikalo et al. only presented their simulation result of the case with u = 1.41 m/s. As shown in Figure 5-3c, our SCA-DCA

model shows better accuracy than Sikalo et al.'s who used Kistler's correlation (Eq. 12). In addition, Kistler's equation (Eq. 12) (Kistler, 1993) is also coded as the boundary condition calculating the dynamic contact angle in the diesel and methanol cases (as shown in Figures 5-6 and 5-7). This model shows reasonable accuracy in the first regime but predicts smaller drop shape as time evolves.

A key benefit of the SCA-DCA model is that it is generated only with the value of static contact angle and a general empirical equation. Hence, in this model, only the values of θ_e and Oh number are needed, both of which are purely based on the properties of the liquid. The requirement of having detailed data (often 50 to 100 points) of the time-varying contact angle that is typically employed in a full DCA model (Gunjal, et al., 2005; Lunkad, et al., 2007; Pasandideh-Fard, et al., 2002; Pasandideh-Fard, et al., 1996) is also avoided. Thus, this model is shown to reduce the experimentally-derived behavior information required as compared with full DCA models. The second advantage of the SCA-DCA model is that it significantly improves the accuracy over a pure SCA model and other empirical correlations, especially in the spreading regime. Moreover, by employing Oh number instead of Ca number, computational cost is also greatly decreased by using the new model. This is because Oh is only related to the properties of drops, whereas spreading velocity V in Ca number needs to be updated after each time step, remarkably increasing the computational cost.

Note, however, the SCA-DCA model has only been tested for three hydrocarbon liquids exhibiting a two-regime spreading behavior. According to the definition of this new model, it is only valid for the two-regime drop impacting process (a kinetic regime followed with a spreading regime).

5.3 Mass Conservation of VOF method

One primal advantage of using VOF method is that it guarantees the mass conservation through numerical computations. Rather than some other method, where mass needs to update every time step making sure it is constant, mass conservation is not of concern to the VOF simulations. To check this consistency, mass of each drop was computed and compared at the initial and final time step separately. It is observed the mass differences of diesel and glycerin drops throughout simulations are less than 0.4%, whereas the ones of methanol drops are within 5%. Hence, VOF method has successfully guaranteed the mass conservation.

Table 5-1 Simulation Errors of the SCA-DCA Model

Simulation	Liquid	Impact velocity (m/s)	Error
1	Diesel	1.60	4%
2	Diesel	1.21	3.8%
3	Diesel	0.76	0.9%
4	Methanol	2.33	5.2%
5	Methanol	3.05	7.5%
6	Glycerin	1.04	2.5%
7	Glycerin	1.41	1.4%
8	Glycerin	4.1	3.4%

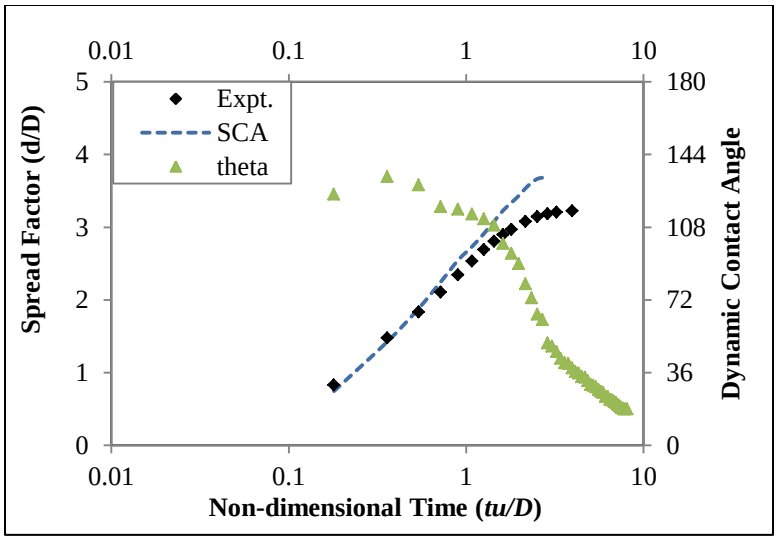

(a)

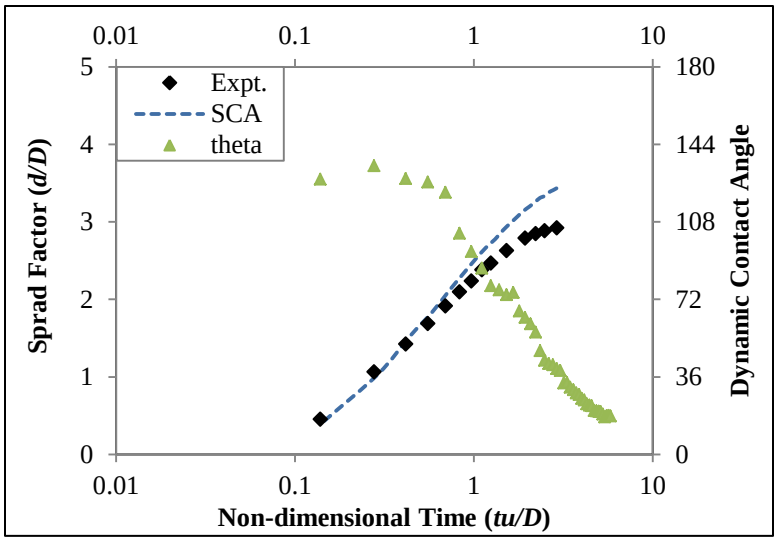

(b)

Figure 5-1 Experimental apparent dynamic contact angles and comparisons of the experimental and numerical spread factors with the SCA model of the diesel drop with impact speed (a) u = 1.6 m/s, (b) u = 1.2 m/s, and (c) u = 0.7 m/s.

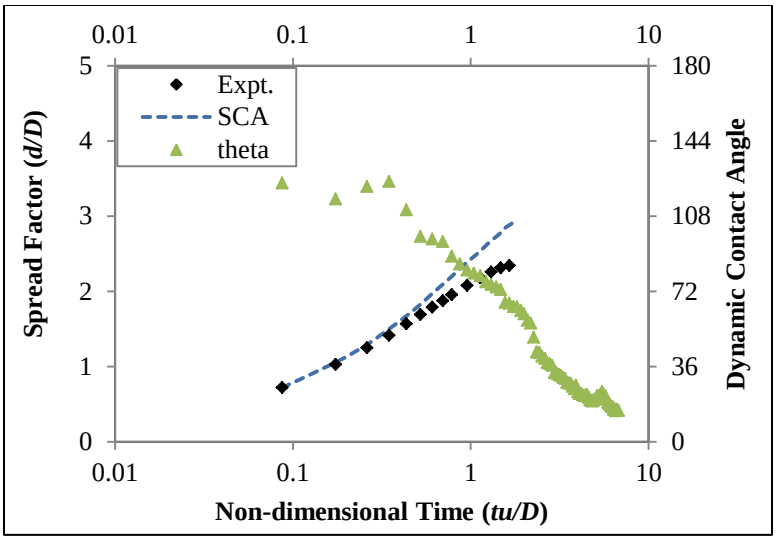

(c)

Figure 5-1--continued

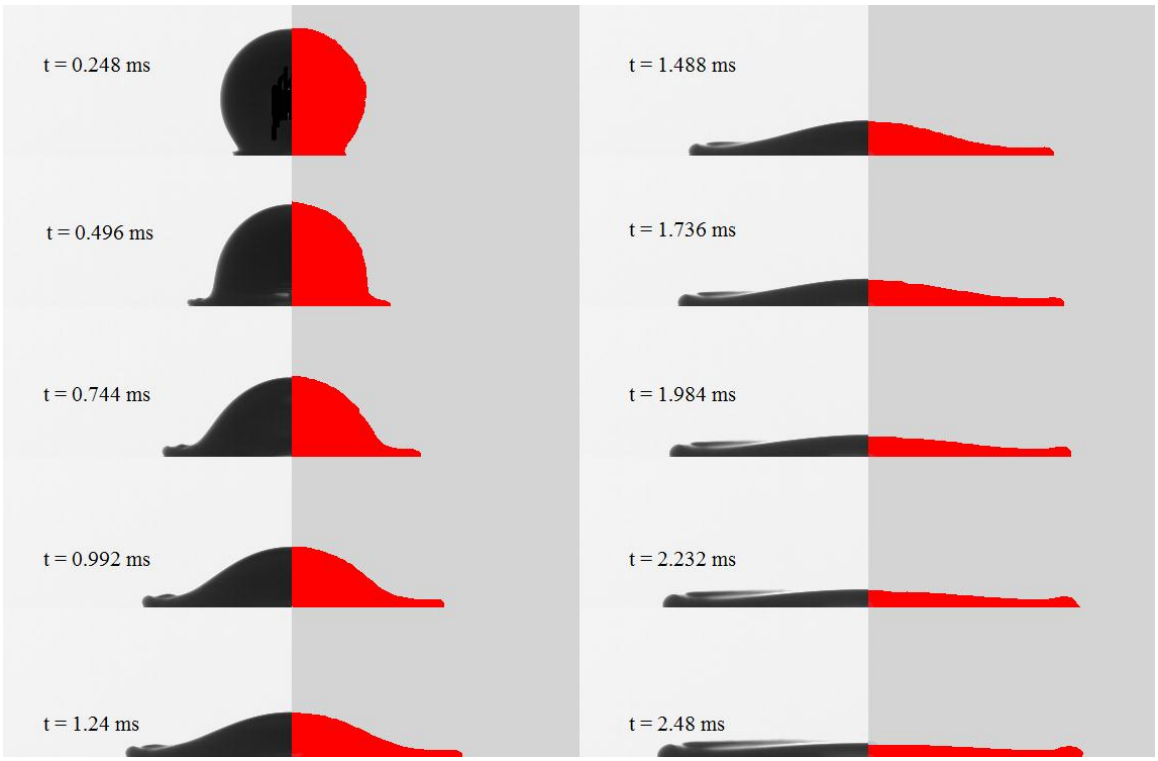

Figure 5-2 Computer generated images (right) compared with photographs of a diesel drop (left) impacting a glass surface with a velocity of 1.6 m/s.

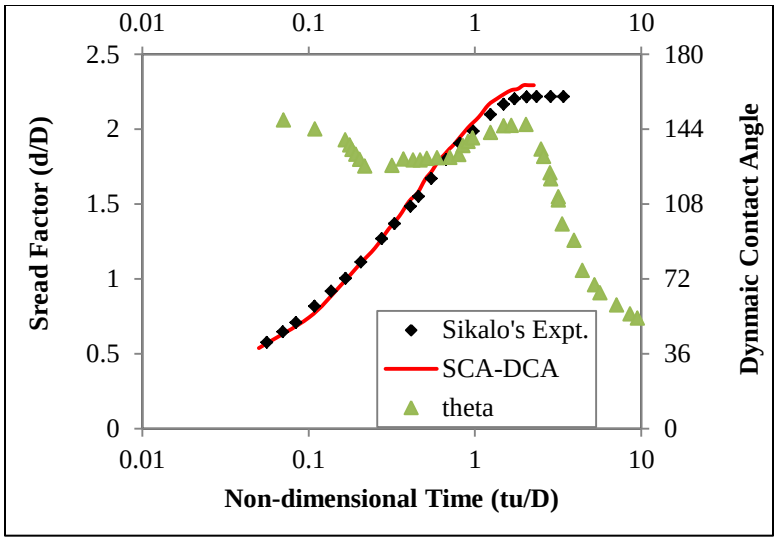

(a)

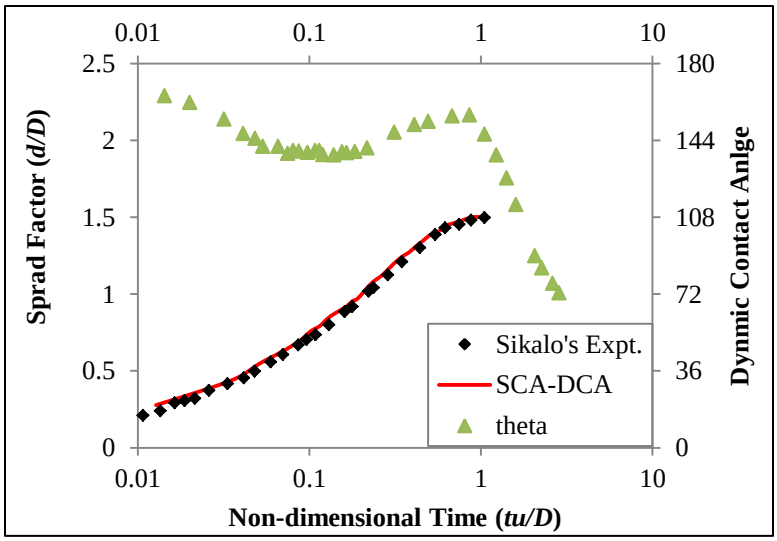

(b)

Figure 5-3 Experimental apparent dynamic contact angles and comparison of the experimental and numerical spread factors with the SCA-DCA model of the glycerin drop with impact speed (a) u = 4.1 m/s, (b) u = 1.04 m/s, and (c) u = 1.41 m/s

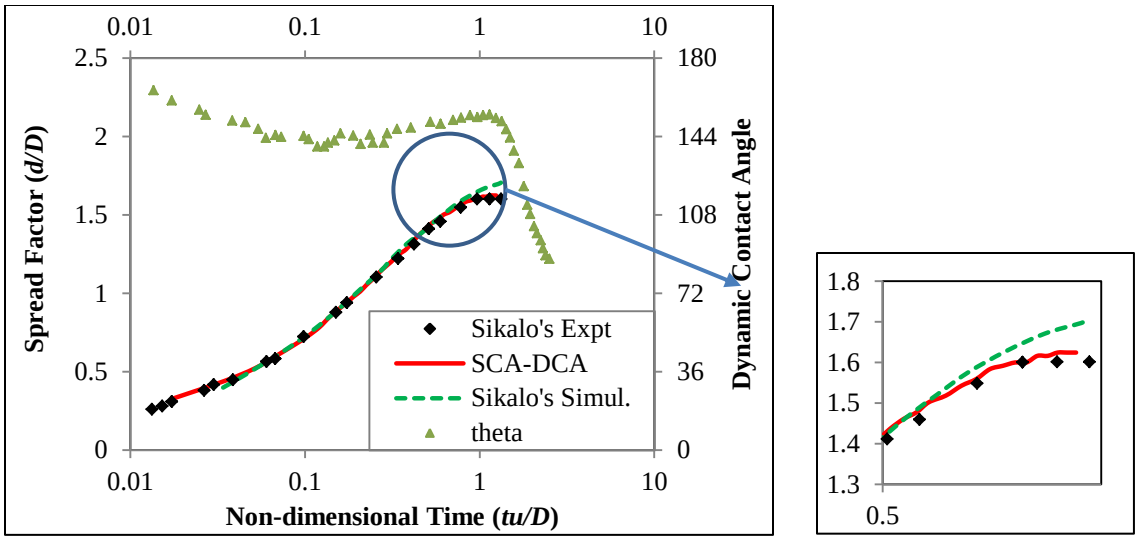

(c)

Figure 5-3--continued

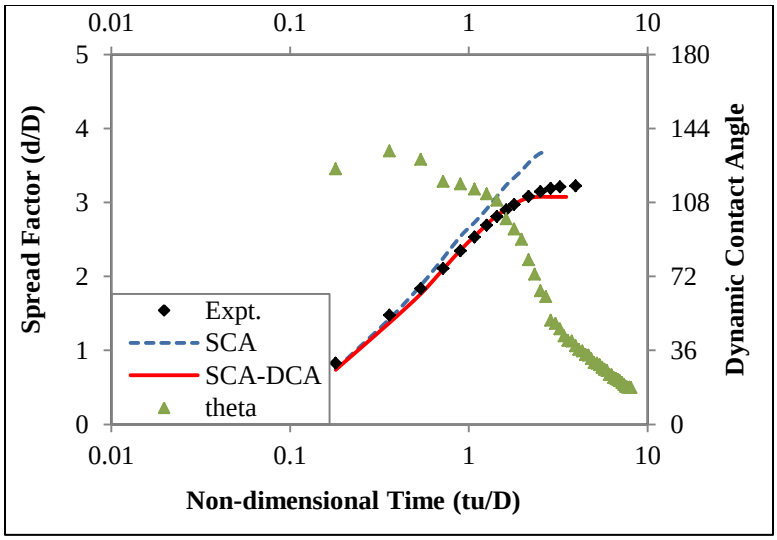

(a)

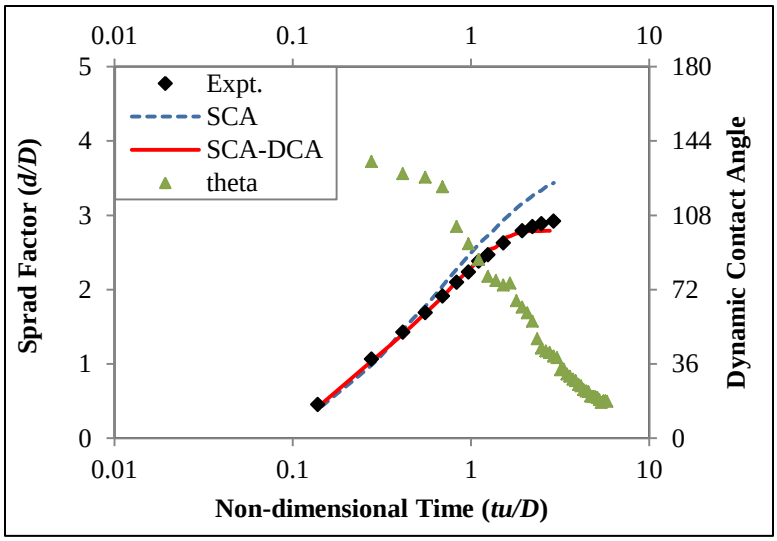

(b)

Figure 5-4 Experimental apparent dynamic contact angles and comparison of the experimental and numerical spread factors with the SCA-DCA model of a diesel drop with (a) u = 1.6 m/s, (b) u = 1.2 m/s, and (c) u = 0.7 m/s

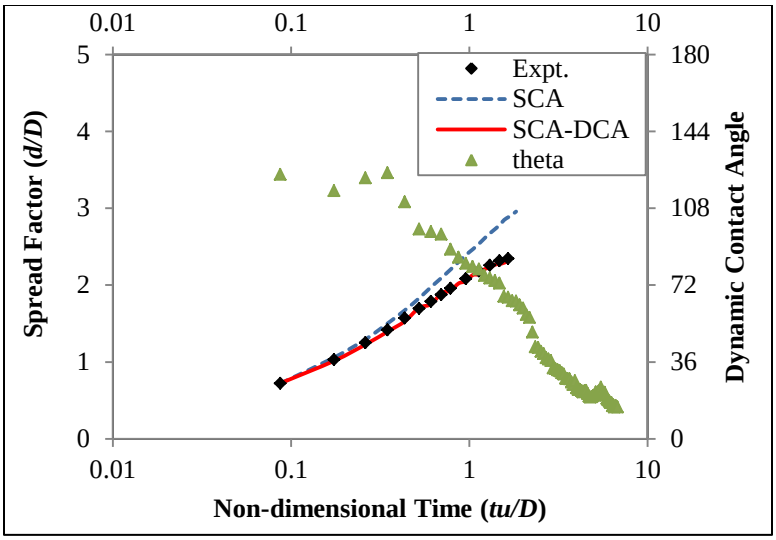

(c)

Figure 5-4--continued

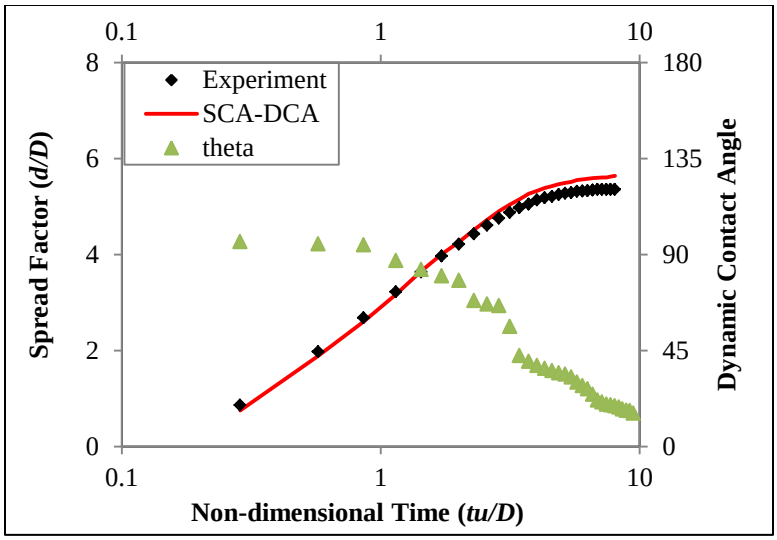

(a)

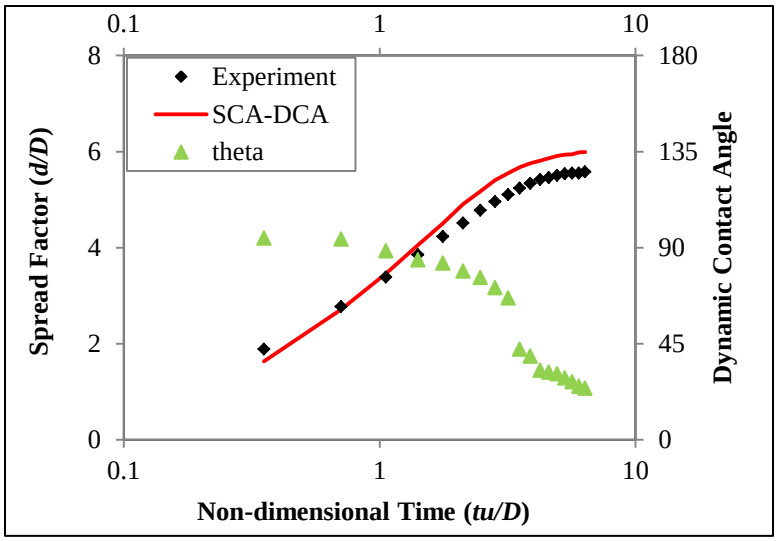

(b)

Figure 5-5 Experimental apparent dynamic contact angles and comparison of the experimental and numerical spread factors with the SCA-DCA model of a methanol drop with impact speed (a) u = 2.33 m/s and (b) u = 3.05 m/s

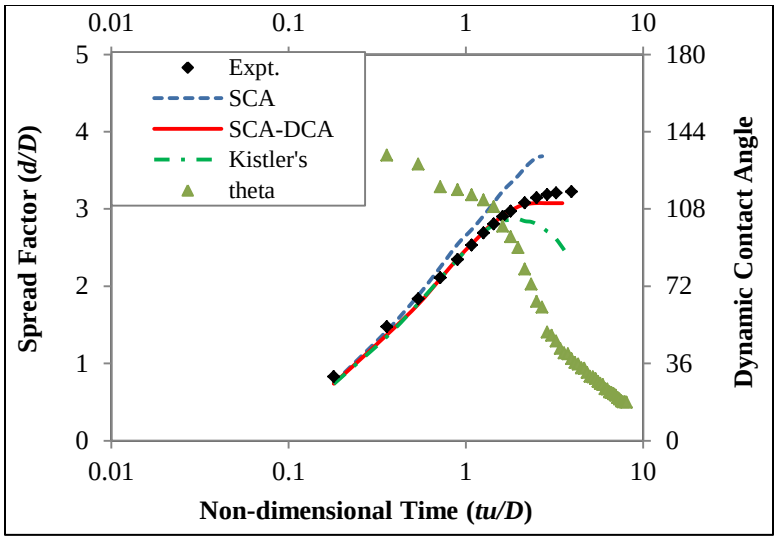

(a)

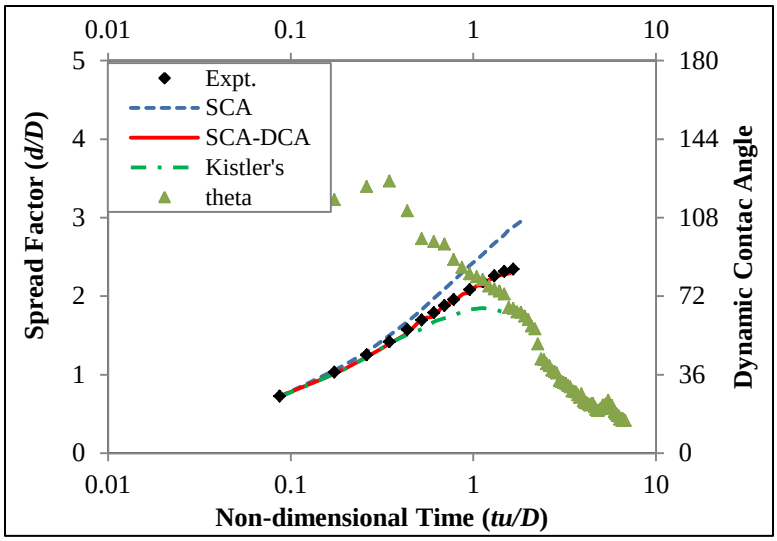

(b)

Figure 5-6 Comparison of the experimental and numerical spread factors with Kistler's model of a diesel drop with impact speed (a) u = 1.6 m/s and (b) u = 0.7 m/s

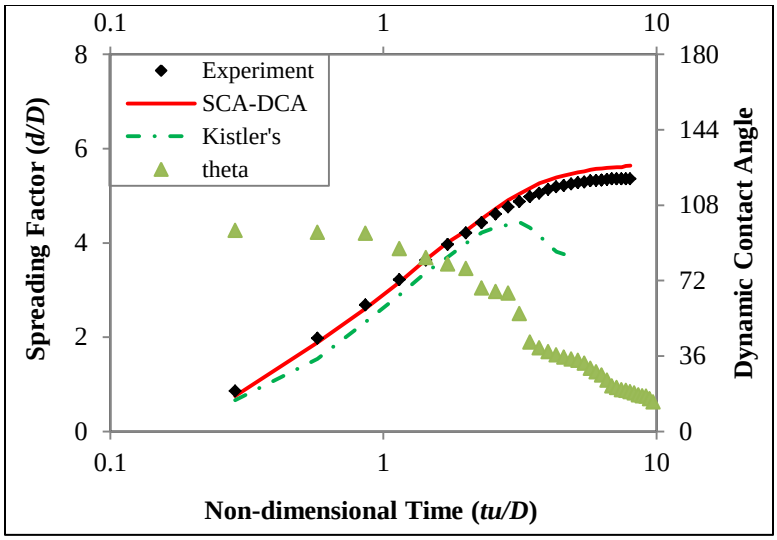

Figure 5-7 Comparison of the experimental and numerical spread factors with Kistler's model of a methanol drop with impact speed u = 2.33 m/s

CHAPTER 6: WATER DROP IMPACT WITH SCA-DCA MODEL

This chapter examines the applicable range of this newly proposed contact angle model. It has been proven that the combined SCA-DCA model can predict the spreading behaviors of hydrocarbon drops impact on a solid smooth flat surface (glass). In that case, it might be interesting to broaden the applicability from hydrocarbon drops to water drops. Also it would be helpful if this applicable range could be generalized in terms of dimensionless numbers (Re, We, or Oh), providing a decent reference for the future studies.

Since the SCA-DCA model is developed on the basis of two-regimen spreading behavior, it is apparent that it won't be applied to the prompt splashing behavior (secondary droplets are ejected from the tip of the lamella at the instance when the drop impact on the surface). For other impact modes, such as rebounding and corona splashing (secondary droplets are ejected from the tip of the lamella in the end of spreading regime), this SCA-DCA model might be applicable for the kinetic and spreading regimes. However, since the time range of spreading behavior is much shorter than other parts of bouncing and splashing modes, these two modes would not be of interest in this work. Thus, only the spreading mode would be considered for the water drop impact. In that case, to validate the SCA-DCA model for water drops, we are looking for experimental data of water drop spreading on solid flat surface.

Several published experimental data were utilized and compared with our model. They are from Roisman et al. (Roisman, et al., 2008), Fukai et al. (Fukai, et al., 1995), and Wang et al. (M. Wang, et al., 2009a). The details of the experimental conditions are listed in Table 6-1. Note that the experimental data vary with the range of $We = O(0.1) - O(100)$, $\mathrm{Re} = O(100) - O(1000)$, $Oh = O(0.001)$. Water drops impact on three different surfaces: stainless steel, Pyrex glass, and cleaned glass. All the experiments were taken under atmospheric pressure and room temperature. Thus, the

properties of water liquid can be approximated to be the same. Details of water properties are listed in Table 6-2. It is noted that the surface tension of water is even higher than glycerin. Therefore, the 2-D mesh is applicable for the numerical calculations.

6.1 Experimental Investigation

Before starting to validate the numerical model, experimental data should be analyzed in order to understand the physical behaviors beyond. Again, spreading factors were plotted in terms of the dimensionless time to compare the results from different experiments. From Figure 6-1, it could be observed that after water drops impact on the surface, spread factor shows a significant increase during a short time (~10 ms), where the inertial energy is quickly dissipated. The drop spreads out fast and reaches to its maximum diameter, and then two different behaviors are displayed: 1) the spread diameter remains almost as a constant, arrested by the surface tension force, which is similar to the situations of hydrocarbon drops; 2) the drop starts receding and the spread diameter decreases. These two behaviors occurred because the wettability and surface roughness of surfaces are different. It is noted that the wettability of Pyrex glass is much smaller than the ones of stainless steel and glass.

The evolution of dynamic contact angle is also investigated and compared. Here, the data of dynamic contact angles are only available in cases 1-3 and case 7. Figure 6-2 shows the varying trends of contact angles on stainless steel and glass separately. Again, it is apparent that the evolutions of apparent dynamic contact angles are significantly different on two surfaces. When the water drop is receding, contact angle oscillates back and forth on the stainless steel due to the high surface roughness. In contrast, contact angle decreases smoothly with time on the glass surface since the glass substrate is smoother. In such a case, Equation (18) would not be applicable for cases 1-3 due to the oscillations. On the other hand, since case 7 is also performed on a cleaned glass, which

is close to the substrate used in our experiments, it is expected that Equation (18) could also predict the evolution of contact angle in case 7.

Even though Equation (18) is not applicable for stainless steel surface, it is still of interest to see whether a generalized equation could be observed. From Figure 6-2, it could be observed that the contact angles keep almost as a constant around 120 degree and then start oscillating. Again, similar to hydrocarbon drops, the reason why apparent dynamic contact angle keeps as a constant is because the drop shape is a truncated sphere during this regime, noted as the kinetic regime. After that, the water drop spreads out and the contact angle varies, noted as spreading regime. Due to the high surface roughness of stainless steel, the dynamic contact angle (namely, the tip of the lamella) is jiggling back and forth when the drop is spreading outwards. This transition instance from kinetic regime to spreading regime could be also calculated according to the power law generalized from Figure 3-12, $t^* = 0.05\,\mathrm{Re}^{0.45}$. This predicted result from the power law is in good agreement with the one observed from the picture. Therefore, by cutting off the kinetic regime, and rescaling the time line ($t^{**} = tu / D - t^*$), Figure 6-3 shows the evolutions of contact angles in the rest regime. It is apparent that no general trend exists during this regime. Thus, for stainless steel surface, the SCA-DCA model will not be applicable.

In case 7, water drops impact on a cleaned glass surface. Therefore, the trend of contact angle is similar to the ones of hydrocarbon drops (Figure 6-2b). By implementing Equation 18 into the spreading regime (the transition time is calculated according to the power law), it is shown that Equation 18 predicts a close trend, compared with the experimental data (Figure 6-4). The difference between predicted and experimental data occurs because the surface roughness is different. In our experiments, we were using the clean new glass and replaced the glass after each run. However, in case 7, the authors washed the glass with acid after each performance. Moreover, by comparing two papers published by the same author (M. Wang, et al., 2009a; M. Wang et al., 2009b), the

uncertainty of the experimental data in case 7 is more than 15% (the same data were presented in both papers with different initial impact velocities and initial diameters). Thus, Equation 18 could be applied for water impact on glass surface as long as the surface is clean enough.

6.2 Numerical Validation

Although the generalized equation (Eq. 18) only can be applied to the case where clean glass is used as the substrate, it is still worthwhile to investigate the idea of two-regime contact angle model whether is applicable for water drop spreading on other surfaces. Therefore, a static contact angle model is applied for each case to check its validation during the kinetic regime.

Figure 6-5 shows the comparisons of spread factors between experimental results and numerical predictions for case 1 and case 2. In Figure 6-5 (a), when $tu/D<0.61$, the predicted spread factor increases with time, showing a good agreement with the experimental data. When $tu/D>0.61$, a discrepancy between the predicted and experimental data starts, where the predicted angle is decreasing rather than remaining as constant. According to the evolution shown in the same plot, it is also apparent that $tu/D=0.61$ is the time instance when the oscillation of contact angle starts. Therefore, it confirms the conclusion made previously that the SCA model is applicable in the kinetic regime but fails in the spreading regime.

Similarly, in Figure 6-5 (b), it is shown that the SCA model predicts well during the time interval $0<tu/D<1.15$, but fails when $tu/D>1.15$. Again, by comparing the evolution of the dynamic contact angle, it is also clear that the time instance when the SCA model fails is the one when the oscillation of contact angle begins.

The SCA model is also applied for cases 4 and 5, where the water drop impacts on the Pyrex glass surface. Figure 6-6 shows the comparisons of spread factors between

experimental and numerical results. Again, by implementing the SCA model, the predicted dynamic contact angle increases with time, showing good accuracy; but a descending trend starts at $tu/D = 2.03$ (case 4) and $tu/D = 1.76$ (case 5) separately. Although the evolution of contact angle is not available for these two cases, the transition time instance still could be confirmed by comparing with the power law $t^* = 0.05\,\mathrm{Re}^{0.45}$.

Figure 6-7 broadens the application of the power law from hydrocarbon drops (Figure 3-12) to water drops. Here, the symbols of hydrocarbon drops are derived by counting the time when the evolutions of dynamic contact angles start showing a significant drop. Nevertheless, the symbols of water drops are derived from the comparisons of spread factors between the SCA model and experimental data. It is apparent that the power law, which is a function of Reynolds number, is applicable for all liquids and all substrates. Therefore, the numerical prediction from SCA model, the experimental evolution of contact angle, and the theoretical power law confirm the transition time (from kinetic regime to spreading regime) in three different aspects.

The SCA model is also tested for case 7, where the substrate is the acid cleaned glass. Figure 6-8 confirms that this model fails when the trend of contact angle starts descending (namely, the spreading regime starts). Since the substrate used in case 7 is the most close to the one used in our experiments, then it is believed that the SCA-DCA should be applicable for case 7. However, as shown in Figure 6-4, a large discrepancy between the experimental data and the theoretical values occurs in the early stage of the spreading regime. In such a case, the discrepancy destroyed the continuum of spreading when the DCA model (Eq. 18) is applied as the boundary condition. Figure 6-8 shows the effect of this discrepancy.

In sum, 1) the SCA model could be applied to the first regime (kinetic regime) of water drop spreading process; 2) The generalized equation (Eq. 18), namely, the DCA model, predicts a close trend to the second regime of evolution of dynamic contact angle. Based on these two conditions, it is believed that the SCA-DCA model should be

applicable for water drop spreading on a smooth solid surface. However, the high uncertainty of the raw data and the acid washed substrate (not as clean as ours) lead to the failure of SCA-DCA model in case 7. Therefore, due to the lack of experimental data, this conception could not be validated in this work.

Because of the success of the SCA model in the first regime and the applicability of Eq. 18 in the second regime, it is still believed that the SCA-DCA model could be applied to water drop spreading on a flat smooth surface (glass). According to this conception and previous success in hydrocarbon drops, it could be concluded that the SCA-DCA model could be applied to hydrocarbon and water drops impact on flat smooth solid surface, with the range of $We = O(1) - O(100)$, $\mathrm{Re} = O(10) - O(1000)$, $Oh = O(0.001) - O(0.1)$.

Table 6-1 Properties of Liquid Water at $T = 25°C$

Liquid	σ (mN/m)	μ (mPa s)	$\rho(kg/m^3)$
water	71.97	1.0	997

Table 6-2 Operation Conditions of Water Drops

Case	Substrate	u (m/s)	D (mm)	We	Re	Oh	Reference
1	stainless steel	0.16	2.50	0.88	443	0.00212	Roisman, et al., 2008
2	stainless steel	0.48	2.50	7.90	1329	0.00212	Roisman, et al., 2008
3	stainless steel	0.23	2.50	1.81	637	0.00212	Roisman, et al., 2008
4	Pyrex glass	2.09	3.70	111	4130	0.00255	Fukai, et al., 1995
5	Pyrex glass	1.50	3.76	58.40	3010	0.00254	Fukai, et al., 1995
6	Pyrex glass	3.76	3.74	364	7390	0.00258	Fukai, et al., 1995
7	glass	0.52	2.15	8.11	1121	0.00254	M. Wang et al., 2009

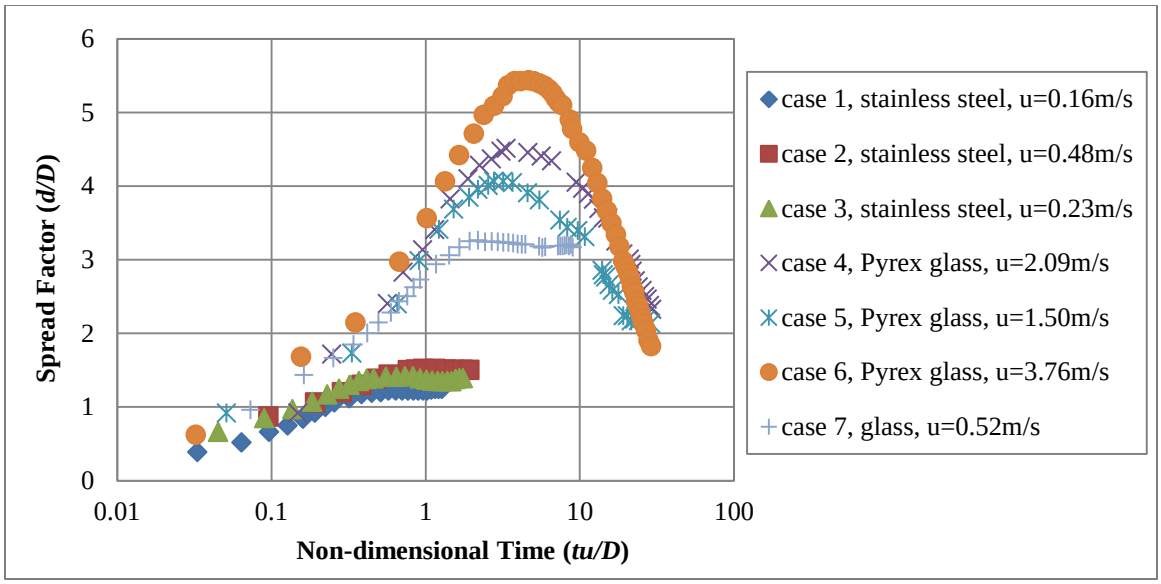

Figure 6-1 Spread factor of water drops for cases shown in Table 6-2.

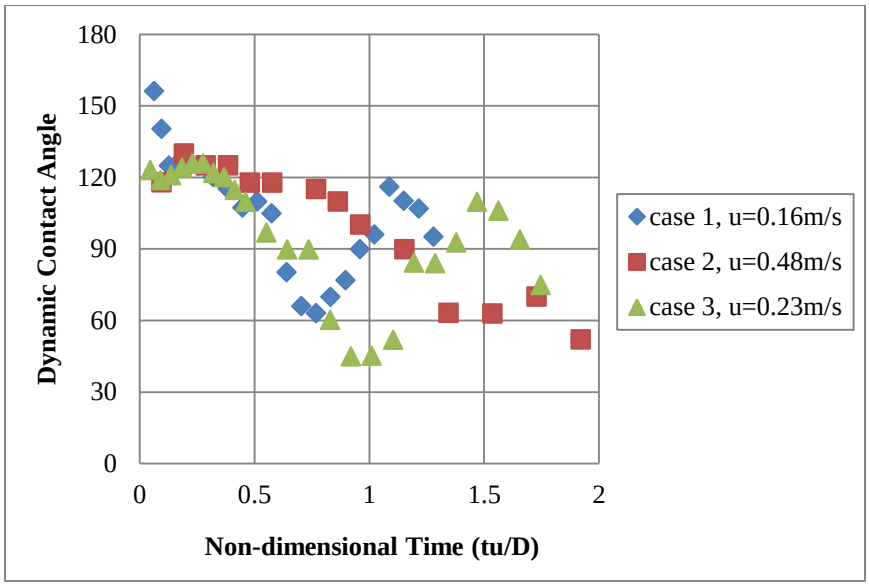

(a)

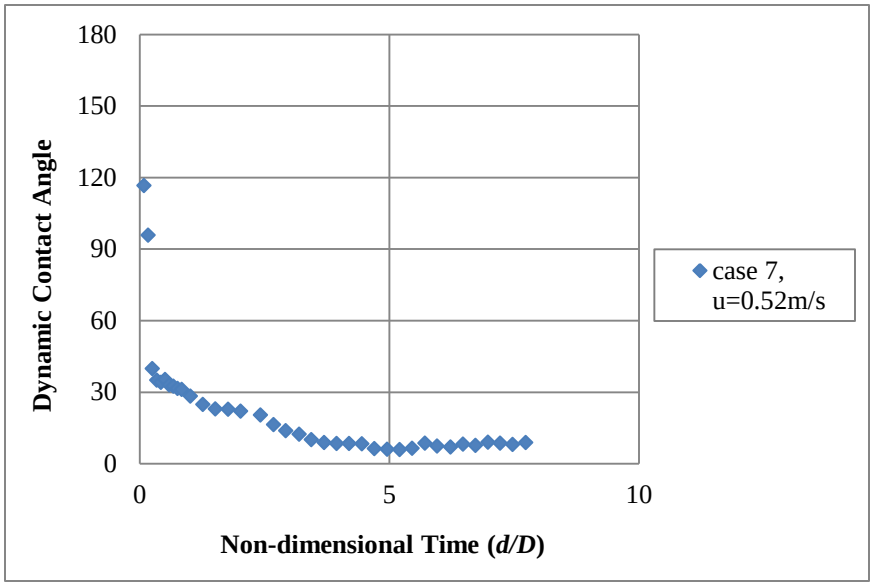

(b)

Figure 6-2 Evolutions of dynamic contact angle for water drops impact on (a) stainless steel and (b) glass.

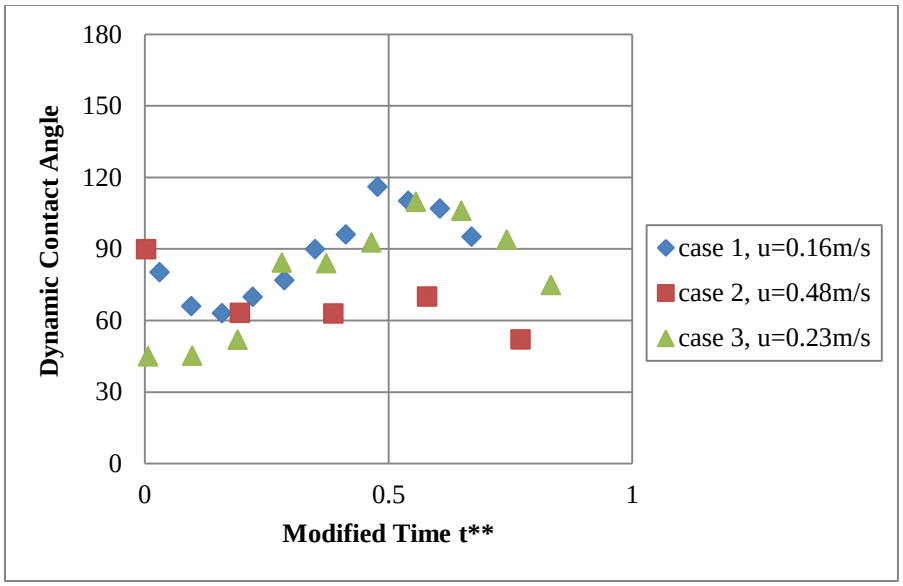

Figure 6-3 Evolutions of contact angles by cutting off the constant regime (stainless surface)

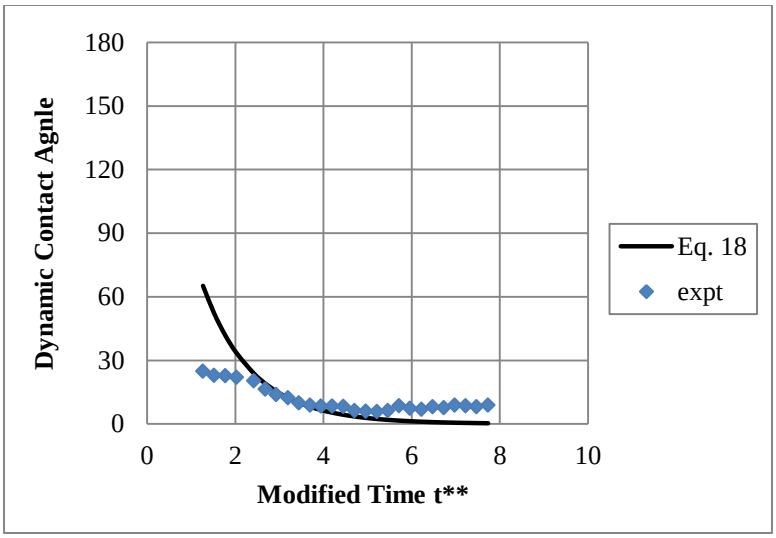

Figure 6-4 Evolutions of contact angle in spreading regime for case 7 (glass surface): experimental (symbol) and theoretical predicted (solid line).

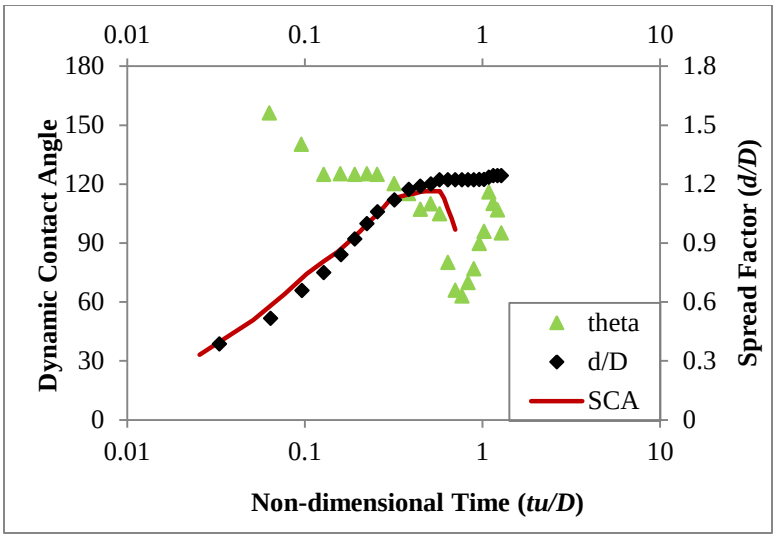

(a) Case 1

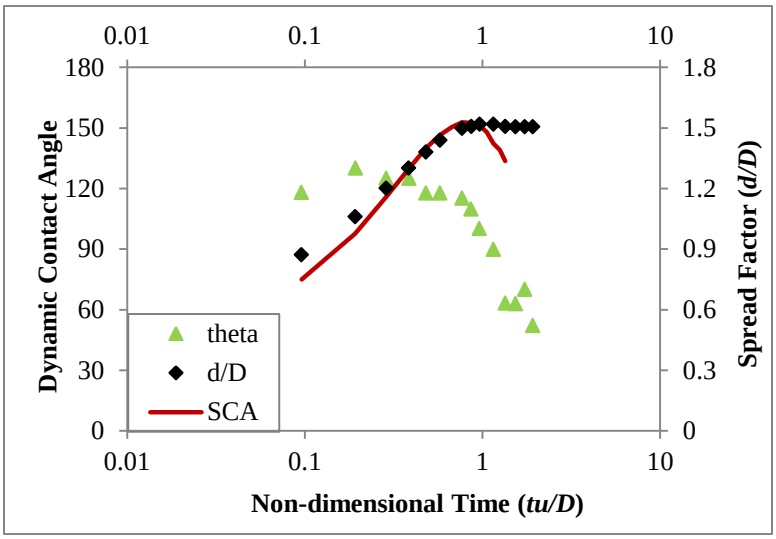

(b) Case 2

Figure 6-5 Comparison of the experimental and numerical spread factors with the SCA model for (a) case 1 and (b) case 2

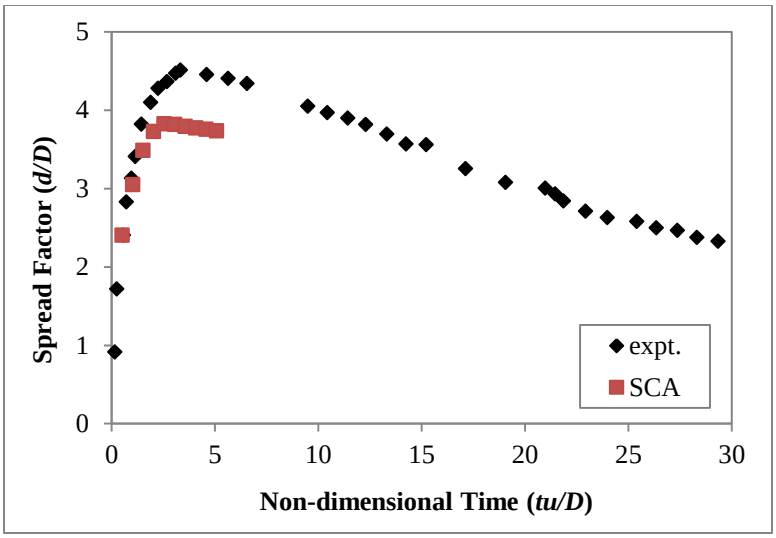

(a)

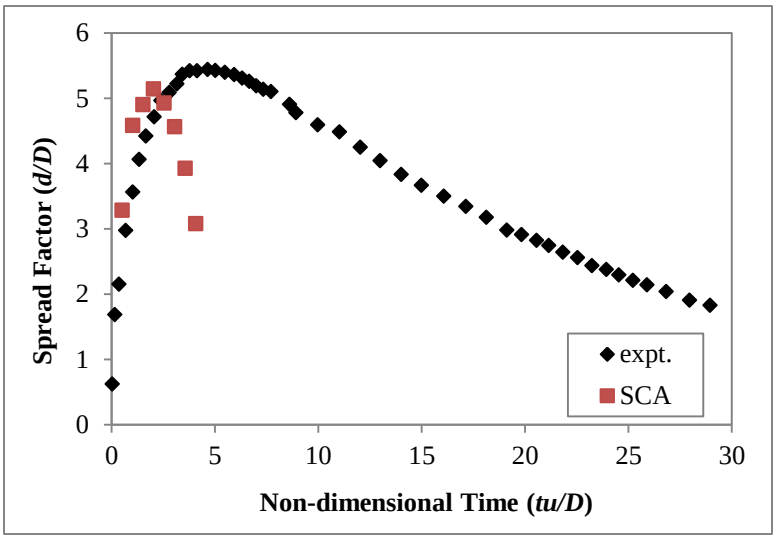

(b)

Figure 6-6 Comparison of the experimental and numerical spread factors with the SCA model for (a) case 4 and (b) case 5

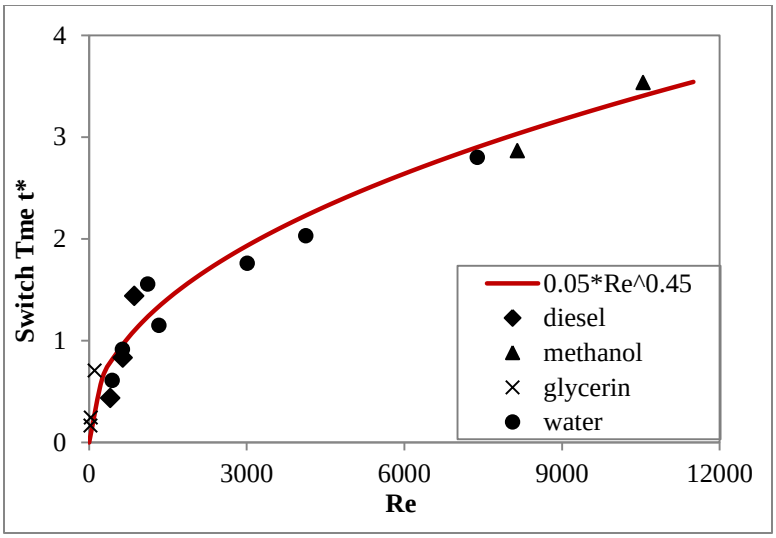

Figure 6-7 Transition time derived from experiments/simulations compared with the power law.

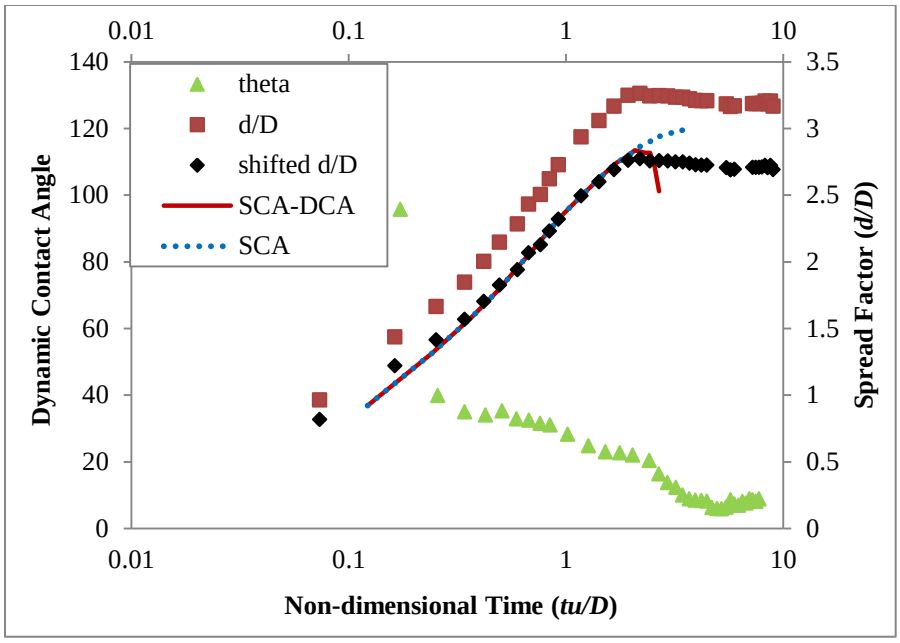

Figure 6-8 Comparisons of experimental data, SCA model, and SCA-DCA model. The experimental spread factor was shifted according to the experimental uncertainty.

CHAPTER 7: CONCLUSION

In this work, the dynamic behavior of impacting drops on a flat, smooth surface drops were investigated through experimental photography and numerical simulations. Three different hydrocarbon liquids were tested to provide a range of material properties and resulting in a range of observed behaviors. The two-phase spreading phenomena were characterized by the evolutions of the apparent dynamic contact angle and the spread factor. A combined SCA-DCA model was proposed on the basis of two-phase spreading phenomena and was employed as the boundary conditions in numerical simulations.

(1) Two-phase spreading of hydrocarbon drops

As evidenced in the experimental results, both the apparent dynamic contact angle and the spread factor show behavior that is consistent with a two regime system: a kinetic regime followed by a spreading regime. The kinetic regime is dominated by the kinetic energy and the spreading regime is governed by the interaction of viscous and surface tension forces. In particular, by cutting off Phase I, the evolution of the contact angles in Regime II coincided for drops with different impact velocities, implying that a general model could be utilized in Regime II. The transition time instance (when the spreading regime starts) follows with a power law in terms of Reynolds number. Furthermore, the maximum spread factor shows a nonlinear and non-monotonic behavior with the Weber number and the Reynolds number. This indicates that the behavior of the spread factor during the spreading phase does not simply depend on viscosity or surface tension, but a combination of these two. Thus, the Ohnesorge number, the ratio of viscous force to the inertia and surface tension, is suggested to describe the behavior of Regime II. It is also observed that the drop spreads faster with decreasing Ohnesorge number.

(2) The combined SCA-DCA model

A general exponential correlation in terms of Ohnesorge number is derived on the basis of experimental results, describing the behavior of apparent contact angle in the spreading phase. This general expression is employed as the boundary condition in the spreading phase, while the SCA model is substituted in the kinetic phase. By comparing the simulation results with the experimental data, this new SCA-DCA model shows better accuracy (error less than 7%), whereas the SCA model and Kistler's correlation (Kistler, 1993) have significantly greater error in Phase II. In addition, since only the values of θ_e and Oh number are needed in this new model, droplet experiments are not required for computation as with the full DCA models.

3) Applicable range of SCA-DCA model

Due to the success of SCA-DCA model on hydrocarbon drops, the next aspect of this study was to broaden the applicable range to include water drops. Published data for water drop spreading on three different surfaces (stainless steel, Pyrex glass, and clean glass) was utilized as the comparison data set. The application of the SCA model showed that the two-regime spreading behavior exists in all of the cases tested. It was also confirmed that the power law description was also applicable for water drops. Conversely, it was found that that the equation used for hydrocarbons (Eq. 18) could not be applied to the stainless steel surface cases, most likely due to surface characteristics that lead to oscillations in the dynamic contact angle. Nevertheless, the equation shows close agreement for the data for cleaned glass. Such a similarity exhibits the possibility of applying SCA-DCA model for the water drop spreading on the cleaned glass surface.

According to the successful validations for hydrocarbon drops and the conception for water drops, it could be concluded that the SCA-DCA model would be able to apply for hydrocarbon and water drops spreading on a flat smooth solid surface, with the range of $We = O(1) - O(100)$, $\mathrm{Re} = O(10) - O(1000)$, $Oh = O(0.001) - O(0.1)$.

CHAPTER 8: FUTURE WORK

The dynamics of hydrocarbon drops impacting on a flat solid surface have been well predicted and simulated by using the SCA-DCA model. Based on the existing findings reported in this work, several recommendations for the future work are given below:

1) Eliminate the limitation of the SCA-DCA model

Since the SCA-DCA model is limited to the flat smooth solid surface, the effect of surface roughness and wettability should be considered to eliminate this limitation. Specially, the wettability, which is related to the advancing contact angle θ_a and receding contact angle θ_r, has been widely studied, both experimentally and numerically. In previous studies, people have tried to implementing θ_a and θ_r into their numerical models, showing a better accuracy than the one without them (Roisman, et al., 2008). Therefore, it is expected that relating our model to these two angles will be able to eliminate the effect of wettability.

2) Numerical investigations on the behaviors of non-Newtonian drop impacting

As stated in the introduction part, a possible way of mitigating the accident crash induced fires is to prevent misting by mixing long chained polymer based additives into fuels. Such polymers are intended to impart non-Newtonian viscosity (shear-thickening) to fuels in a shear range that is typical of accidents but does not otherwise affect normal functioning of the fuel system. Such an increase of viscosity retards the break-up of a liquid into smaller droplets. A drop hitting a dry surface at moderate impact speeds experiences a wide range of strain rates during the resulting deformation; hence, this can be a suitable tool to test the viscosity variations of the polymer-fuel blends. Accordingly, computational simulation of non-Newtonian behavior becomes necessary as it lends a great flexibility in studying a particular range of strain rates. It also allows the desired variation of liquid properties in order to study the resultant effects on quantities of

interest – like drop shapes and impacting velocities – without actually doing tests. However, such polymer-fuel blends are still in the development stages. Even though the experiments that we have been tested so far provided insights regarding the effect of polymer additive on flow characteristics of diesel, it is still not possible to obtain a non-Newtonian liquid without changing its Newtonian viscosity. Consequently, the success of blending the fuel liquid with polymer additives becomes an important precondition. In particular, diesel fuel would be primary solvent that needs to be tested, and if such a test fails, then methanol and other hydrocarbon liquids would be taken into the consideration.

3) Broaden the SCA-DCA model to predict the splashing behavior

Although only spreading behavior is examined in this work, the transition from spreading to splashing, namely, the splashing threshold, remains an important issue for the studies of drop impacts on the solid surface. It has been realized that Kelvin-Helmholtz instability theory is the key to explain the mechanism of the splashing phenomenon. In particular, the ambient pressure, or the air density, has a significant effect on the threshold and trajectory of splashing (Liu, et al., 2010; N. K. Mishra, et al., 2011). Several semi-empirical splash threshold correlation related to the ambient pressure were derived and showed good agreement with the experimental data (Liu, et al., 2010; L. Xu, et al., 2005). Beyond the pressure, other properties, such as the impact speed, drop size, liquid viscosity, and surface tension also have an effect on the tendency of splashing (Engel, 1955; Levin & Hobbs, 1971; Scheller & Bousfield, 1995; Šikalo, et al., 2002; L. Xu, et al., 2005; X. Zhang & Basaran, 1997). However, there are no specific correlations relate these properties to the splashing threshold as the ambient pressure does. Given that the SCA-DCA model is only valid for the two-phase spreading behavior, it would be instructive to use this model to predict the splashing behavior by varying properties of the impacting drop. Such a numerical simulation would also offer a priori knowledge of experimental studies.

BIBLIOGRAPHY

Ameri David, R. L., Wei, M., Liu, D., Bathel, B. F., Plog, J. P., Ratner, A., & Kornfield, J. A. (2009). Effects of pairwise, self-associating functional side groups on polymer solubility, solution viscosity, and mist control. *Macromolecules, 42*(4), 1380-1391.

Baiocci, C., & Pukhnachev, V. V. (1990). Problems with one-sided constraints for Navier-Stokes equations and the dynamic contact angle. *J. Appl. Mech. Techn. Phys., 2*, 27-40.

Berg, J. C. (Ed.). (1993). *Wettability*. New York: Dekker.

Blake, T. D. (2006). The physics of moving wetting lines. *Journal of Colloid and Interface Science, 299*, 1-13.

Blake, T. D., & Haynes, J. M. (1969). Kinetics of liquid/liquid displacement. *J. Colloid Interface Sci., 30*, 421-423.

Boender, W., Chesters, A. K., & Zanden, A. J. J. v. d. (1991). An approximate analytical solution of the hydrodynamic problem associated with an advancing liquid-gas contact line. *Intl J. Multiphase Flow, 17*, 661-676.

Brackbill, J. U., Kothe, D. B., & Zemach, C. (1992). A continuum method for modeling surface tension. *J. Comput. Phys., 100*.

Braun, R. J., Murray, B. T., Boettinger, W. J., & McFadden, G. B. (1995). Lubrication theory for reactive spreading of a thin drop. *Phys. Fluids, 7*.

Bunn, T. L., Slavova, S., & Robertson, M. (2012). Crash and burn? Vehicle, collision, and driver factors that influence motor vehicle collision fires. *Accident Analysis and Prevention, 47*, 140-145.

Bussmann, M., Chandra, S., & Mostaghimi, J. (2000). Modeling the splash of a droplet impacting a solid surface. *Phys. Fluids 12*, 3121-3132.

Bussmann, M., Mostaghimi, J., & Chandra, S. (1999). On a three-dimensional volume tracking model of droplet impact. *Phys. Fluids 11*, 1406-1417.

Chen, S., & Doolen, G. D. (1998). Lattice Boltzmann methods for fluid flows. *Annu. Rev. Fluid Mech., 30*, 329-364.

Cherry, B. W., & Holmes, C. M. (1969). Kinetics of wetting of surfaces by polymers. *J. Colloid Interface Sci., 29*, 174-176.

Cooper-White, J. J., Crooks, R. C., & Boger, D. V. (2002). A drop impact study of worm-like viscoelastic surfactant solutions. *Colloid Surf. A, 210*, 105-123.

Cossali, G. E., Coghe, A., & Marengo, M. (1997). The impact of a single drop on a wetted solid surface. *Exp. Fluids, 22*, 463-472.

Cossali, G. E., Marengo, M., Coghe, A., & Zhdanov, S. (2004). The role of time in single drop splash on thin film. *Exp. Fluids, 36*, 888-900.

Cox, R. G. (1986). The dynamics of the spreading of liquids on a solid surface. Part 1. Viscous flow. *J. Fluid Mech., 168*, 169-194.

de Gennes, P. G. (1985). Wetting: statics and dynamics. *Rev. Mod. Phys, 57*, 827-863.

Dear, J. P., & Field, J. E. (1988). High-speed photography of surface geometry effects in liquid/solid impact. *J. Appl. Phys., 63*, 1015-1021.

Dussan V., E. B. (1976). The moving contact line: the slip boundary condition. *J. Fluid Mech., 77*, 665-684.

Dussan V., E. B. (1979). On the spreading of liquids on solid surfaces: static and dynamic contact lines. *Ann. Rev. Fluid Mech., 11*, 371-400.

Ehrhard, P., & Davis, S. H. (1991). Non-isothermal spreading of liquid drops on horizontal plates. *J. Fluid Mech., 229*, 365-388.

Engel, O. (1955). A water drop collision with solid surfaces. *PJ Res Nat Bur Stand 54*, 281-298.

Field, J. E., Davies, P. N. H., & Lesser, M. B. (1979). *Theoretical and experimental studies of two-dimensional liquid impact.* Paper presented at the Proc. 5th Int. Conf. on Erosion by Solid and Liquid Impact, Cambridge.

Finlow, D. E., Kota, P. R., & Bose, A. (1996). Investigation of wetting hydrodynamics using numerical simulations. *Phys. Fluids, 8*.

Frenkel, J. I. (1946). *Kinetic Theory of Liquids*. Oxford: Oxford Univ. Press.

Fukai, J., Shiiba, Y., Yamamoto, T., Miyatake, O., Poulikakos, D., Megardis, C. M., & Zhao, Z. (1995). Wetting effects on the spreading of a liquid droplet colliding with a flat surface: Experiment and modeling. *Phys. Fluids, 7*, 236.

Gentner, F., Rioboo, R., Baland, J. P., & Coninck, J. D. (2004). Low inertia impact dynamics for nanodrops. *Langmuir, 20*, 4748-4755.

Glasstone, S., Laidler, K. J., & Eyring, H. J. (1941). *The Theory of Rate Processes*. New York: McGraw–Hill.

Goodwin, R., & Homsy, G. M. (1991). Viscous flow down a slope in the vicinity of a contact line. *Phys. Fluids, 3*(4).

Greenspan, H. P. (1978). On the motion of a small viscous droplet that wets a surface. *J. Fluid Mech., 84*, 125-143.

Gunjal, P. R., Ranade, V. V., & Chaudhari, R. V. (2005). Dynamics of drop impact on solid surface: experiments and VOF simulations. *AIChE Journal, 51*(1), 59-78.

Haley, P. J., & Miksis, M. J. (1991). The effect of the contact line on droplet spreading. *J. Fluid Mech., 223*, 57-81.

Hansen, R. J., & Toong, T. Y. (1971). Dynamic contact angle and its relationship to forces of hydrodynamic origin. *J. Colloid Interface Sci., 37*.

Harlow, F. H., & Welch, J. E. (1966). Numerical study of large-amplitude free-surface motions. *Phys. Fluids, 8*, 842-851.

He, G., & Hadjiconstantinou, N. G. (2003). A molecular view of Tanner's law: molecular dynamics simulations of droplet spreading. *J. Fluid Mech., 497*, 123-132.

Hirt, C., & Nichols, B. (1981). Volume of fluid /VOF/ method for the dynamics of free boundaries. *Journal of Computational Physics*, 201-225.

Hocking, L. M. (1977). A moving fluid interface. Part 2. The removal of the force singularity by a slip flow. *J. Fluid Mech., 79*, 209-229.

Hocking, L. M. (1990). Spreading and instability of a viscous fluid sheet. *J. Fluid Mech., 211*, 373-392.

Hocking, L. M. (1992). Rival contact-angle models and the spreading of drops. *J. Fluid Mech., 239*, 671-681.

Hocking, L. M., & Rivers, A. D. (1982). The spreading of a drop by capillary action. *J. Fluid Mech., 121*, 425-442.

Hoffman, R. L. (1974). A study of the advancing interface. I. Interface shape in liquid-gas systems. *Journal of Colloid and Interface Science, 50*(2), 228-241.

Hopf, W., & Geidel, T. (1987). The dynamic contact angle I. Dependence of the receding contact angle on velocity in the surfactant-containing three-phase system. *Colloid Polym. Sci., 265*, 1075-1084.

Huh, C., & Scriven, L. E. (1971). Hydrodynamic model of steady movement of a solid/liquid/fluid contact line. *J. Colloid Interface Sci., 35*.

Jacqmin, D. (1999). Calculation of two-phase Navier-Stokes flows using phase-field modeling. *J. Comput. Phys., 155*, 96-127.

Jayaratne, O. W., & Mason, a. B. J. (1964). The coalescence and bouncing of water drops at an air/water interface. *Proc. R. Soc. London A, 280*, 545-565.

Jepsen, R. A., Yoon, S. S., & Demosthenous, B. (2006). Effects of air on splashing of a large droplet impact: experimental and numerical investigations. *At. Sprays, 16*(8), 981-996.

Jiang, T., Oh, S., & Slattery, J. C. (1978). Correlation for dynamic contact angle. *Journal of Colloid and Interface Science, 69*(1).

Kelecy, F. J., & Plethcer, R. H. (1997). The development of a free surface capturing approach for multidimensional free surface flows in closed containers. *J. Comput. Phys., 138*, 939-980.

Kim, H.-Y. (Chun, J. -H.). The recoiling of liquid droplets upon collision with solid surfaces. *Phys. Fluids, 13*, 643-659.

Kistler, S. F. (1993). Hydrodynamics of wetting. In J. C. Berg (Ed.), *Wettability* (pp. 311). New York: Marcel Dekker.

Lamb, H. S. (1932). *Hydrodynamics*. London: J. & C. F. Clay.

Leneweit, G., Koehler, R., Roesner, K., & Schäfer, G. (2005). Regimes of drop morphology in oblique impact on deep fluids. *J. Fluid Mech., 543,* 303-331.

Levin, Z., & Hobbs, P. V. (1971). Splashing of water drops on solid and wetted surfaces: Hydrodynamics and charge separation. *Phil. Trans. R. Soc. Lond. A, 269*, 555-585.

Levine, S., Lowndes, J., Watson, E. J., & Neale, G. (1980). A theory of capillary rise of a liquid in a vertical cylindrical tube and in a parallel-plate channel: Washburn equation modified to account for the meniscus with slippage at the contact line. *J. Colloid Interface Sci., 73*.

Liu, J., Vu, H., Yoon, S., Jepsen, R., & Aguilar, G. (2010). Splashing phenomena during liquid droplet impact. *At. Sprays, 20*(4), 293-310.

Lunkad, S. F., Buwa, V. V., & Nigam, K. D. P. (2007). Numerical simulations of drop impact and spreading on horizontal and inclined surfaces. *Chemical Engineering Science 62,* 7214-7224.

Mao, T., Kuhn, D. C. S., & Tran, H. (1997). Spread and rebound of liquid droplets upon impact on flat surface. *AIChE J., 43*(9), 2169-2179.

Miller, C. A., & Neogi, P. (1985). *Interfacial Phenomena: Equilibrium and Dynamic Effects*. New York: CRC Press.

Mishra, N. K. (2009). *Effect of Chamber Pressure on Liquid Drop Impacts on a Stationary Smooth and Dry Surface.* Master M. Eng. Thesis, the University of Iowa, Iowa City.

Mishra, N. K., Zhang, Y., & Ratner, A. (2011). Effect of chamber pressure on spreading and splashing of liquid drops upon impact on a dry smooth stationary surface. *Experiments Fluids, 51*(2), 483-491.

Mourougou-Candoni, N., Prunet-Foch, B., Legay, F., Vignes-Adler, M., & Wong, K. (1997). Influence of dynamic surface tension on the spreading of surfactant solution droplets impacting onto a low-surface-energy solid substrate. *J. Colloid Interface Sci., 192*(1), 129-141.

Mukherjee, S., & Abraham, J. (2007). Investigations of drop impact on dry walls with a lattice-Boltzmann model. *Journal of Colloid and Interface Science, 312*, 341-354.

Mundo, C. H., Sommerfeld, M., & Tropea, C. (1995). Droplet-wall collisions: experimental studies of the deformation and breakup process. *Int. J. Multiphase Flow, 21*, 151-173.

Okawa, T., Shiraishi, T., & Mori, T. (2006). Production of secondary drops during the single water drop impact onto a plane water surface. *Experiments in Fluids, 41*(6), 965-974.

Okawa, T., Shiraishi, T., & Mori, T. (2008). Effect of impingement angle on the outcome of single water drop impact onto a plane water surface. *Exp. Fluids, 44*, 331-339.

Osher, S., & Sethian, J. A. (1988). Fronts propagating with curvature dependent speed: Algorithms based on Hamilton-Jacobi Formulations. *J. Comput. Phys., 79,* 12-49.

Pasandideh-Fard, M., Chandra, S., & Mostaghimi, J. (2002). A Three-Dimensional Model of Droplet Impact and Solidification. *International Journal of Heat and Mass Transfer, 45*(11), 2229-2242.

Pasandideh-Fard, M., Qiao, Y. M., Chandra, S., & Mostaghimi, J. (1996). Capillary effects during droplet impact on a solid surface. *Physics of fluids 8,* 650-659.

Petrov, J. G., & Radoev, B. P. (1981). Steady motion of the three phase contact line in model Langmuir-Blodgett system. *Colloid Polym. Sci., 259,* 753-760.

Pismen, L. M., & Nir, A. (1982). Motion of a contact line. *Phys. Fluids, 25*.

Pukhnachev, V. V., & Solonnikov, V. A. (1983). On the problem of dynamic contact angle. *J. Appl. Maths Mech., 46,* 961-971.

Range, K., & Feuillebois, F. (1998). Influence of surface roughness on a liquid drop impact. *J. Colloid Interface Sci., 203,* 16-30.

Ratner, A. (2009). Mitigating Crash Fires with Fuel Additives. *UTC Spotlight*

Rein, M. (1993). Phenomena of liquid drop impact on solid and liquid surfaces. *Fluid Dynamics Research, 12,* 61-93.

Rein, M. (Ed.). (2002). *Drop-surface interactions*. New York: Springer Wien.

Rein, M., & Deplanque, J. P. (2008). The role of air entrainment on the outcome of a drop impact on a solid surface. *Acta. Mech., 20,* 105-118.

Rioboo, R., Bauthier, C., Conti, J., Voue, M., & De Coninck, J. (2003). Experimental investigation of splash and crown formation during single drop impact on wetted surfaces. *Exp. Fluids, 35,* 648-652.

Rioboo, R., Marengo, M., & Tropea, C. (2002). Time evolution of liquid drop impact onto solid, dry surface. *Experiments in Fluids, 33,* 112-124.

Rioboo, R., Tropea, C., & Marengo, M. (2001). Outcomes from a drop impact on solid surfaces. *At. Sprays, 11,* 155-165.

Rodriguez, F., & Mesler, R. (1988). The penetration of drop-formed vortex rings into pools of liquid. *J. Colloid Interface Sci., 121*(1), 121-129.

Roisman, I. V., Opfer, L., Tropea, C., Raessi, M., Mostaghimi, J., & Chandra, S. (2008). Drops impact onto a dry surface: Role of the dynamic contact angle. *Colloids and Surfaces A: Physicochem. Eng. Aspects, 322,* 183-191.

Roisman, I. V., Rioboo, R., & Tropea, C. (2002). Normal impact of a liquid drop on a dry surface: model for spreading and receding. *Proc. R. Soc. Lond. A*(458), 1411-1430.

Ruckenstein, E., & Dunn, C. S. (1978). Stability of thin solid films. *Thin Solid Films, 51*(1), 43-75.

Ryskin, G., & Leal, L. G. (1984). Numerical solution of free-boundary problems in fluid mechanics. Part I. The finite-difference technique. *J. Fluid Mech., 148*, 1-17.

Scheller, B. L., & Bousfield, D. W. (1995). Newtonian drop impact with a solid surface. *AIChE Journal, 41*(6), 1357-1367.

Schwartz, A. M., & Tejada, S. B. (1970). NASA Contract Report CR 72728.

Schwartz, A. M., & Tejada, S. B. (1972). Studies of dynamic contact angles on solids. *J. Colloid Interface Sci., 38*(2), 359-375.

Shen, C. L., Xie, W. J., & Wei, B. (2010). Parametrically excited sectorial oscillation of liquid drops floating in ultrasound. *Phys. Rev. E., 81*(046305), 1-6.

Shikhmurzaev, Y. D. (1997). Moving contact lines in liquid/liquid/solid systems. *J. Fluid Mech., 334*, 211-249.

Šikalo, Š., Marengo, M., Tropea, C., & Ganic, E. N. (2002). Analysis of impact of droplets on horizontal surfaces. *Exp. Ther. Fluid. Sci., 25*(7), 503-510.

Šikalo, Š., Wilhelm, H. D., Roisman, I. V., Jakirlic, S., & Tropea, C. (2005). Dynamics contact angle of spreading droplets: Experiments and simulations. *Physics of Fluids 17*(062013), 1-13.

Siscoe, G. L., & Levin, Z. (1971). Water-drop-surface-wave interactions. *J. Geophys. Res., 76*(21), 5112-5116.

Smith, H. J. (1975). *The hydrodynamic and physico-chemical basis of the drop picture method*. Göttingen: Max-Planck-Institut für Strömungsforschung.

Stow, C. D., & Hadfield, M. G. (1981). An experimental investigation of fluid flow resulting from the impact of a water drop with an unyielding dry surface. *Proc R Soc London, 373*, 419-441.

Ström, G., Fredriksson, M., & Stenius, P. (1990). Kinetics of oil displacement from a solid surface by an aqueous solution. *J. Colloid Interface Sci., 134*(1), 117-121.

Ström, G., Fredriksson, M., Stenius, P., & Radoev, B. (1990). Kinetics of steady-state wetting. *J. Colloid Interface Sci., 134*(1), 107-116.

Tanner, L. H. (1979). The spreading of silicone oil drops on horizontal surfaces. *J. Phys. D: Appl. Phys., 12*.

Tryggvason, G., Bunner, B., Esmaeeli, A., Juric, D., Al-Rawahi, N., Tauber, W., . . . Janz, Y.-J. (2001). A front-tracking method for the computations of multiphase flow. *J. Comput. Phys., 169*(2), 708-759.

Vander Wal, R. L., Berger, G. M., & Mozes, S. D. (2006). The splash/non-splash boundary upon a dry surface and thin fluid film. *Exp. Fluids, 40*, 53-59.

Voinov, O. V. (1976). Hydrodynamics of wetting. *Fluid Dyn., 11*.

Wang, A., & Chen, C. (2000). Splashing impact of a single drop onto very thin liquid films. *Phys. Fluids, 12*(9), 2155-2158.

Wang, M., Lin, F., Hung, Y., & Lin, S. (2009a). Dynamic Behaviors of Droplet Impact and Spreading: Water on Five Different Substrates. *Langmuir, 25*(12), 6772-6780.

Wang, M., Lin, F., Ong, J. Y., & Lin, S. (2009b). Dynamic behaviors of droplet impact and spreading-Water on glass and paraffin. *Colloids and Surfaces A: Physicochem. Eng. Aspects, 339*, 224-231.

Winnikow, S., & Chao, B. T. (1966). Droplet Motion in Purified Systems. *Phys. Fluids, 9*, 50-61.

Woerhington, A. (1877). On the forms assumed by drops of liquids falling vertically on a horizontal plate. *Proc R Soc London, 25*, 261-271.

Xu, L. (2007). Liquid drop splashing on smooth, rough, and textured surfaces. *Physical Review E, 75*(5), 056316.

Xu, L., Zhang, W., & Nagel, S. R. (2005). Drop splashing on a dry smooth surface. *Physical Review Letters 94*, 184505-184501-184504.

Yarin, A. L. (2006). Drop impact dynamics: Splashing, Spreading, Receding, Bouncing... *Annu. Rev. Fluid Mech., 38*, 159-192.

Yarin, A. L., & Weiss, D. A. (1995). Impact of drops on solid surfaces: self-similar capillary waves, and splashing as a new type of kinematic discontinuity. *J. Fluid Mech., 283*, 141-173.

Zhang, X., & Basaran, O. A. (1997). Dynamic surface tension effects in impact of a drop with a solid surface. *J. Colloid Interface Sci., 187*(1), 166-178.

Zhang, Y., & Ratner, A. (2010). *Fuel drop spreading on a flat smooth surface: numerical simulations with a VOF method.* Paper presented at the ASME 2010 International Mechanical Engineering Congress & Exposition, Vancouver, British Columbia, Canada.

Zhbankova, S. L., & Kolpakov, A. V. (1990). Collision of water drops with a plane water surface. *Fluid Dyn., 25*, 470-473.

Zhou, M. Y., & Sheng, P. (1990). Dynamics of immiscible fluid displacement in a capillary tube. *Phys. Rev. Lett., 64*.